Fracture mechanics of concrete: Structural application and numerical calculation

Edited by

George C. Sih

Lehigh University,
Institute of Fracture and Solid Mechanics,
Bethlehem, PA 18015, USA

A. DiTommaso

University of Bologna
Bologna, Italy

1985 **MARTINUS NIJHOFF PUBLISHERS**
a member of the KLUWER ACADEMIC PUBLISHERS GROUP
DORDRECHT / BOSTON / LANCASTER

Mechanics of fracture and progressive cracking in concrete structures

1.1 Introduction

Cracking is an essential feature of the behavior of concrete structures. Even under service loads, concrete structures are normally full of cracks. Clearly, cracking should be taken into account in predicting ultimate load capacity as well as behavior in service.

To fracture mechanics specialists, it appears natural that concrete structures should be designed according to fracture mechanics. Yet, none of the existing code provisions are based on fracture mechanics. The reason is not ignorance on the part of concrete engineers. Fracture mechanics analysis was tried, and was found to yield predictions that deviate from measurements, on the average, at least as much as those based on the tensile strength approach. These were, however, predictions of the classical, linear fracture mechanics.

In various recent studies, especially those at the Technical University of Lund, Northwestern University and Politecnico di Milano, it became apparent that fracture mechanics does work for concrete, provided that one uses a proper, nonlinear form of fracture mechanics in which a finite nonlinear zone at the fracture front is taken into account. This may be done in various ways. In the first part of the present work, an exposition of one particularly efficient approach will be given. In this approach [8], which is based on the work recently pursued with success by a group of researchers at Northwestern University and Politecnico di Milano, cracking is modeled in a continuous, or smeared manner, and fracture is treated as a propagation of a smeared crack band through concrete. Continuous modeling of cracks in concrete, introduced by Rashid [119], has become popular in finite element analysis, not just because it reflects the reality of densely distributed cracks, but mainly because it is computationally convenient.

In the present engineering practice, tensile strength is used as the cracking criterion. This criterion, however, does not give objective results and does not agree with fracture tests. Remedy can be obtained by

introducing an energy criterion. This approach will be described in detail, along with the finite element implementation, comparisons with fracture tests, and some examples of application. Considered will be the consequence for the structural size effect, and how this effect should be manifested in code formulas for brittle failures, such as the diagonal shear failure of beams. Furthermore, the stability aspects of fracture will be analyzed focusing attention on the strain localization instability as well as crack spacing. Finally, the conclusion will center on a more fundamental study of strain-softening triaxial constitutive relations for the fracture process zone.

The principal intent of this work* is to highlight various new research directions, rather than present a systematic review and description of all the existing knowledge.

1.2 Blunt crack band theory

Basic hypothesis. The analysis which follows is based on the hypothesis that fracture in a heterogeneous material such as concrete can be modeled as a band of parallel, densely distributed microcracks having a blunt front [1–3]. This hypothesis may be justified as follows.

For the purpose of analysis, a heterogeneous material is approximated by an equivalent homogeneous continuum. One must then distinguish the continuum stresses and strains (macrostresses and macrostrains) from the actual stresses and strains in the microstructure, called the microstresses and microstrains. In the theory of randomly inhomogeneous materials, the homogenized continuum stresses and strains are defined as the averages of the microstresses and microstrains over a certain representative volume (Figure 1.1). Its size must be sufficiently large compared to the size of the inhomogeneities. Even for a crude description, this size must be considered to be at least several times the size of inhomogeneities, i.e., several times the maximum aggregate size.

In the usual analysis, only the average elastic (or inelastic) material properties are considered and the geometry of the microstructure with the differences in the elastic constants between the aggregate and the cement paste is not taken into account. The detailed distribution of stress or strain over distances less than several times the aggregate size (Figure 1.1). is then meaningless, and only the stress resultants and the accumulated strain over the cross section of the representative volume have physical meaning. In finite element analysis, it makes, therefore, no sense to use finite elements smaller than several aggregate sizes. In case of fracture, this further means that if an equivalent homogeneous continuum is assumed, it makes no sense to consider concentrations of stress (or of microcrack density) within volumes less than several aggregate sizes (Figure 1.1).

* This work was partially supported under AFOSR grant 83-0009 to Northwestern University.

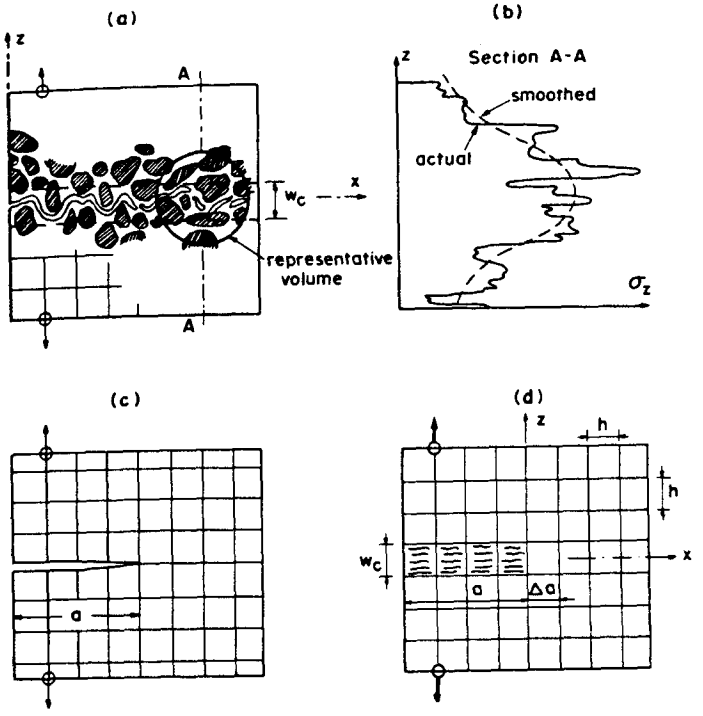

Fig. 1.1. Random microstructure, scatter of microstresses, and crack band or sharp crack model.

Similarly, a straight-line crack is an approximation. The actual crack path in concrete is not smooth but highly tortuous, since the crack tends to pass around the hard aggregate pieces and randomly sways to the side of a straight path by distances roughly equal to the aggregate size (Figure 1.1). Therefore, the actual stress (microstress) variation over such distances cannot be relevant for the macroscopic continuum model.

In view of the foregoing arguments, one should not subdivide the width of the crack band front into several finite elements. There is, however, also another reason. A strain-softening continuum is unstable and exhibits a strain-localization instability [4,5], in which the deformation localizes into one of the elements across the width of the crack band front. This instability will be illustrated later.

For an elastic material in which the stress drops suddenly to zero at the fracture front (Figure 1.2), it is found (regardless of the aggregate size) [6,7] that a sharp interelement crack and a smeared crack band in a square mesh (without any singularity elements) give essentially the same

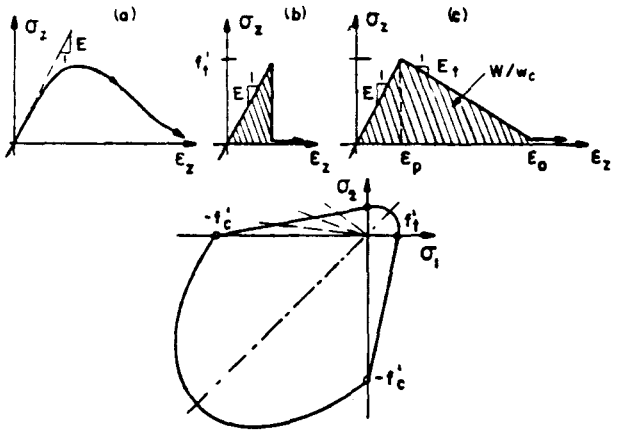

Fig. 1.2. Gradual strain-softening and sudden stress drop (a–c), and biaxial failure envelope (d).

results for the energy release rate and agree closely (within a few percent) with the exact elasticity solution, provided that the finite element is not larger than about 1/15 of the cross section dimension. To demonstrate it here, Figure 1.3 shows some of the numerical results for a line crack (left) and crack band (right) [6]. The finite element mesh covers a cut-out of an infinite elastic medium loaded at infinity by uniform normal stress $\bar{\sigma}$ perpendicular to a line crack of length 2a. The nodal loads applied at the boundary are calculated as the resultants (over the element width) of the exact stresses in the infinite medium at that location. Westergaard's exact solution is shown as the solid curve. The data points show the calculated results for the square mesh shown (mesh A), as well as for meshes B and C (not shown) in which the element size is reduced to 1/2 and 3/8, respectively. Each element consisted of two constant-strain triangles (and calculations were made for $\bar{\sigma} = 0.981\ \alpha$ (MPa), $E_c = 2256$ MPa, $\nu = 0.2$, and stress intensity factor 0.6937 $MNm^{-3/2}$).

A similar equivalence of line crack and blunt crack band may be expected when a gradual stress drop is considered (Figure 1.2). This is confirmed in Figure 1.3c by the fact that a reduction of mesh size does not affect the results. The reason for this equivalence is the fact that fracture propagation depends essentially on the flux of energy into the fracture process zone at the crack front, which represents a global characteristic of the entire structure and depends little on the detailed distributions of stress and strain near the fracture front.

It may be also noted that the results for the stress intensity factor [6] obtained with nonsingular finite elements agree with the exact elasticity solution quite closely, usually within 1% for typical meshes. There is no need to use singularity elements in fracture analysis. Moreover, one

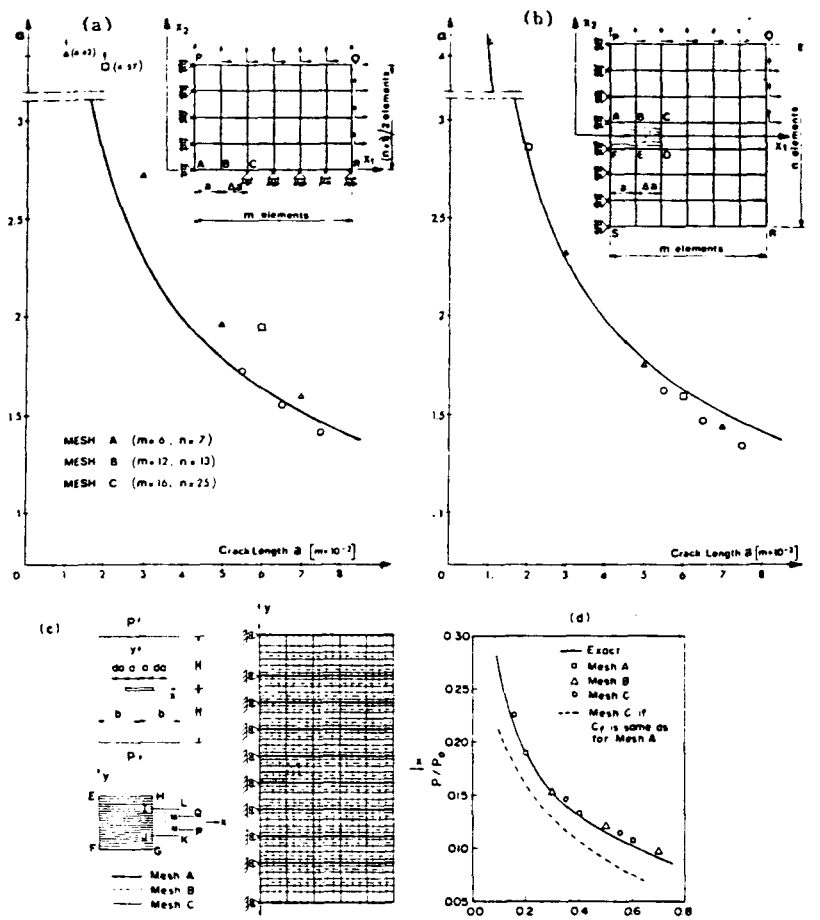

Fig. 1.3. Finite element results of Bažant and Cedolin (1979) for sudden stress drop (a, b), showing equivalence of blunt crack band and sharp crack modeling, and results of Bažant and Oh (c, d), showing the results for gradual stress decrease and meshes of different size.

should realize that the nonuniform stress distribution implied in a singularity element is meaningful only if this element is many times larger than the representative volume, i.e., is at least 20 aggregate pieces in size, which is too large for most applications.

Because the line crack and the crack band models are essentially equivalent, the choice of one or the other is principally a question of computational convenience. The line crack model appears to be less convenient. When a line crack extends through a certain node, the node must be split into two nodes. This increases the total number of nodes and changes the topological connectivity of the mesh. Unless one renumbers the nodes, the band structure of the structural stiffness matrix is

destroyed. All this complicates programming. Furthermore, when the direction in which a Mode I crack should extend is not known in advance, one must make trial calculations for various possible locations of the node ahead of the crack front through which the crack should pass, in order to determine the location which gives the maximum energy release rate.

The smeared cracking approach, introduced by Rashid [8] avoids these difficulties. The cracking is modeled simply by changing the isotropic elastic moduli matrix to an orthotropic one, reducing the material stiffness in the direction normal to the cracks in the band. This is easily implemented by finite elements. Moreover, a crack propagation in an arbitrary direction with respect to the mesh lines, or a crack following a curved path, may be easily modeled as a zig-zag crack band (Section 1.3) whose overall path through the mesh approximates the actual crack path. Another advantage of the crack band model is that the known properties of stress-strain relations and failure envelopes can be applied to fracture; this includes, e.g., the effect of the compressive normal stress parallel to the crack, or the effect of creep. Still another advantage of the crack band model is the fact that, as it will be shown in the sequel, one can treat the case when principal stress directions in the fracture process zone rotate during the progressive fracture formation, i.e., during the strain softening,

Ahead of the tip of a propagating major crack in concrete, there is always a relatively large zone of discontinuous microcracks. Formation of microcracks at the fracture front has recently been observed experimentally [9–11]. From measurements of tensile strain fields by Moiré interferometry [10,11], it appears that there is at the fracture front a zone of microcracks whose width is about the aggregate size. From microscopic observations, it seems that the larger, easily discernible microcracks are not spread over a band of a large width but are concentrated essentially on a line. However, the line along which the microcracks are scattered is not straight but is highly tortuous (Figure 1.1), deviating to each side of the overall fracture axis by a distance equal roughly to the aggregate size, as the crack is trying to pass around the harder aggregate pieces. In the equivalent, smoothed macroscopic continuum which is implied in structural analysis, the scatter in the locations of visible microcracks is characterized by a microcrack band better than by a straight row of microcracks. Further, it should be realized that the boundary of the fracture process zone should not be defined as the boundary of visible microcracks but as the boundary of the strain-softening region, i.e., the region in which the maximum stress decreases with increasing maximum strain. Since the strain-softening is caused not just by microcracking but also by unobservable bond ruptures and submicroscopic flaws, the fracture process zone is probably much wider (as well as longer) than the region of

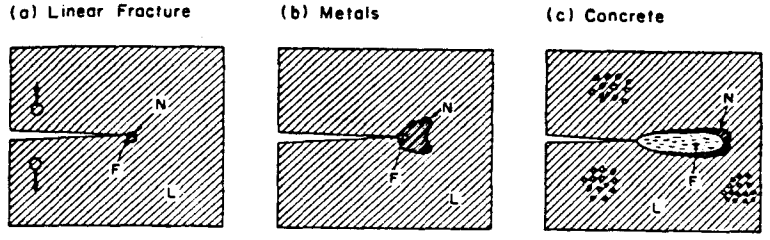

Fig. 1.4. Shape of nonlinear zone (N) and fracture process zone (F).

visible microcracks. Measurements of Cedolin et al. [10,11] appear to support this view. However, because of the foregoing justifications, the question of the actual shape of the microcrack zone is unimportant for the macroscopic continuum modeling.

In ductile fracture of metals, there is a large plastic zone in which the metal is yielding but does not undergo strain-softening, and the strain-softening zone itself (i.e., the fracture process zone) is only a small part of the yielding zone (Figure 1.4). On the other hand, in concrete, the nonlinear zone is not much larger than the strain-softening zone (Figure 1.4) since concrete in tension is not capable of plastic deformation. Thus one may consider that the concrete outside the fracture process zone behaves as nearly elastic.

If the relation of the normal stress σ_z and the relative displacement δ_f across a line crack is identical to the relation of σ_z to the displacement δ_f obtained by accumulating the strains ε_f due to microcracking over the width w_c of the crack band [1], then, according to the above reasoning, the line crack model and the crack band model are essentially equivalent. Line crack models with softening stress-displacement relations were proposed in many previous works [12–18]. These include especially the works of Knauss [16], Wnuk [17], and Kfouri, Miller and Rice [14,15] on polymers and metals, which considered a gradual release of the forces between the opposite surfaces as the opening displacements grow, and modeled it by a gradual decrease of the internodal force as one node in a finite element grid is being separated by fracture into two nodes. For concrete, the concept of a gradually decreasing stress-displacement relation was first applied in the outstanding original work of Hillerborg, Modéer and Petersson [18,19] in their model of fictitious sharp interelement crack. Their pioneering work provided inspiration for developing the present blunt crack model with gradual strain-softening.

Stress-strain relation for fracture process zone. Cartesian coordinates $x_1 = x$, $x_2 = y$, and $x_3 = z$ will be introduced with the cracks being assumed to be normal to the axis z. The normal stress and strain

components may be grouped into the column matrices $\sigma = (\sigma_x, \sigma_y, \sigma_z)^T$, $\varepsilon = (\varepsilon_x, \varepsilon_y, \varepsilon_z)^T$, where T denotes the transpose. The strains are assumed to be linearized or small. The elastic stress-strain relation for the normal components may then be written as $\sigma = D\varepsilon$, in which D is the stiffness matrix of the uncracked material,

$$D = \begin{bmatrix} D_{11} & D_{12} & D_{13} \\ & D_{22} & D_{23} \\ \text{sym.} & & D_{33} \end{bmatrix}. \tag{1.1}$$

If the elastic material is intersected by continuously distributed parallel cracks normal to z, the stress-strain relation has the form [8,20] $\sigma = D^{fr}\,\varepsilon$, in which

$$D^{fr} = \begin{bmatrix} D_{11} - D_{13}^2 D_{33}^{-1}, & D_{12} - D_{13}D_{23}D_{11}^{-1}, & 0 \\ & D_{22} - D_{23}D_{33}^{-1}, & 0 \\ \text{sym.} & & 0 \end{bmatrix} \tag{1.2}$$

This matrix, representing the stiffness matrix of a fully cracked material, may be derived from the condition that strain ε_z^m of the material between the crack is unrelated to ε_z (except for $\varepsilon_z^m < \varepsilon_z$) and that the stress normal to the cracks must be zero, assuming that the material between the cracks behaves as an uncracked elastic material in a plane stress state. This, of course, is a simplification, because the material between the cracks becomes damaged by discontinuous microcracks.

To describe progressive development of microcracks in the fracture process zone, it is necessary to formulate a stiffness matrix which continuously changes from the form given in Eq. 1.1 to that in Eq. 1.2. This objective is hard to achieve by direct reasoning, since every element of the 6×6 stiffness matrix changes. It was found [1,3], however, that the task becomes easier if the compliance matrix, C, is used. For a crack-free material,

$$\varepsilon = C\sigma, \tag{1.3}$$

where

$$C = D^{-1} = \begin{bmatrix} C_{11} & C_{12} & C_{13} \\ & C_{22} & C_{23} \\ \text{sym.} & & C_{33} \end{bmatrix} \tag{1.4}$$

Now, if only cracks normal to x are permitted, the appearance of

cracks at constant stresses increases only the overall strain ε_z normal to the cracks and has no effect on the lateral strains ε_x and ε_y. Therefore, the compliance matrix after appearance of partial discontinuous cracks should have the form [1,3]:

$$C(\mu) = \begin{bmatrix} C_{11} & C_{12} & C_{13} \\ & C_{22} & C_{23} \\ \text{sym.} & & C_{33}\mu^{-1} \end{bmatrix} \tag{1.5}$$

where μ is a certain parameter, called cracking parameter, which increases C_{33}. This formulation must, in the limit, be equivalent to the well-known generally accepted stiffness matrix D^{fr} for a fully cracked material (Eq. 1.2). Indeed, as generally proved in [1], the matrix in Eq. 1.2 results as

$$D^{fr} = \lim_{\mu \to 0} C^{-1}(\mu). \tag{1.6}$$

In writing a computer program, it is convenient for the programmer to note that instead of setting $\mu = 0$, one may assign in the program μ^{-1} as a very large number (e.g., 10^{40}) and let the computer carry out the inversion of the matrix numerically; the result is a stiffness matrix like that in Eq. 1.2 except that extremely small numbers (10^{-40}) are obtained instead of 0.

A characteristic feature of the compliance matrix for progressive microcracking (Eq. 1.4) is the fact that cracking has no effect on lateral strains. This can be true only if all microcracks are normal to axis z, which is certainly a simplification. In reality, a certain distribution of the orientations of the microcracks is expected, the orientation normal to axis x being just the prevalent one, not the only one. If inclined microcracks were considered, than it would be necessary to also introduce a gradual change of the off-diagonal terms in Eq. 1.4 as the formation of microcracks advances.

Comparing now the compliance matrices in Eqs. 1.5 and 1.6, it is seen that a continuous transition from a crack-free state to a fully cracked state may be very simply obtained by continuously varying the cracking parameter μ between the limits

$$\text{uncracked state;} \quad \mu = 1 \quad \text{and} \quad \text{fully cracked state:} \quad \mu = 0 \tag{1.7}$$

The law governing the variation of the cracking parameter, μ, may be determined on the basis of the uniaxial tensile test. It has been proven independently by several investigators [21–25] that concrete exhibits tensile strain-softening, i.e., a gradual decrease of stress at increasing

strain. Tests of strain-softening are stable only if the loading frame is much stiffer than the specimen and if the specimen is not too long. The observed stress-strain relation appears [21,22,24,26] to be smoothly curved. Although a curved strain-softening can be easily implemented with parameter μ, we assume, for the sake of simplicity, a bilinear stress-strain relation (Fig. 1.2), the declining (strain-softening) branch of which is characterized by negative compliance C_{33}^t.For uniaxial tension σ_z it follows that

$$\varepsilon_z = C_{33}\mu^{-1}\sigma_z \quad \text{or} \quad \sigma_z = C_{33}\mu^{-1}\varepsilon_z \tag{1.8}$$

which must be equivalent to the relation $\sigma_z = (\varepsilon_z - \varepsilon_0)C_{33}^t$ for the straight-line softening in which C_{33}^t is negative and ε_0 represents the terminal point of the strain-softening branch at which the tensile stress vanishes (Fig. 1.2). This point is related to the strain ε_p at the peak stress point, $\varepsilon_0 = \varepsilon_p + (-C_{33}^t)f_c'$. Comparing the foregoing two expressions for σ_z, the following result is obtained [1]:

$$\mu^{-1} = \frac{-C_{33}^t}{C_{33}} \frac{\varepsilon_z}{\varepsilon_0 - \varepsilon_z} \tag{1.9}$$

as the law governing the variation of cracking parameter μ. Substituting Eq. 1.9 and Eq. 1.5 and inverting the matrix, the stiffness matrix $\boldsymbol{D}$ to be used in the finite element program is then obtained.

Concrete may be considered to be isotropic. It follows that

$$C_{33} = 1/E, \quad C_{33}^t = 1/E_t \tag{1.10}$$

where E = Young's modulus, and the compliance matrix for partially cracked concrete takes the following special form:

$$\boldsymbol{C}(\mu) = \frac{1}{E}\begin{bmatrix} 1 & -\nu & -\nu \\ -\nu & 1 & -\nu \\ -\nu & -\nu & \mu^{-1} \end{bmatrix} \tag{1.11}$$

and the limit of its inverse at $\mu \to 0$ is

$$\boldsymbol{D}^{fr} = \frac{E}{1-\nu^2}\begin{bmatrix} 1 & \nu & 0 \\ \nu & 1 & 0 \\ 0 & 0 & 0 \end{bmatrix} \tag{1.12}$$

in which E = Young's modulus and ν = Poisson's ratio.

In computer finite element analysis, it is most convenient to use the incremental loading technique. For this purpose, the incremental stress-strain relations may be obtained differentiating Eq. 1.3 in which μ from

Eq. 1.9 is substituted. In a finite element program, it is also necessary to enlarge the compliance and stiffness matrices to a 6×6 form, including the rows and columns for shear strains and stresses. Most simply, these may be considered to be the same as for a crack-free material, except that the shear stiffness in the diagonal term needs to be reduced by an empirical shear stiffness reduction factor [27,20]. More accurately, the columns and rows for the shear behavior should reflect the frictional-dilatant properties of cracks; see, e.g., [28,29]. The question of shear terms is, however, often unimportant since fracture is geomaterials usually occurs in principal stress directions.

During the passage of the fracture process zone through a fixed station, the principal stress directions usually do not rotate significantly. This justifies another simplifying assumption which has been implied in the preceding formulation. It is the fact that we use total stress-strain relations (Eqs. 1.3 and 1.5) which are path-independent. In reality, all inelastic behavior is path-dependent. Nevertheless, the assumption of path-independence of the stress-strain relation in the vicinity of the fracture front may be adequate for many situations. Note that the microplane model outlined in the sequel provides the possibility to take into account the path-dependence if one is willing to accept a more complicated method of analysis (Eq. 1.93 in the sequel).

The difference of the total strain ε_z at the strain-softening branch from the strain predicted for an uncracked material, i.e., $\varepsilon_f = \varepsilon_z - \sigma_z/E$, represents the strain which is caused by microcracking. If this strain is integrated over the width of the crack band, i.e., $\delta_f = \varepsilon_f w_c$, one may obtain from our stress-strain relation a stress-displacement relation. For models in which the fracture is treated as a sharp interelement crack, this displacement is analogous to the opening displacement, δ_f, of such a crack. In this sense, the present theory is equivalent to previous models based on stress-displacement relations, especially the model of Hillerborg et al. [18,19].

The blunt crack band approach lends itself logically to describing the effect on fracture of the triaxial stress state in the vicinity of the crack front. From extensive testing, it is known that in the presence of transverse normal compression stresses, the tensile strength is diminished [27,30,31,1,32]. The measured biaxial failure envelope (Figure 1.2d) seems to consist approximately of a straight line which connects the failure point for uniaxial tensile failure to that for uniaxial compression failure in the (σ_x, σ_y) plane. Accordingly, we may suppose that transverse compressive stresses reduce the peak stress f_t' to the value f_{tc}' given as:

$$\text{for } \Delta f_t' \leqslant 0: \quad f_{tc}' = f_t' + k(\sigma_x + \sigma_y)$$

$$\text{for } \Delta f_t' > 0: \quad f_{tc}' = f_t' \tag{1.13}$$

where f_t' = uniaxial tensile strength, f_c' = uniaxial compression strength, and $k = f_t'/f_c'$.

It is worth noting that if μ is replaced by $1 - \omega$, then ω resembles the damage parameter used in the so-called continuous damage mechanics, which has recently been applied to concrete [33–37]. There is, however, a fundamental difference in that the damage due to microcracking is considered to be inseparable from a zone of a certain characteristic width, w_c, which is a fixed parameter, a material property.

Fracture characteristics. The fracture energy is defined as the energy consumed by crack formation per unit area of the crack plane. It may be calculated as

$$G_f = W_f w_c, \quad W_f = \int_0^{\varepsilon_0} \sigma_z \, d\varepsilon_z \tag{1.14}$$

in which w_c is the width of the crack band (fracture process zone) and W_f the work of tensile stress per unit volume which is equal to the area under the tensile stress-strain curve (Figure 1.2).

In theory, it should be possible to determine the crack band width w_c by analyzing the strain-localization instability that leads to fracture. It should be possible to do this by extending the previous simple analysis of this instability [4,5]. The practical calculation would be, however, quite complicated in case of a large fracture process zone with a nonhomogeneously stressed specimen. Aside from that, if both W_f and G_f are considered as constants, w_c should also be a constant. This constant may be determined empirically. For the bilinear tensile stress-strain relation (Figure 1.2), one has

$$W_f = \tfrac{1}{2}(C_{33} - C_{33}^t) f_t'^2 w_c = \tfrac{1}{2} f_t' \varepsilon_0, \quad \text{or} \quad w_c = \frac{2G_f}{f_t'^2} \frac{1}{C_{33} - C_{33}^t} \tag{1.15}$$

in which C_{33}^t is negative. For isotropic material, $C_{33} = 1/E$, $C_{33}^t = 1/E_t$. This equation indicates that the width of the fracture process zone, precisely, the effective width corresponding to a uniform transverse distribution of tensile strain over the crack band, may be determined by measuring the softening compliance, the tensile strength, and the fracture energy. To ensure that C_{33}^t be negative, Eq. 1.15 requires that

$$w_c < w_0, \qquad \text{where } w_0 = \frac{2C_f}{f_t'^2 C_{33}} \quad \text{or} \quad w_0 = \frac{2G_f E}{f_t'^2}. \tag{1.16}$$

Note that the expression for w_0 is similar to the well-known Irwin's

expression for the size of the yielding zone [39–41], in which the yield stress appears instead of f_t'.

Because of the aforementioned approximate equivalence of the fracture models utilizing stress-displacement relations for sharp cracks [18], it seems that the precise width w_c of the fracture process zone should not matter, provided that correct energy dissipation due to crack formation is assured. In other words, we should get essentially the same results utilizing different widths of the crack band, provided we adjust the softening compliance C_{33}^t so as to assure that the energy consumed in the fracture process zone equals the given value G_f. Thus, we may choose the value w_c, and then we may calculate C_{33}^t from Eq. 1.15, thereby assuring the energy consumption to be correct. It has been numerically demonstrated [1] (Figure 1.3) that indeed the analyses with different w_c yield essentially the same numerical results. If insistance is made on using the correct experimentally observed softening compliance C_{33}^t, then, of course, only one value of the crack band width w_c is correct. It has been from this condition that the value of w_c has been determined (Eq. 1.17 below).

Although the stress intensity factor, K_I, cannot be defined here as a limiting property of the stress field, one may introduce an "effective" K_I employing the relation known from linear fracture mechanics: $K_I = \sqrt{G_f E'}$ where $E' = E$ for plane stress, and $E' = E/(1 - \nu^2)$ for plane strain. All the subsequent expressions involving G_f could be stated in terms of K_I, but there is no need for this.

Comparison with fracture test data. Most of the important test data from the literature [25,43–57] have been successfully fitted in report [1] with the present nonlinear fracture model. Some of the fits, obtained in [1] by finite element analysis using square meshes, are shown in Figures 1.5 and 1.6 by the solid lines. The best possible fits obtainable with linear fracture mechanics are shown for comparison in these figures as the dashed lines (these fits were calculated also by the finite element method using square meshes). In computations, the loading point was displaced in small steps. Reaction, representing the load P, was evaluated at each loading step. The same stress-strain relation was assumed to hold for all finite elements. However, only some elements entered nonlinear behavior. A plane stress state was assumed for all calculations.

In optimizing the data fits, it was discovered that the optimum width on the crack band front was for all cases between $2d_a$ and $5d_a$ and that the crack band front width

$$w_c = 3d_a, \tag{1.17}$$

where d_a = maximum aggregate size, was nearly optimum for all calculations. It was for this width w_c that the area under the stress-strain curve

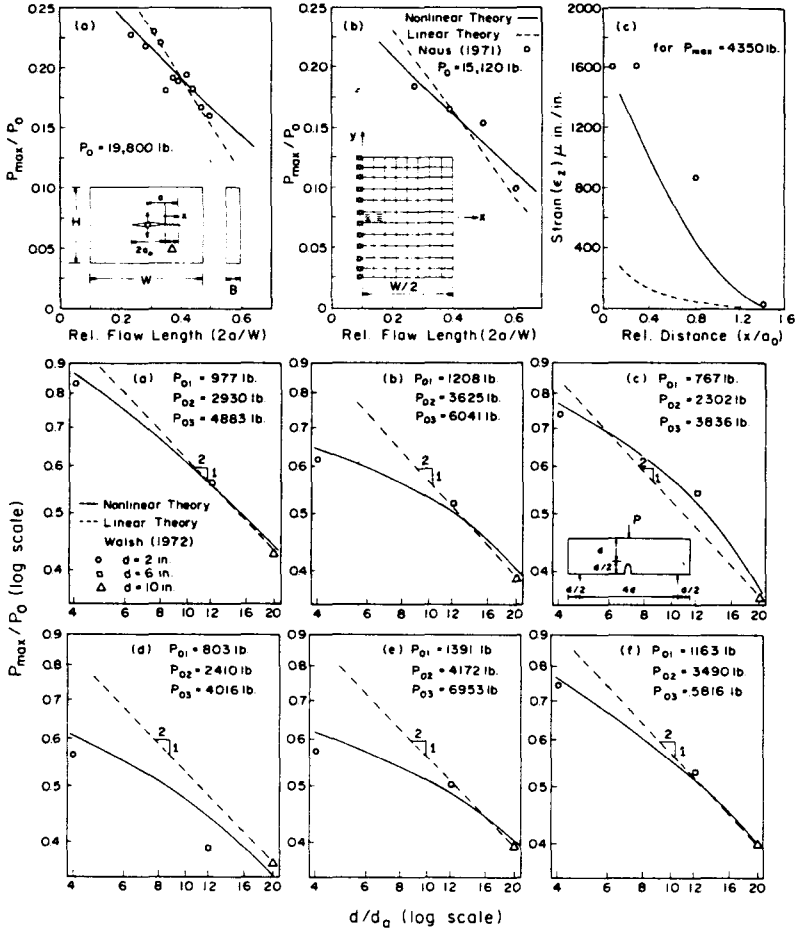

Fig. 1.5. Comparison of theory with maximum load test data of Naus (1971) and Walsh (1972) (P_0 = max. load according to strength concept).

yielded the correct value of the fracture energy needed to obtain good fits of the test data. It thus appears that, at least for plain concretes, the width of the crack band front may be predicted from the maximum aggregate size. However, we must caution that the foregoing simple relation might not hold for high strength concretes, in which the crack band is, no doubt, more concentrated, since the difference between the strengths of aggregate and matrix is less.

In view of Eq. 1.17, the present fracture theory is essentially a two parameter theory. The two material parameters to be determined by experiment are G_f and f'_c.

As for the length of the fracture zone (the strain-softening zone), its value is not constant. A typical value is roughly 12 d_a, but it can be as

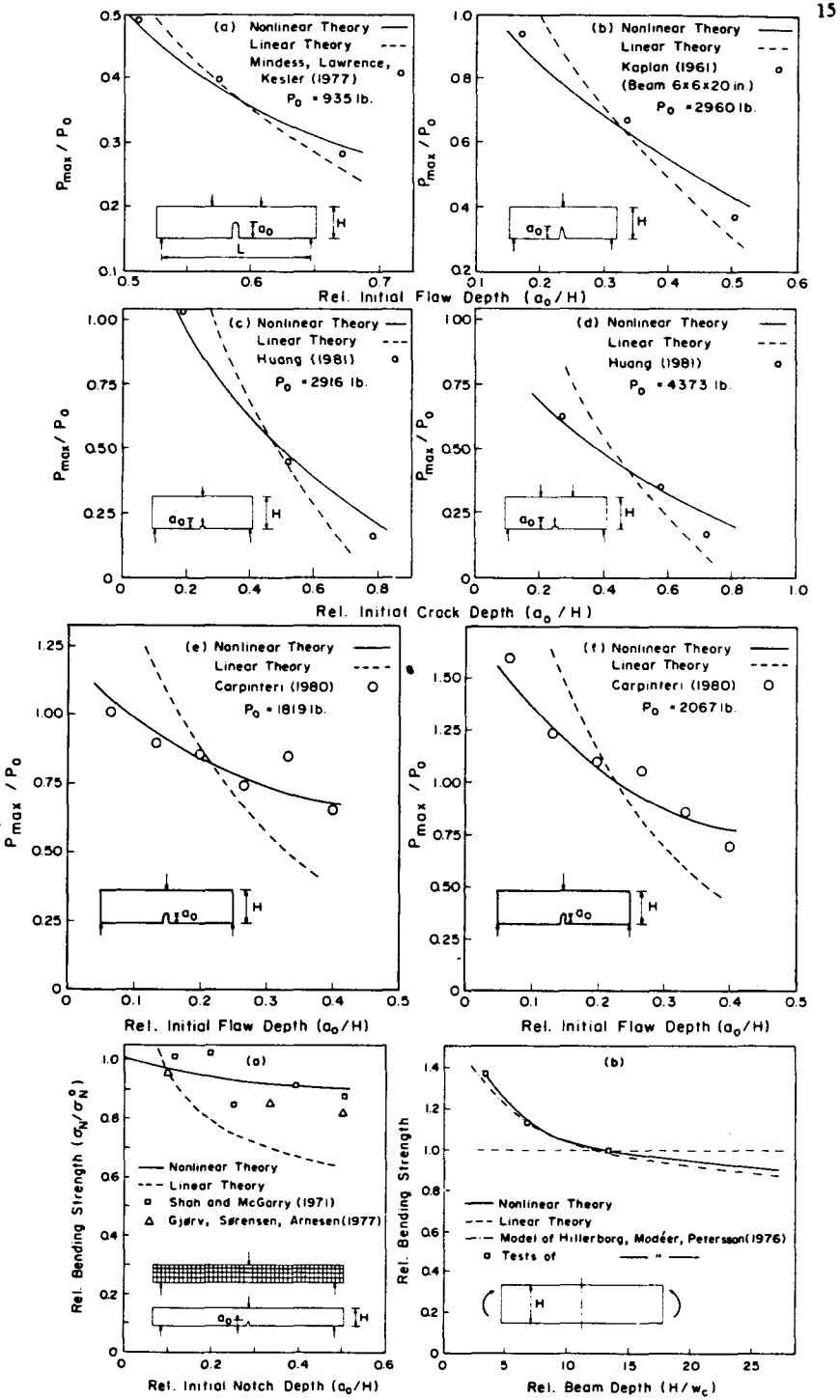

Fig. 1.6. Comparison of theory with maximum load test data by Kaplan (1961), Mindess et al. (1977), Huang (1981), Carpinteri (1980), Shah and McGarry (1971), Gjørv et al. (1971), and Hillerborg et al. (1976).

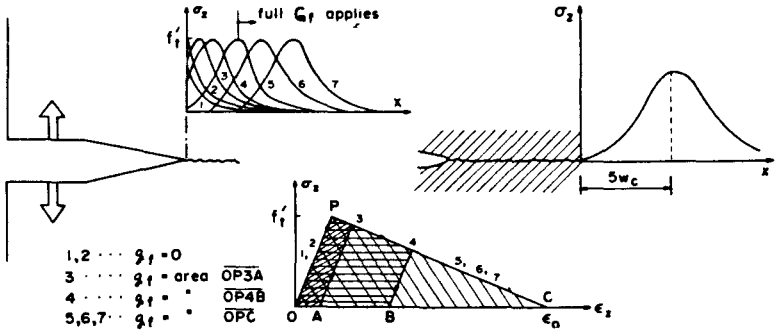

Fig. 1.7. Finite element results of Bažant and Oh (1983) on stress distribution (1,2,... 7) ahead of fracture front at successive loading stages, and corresponding states on stress-strain curves.

small as d_a. This is illustrated by the calculated stress profiles at various stages of loading, shown in Figure 1.7 along with the associated states on the stress-strain diagram.

Figures 1.5 and 1.6 represent maximum load data, for which the P_{max}-values are normalized with regard to the engineering strength theory predictions. The data are plotted as a function of either crack length or structure size. Note that the theory also yields the size effect in bending failure of unnotched beams (data of Hillerborg et al. in Figure 1.6). This confirms that this effect is principally a fracture size effect, and not an effect of statistical inhomogeneity of cross section. It is due to the fact that, in a small beam, the fracture process zone cannot develop to full length, causing the energy consumed by fracture to be less than in a deep beam.

Nonlinear fracture properties are sometimes characterized by means of R-curves (resistance curves), which represent the variations of apparent fracture energy as a function of the crack extension from a notch. In some recent works, the R-curves were considered as a basic material property [41]. This is not so, however, according to the present theory, since the R-curves can be unique only in the asymptotic sense, for infinitely small crack extension from a notch. In the present calculations, the resulting R-curves are somewhat different for different specimen geometries, loading arrangements, etc. At the beginning of crack extension from a notch, the theory gives a smaller value of fracture energy because the fracture process zone is not yet fully developed.

The apparent fracture energies needed to generate the curves in Figure 1.8 were obtained by evaluating for each crack length increment the total loss of strain energy from all finite elements outside the crack band, which behave elastically. The specimens for Sok et al.'s data in Figure 1.8 were prestressed in the direction parallel to crack, and this had to be taken into account; Eq. 1.13 was used.

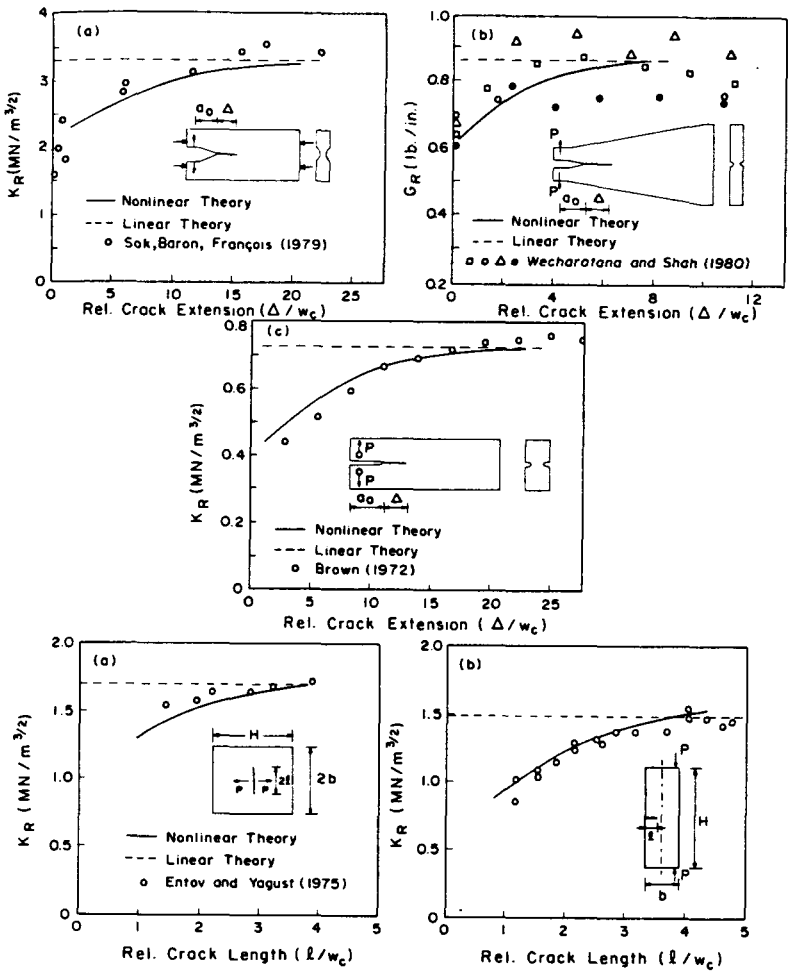

Fig. 1.8. Comparison of theoretical R-curves with test data by Sok et al. (1979), Wecharatana and Shah (1980), Brown (1972), and Entov and Yagust (1975) (K_R is the stress intensity factor corresponding to fracture energy $G_R = G_F$).

For details of data fitting and interpretation of test data, see [1]. Table 1.1 [1] summarizes the values of material parameters for all the data fits shown. Note that the values of G_f obtained with the present formulation are considerably different from the G_f values obtained by the experimentalists in a different manner. Table 1.1 also lists the values G_f^{lin} which give the best fits for linear fracture mechanics (dashed lines).

The present theory has also been used to analyze the most important test data on the fracture of rock available in the literature [58]. For rocks of very different types, involving Indiana limestone, Carrara marble,

TABLE 1
Parameters for fracture test data (after Bažant and Oh, 1983)

Test series	f_t' (psi)	E (ksi)	G_f (lb./in.)	d_a (in.)	w_c (in.)	G_f^{lin} (lb./in.)	c_f	$\bar{G}_f$ (lb./in.)
1. Naus – no. 1	460 *	4,450 *	0.205 *	0.375	1.125 *	0.430 *	7.664 *	0.224 *
2. Naus – no. 2	360 *	4,500 *	0.099 *	0.375	1.125 *	0.249 *	6.111 *	0.113 *
3. Walsh – no. 1	347 *	3,299 *	0.174 *	0.50	1.50 *	0.188 *	6.356 *	0.185 *
4. Walsh – no. 2	430 *	4,083 *	0.188 *	0.50	1.50 *	0.173 *	5.535 *	0.270 *
5. Walsh – no. 3	273 *	2,593 *	0.126 *	0.50	1.50 *	0.158 *	5.845 *	0.123 *
6. Walsh – no. 4	286 *	2,716 *	0.133 *	0.50	1.50 *	0.162 *	5.888 *	0.133 *
7. Walsh – no. 5	495 *	4,697 *	0.224 *	0.50	1.50 *	0.173 *	5.725 *	0.348 *
8. Walsh – no. 6	414 *	3,928 *	0.193 *	0.50	1.50 *	0.176 *	5.897 *	0.253 *
9. Mindess, Lawrence, Kesler	370 *	6,260	0.088 *	0.375	1.125 *	0.170 *	7.154 *	0.087 *
10. Shah, McGarry	300 *	3,000 *	0.108 *	0.375	1.125 *	0.047 *	6.400 *	0.103 *
11. Gjørv, Sørensen, Arnesen	300 °	3,000 *	0.108 *	0.375	1.125 *	0.047 *	6.400 *	0.103 *
12. Kaplan	300 *	4,190	0.101	0.50	1.50 *	0.177 *	6.269 *	0.098 *
13. Huang – no. 1	360 *	3,122 *	0.225 *	0.50	1.50 *	0.337 *	7.227 *	0.217 *
14. Huang – no. 2	360 *	3,122 *	0.225 *	0.50	1.50 *	0.245 *	7.227 *	0.217 *
15. Carpinteri – no. 1	313 *	2,700 *	0.207 *	0.375	1.125 *	0.147 *	10.14 *	0.128 *
16. Carpinteri – no. 2	356 *	3,130 *	0.280 *	0.752	2.256 *	0.201 *	6.130 *	0.315 *
17. Hillerborg, Modéer, Petersson	400 *	3,300 *	0.100 *	0.157	0.471 *	0.118 *	8.758 *	0.086 *
18. Sok, Baron, François	740 *	3,000 *	2.800 *	0.472	1.416 *	2.910 *	21.66 *	1.600 *
19. Brown	690 *	2,200 *	0.182 *	0.047	0.141 *	0.185 *	11.93 *	0.178 *
20. Wecharatana, Shah	740 *	3,000 *	0.855 *	0.250 *	0.750 *	0.860 *	12.49 *	0.848 *
21. Entov, Yagust – no. 1	450 *	3,000 *	0.746 *	0.787	2.360 *	0.755 *	9.366 *	0.657 *
22. Entov, Yagust – no. 2	440 *	3,000 *	0.640 *	0.787	2.360 *	0.630 *	8.405 *	0.617 *

Note: psi = 6895 N/m^2, lb./in. = 175.1 N/m, in. = 25.4 mm, ksi = 1000 psi; $c_f \doteq 1 - E/E_t$.
* Asterisk indicates numbers estimated by calculations; without asterisk as reported.

Colorado oil shale, and Westerly granite, it was found that nearly optimum fits are achieved for all these rocks with $w_c = 5d_g$ where d_g = grain size of rock. These studies involved the measurements of maximum load, as well as of the resistance curves (R-curves). Statistical regression analysis for the test data for various rocks also indicated a significant improvement. The coefficient of variation of the deviation from the regression line for the plot of relative maximum load values was found to be 10.6%. This is to be compared with the value 15.2% for linear fracture theory, and the value 79.6% for strength-based predictions.

The test data on concrete fracture available in the literature are sufficiently numerous for a statistical regression analysis of the errors. Figure 1.9 shows a regression analysis of the maximum load data for twenty-two different concretes [1]. In this plot, the abscissa is $X = P_t/P_0$ and the ordinate is $Y = P_m/P_0$, in which P_m = measured maximum load P_{max}, P_t = theoretical value of P_{max}, and P_0 = failure loads calculated according to the strength theory. If the theory were perfect, then the plot of Y vs. X would have to be a straight line of slope 1.0, passing through the origin. Thus, the vertical deviations of the data points from the regression line characterize the errors of the theory. The coefficient of variation, ω, of the vertical deviation from the regression line in Figure 1.9 is [1]:

For the present fracture theory	$\omega = 0.066$	
For linear fracture theory	$\omega = 0.267$	(1.18)
For strength criterion	$\omega = 0.650$	

These results confirm that the improvement achieved with the present non-linear fracture theory is quite significant.

The test data available in the literature on the R-curves may be analyzed similarly [1]. In this regression analysis, the fracture energy values were normalized with regard to the product $f_t' d_a$, and the theoretical values of $G_f/f_t' d_a$ were plotted against the measured values of this ratio. Again, if everything worked perfectly, this plot would have to be a straight line of slope 1.0 and intercept 0.0. The standard errors for the vertical deviations from this regression line have been calculated for the sets of various test data available in the literature,

For the present fracture theory:	$s = 0.083$	
For linear fracture theory:	$s = 0.317$	(1.19)

The values of the fracture energy obtained for the optimum fits of various fracture data on concrete were further examined to see whether the fracture energy could be approximately predicted from the elemen-

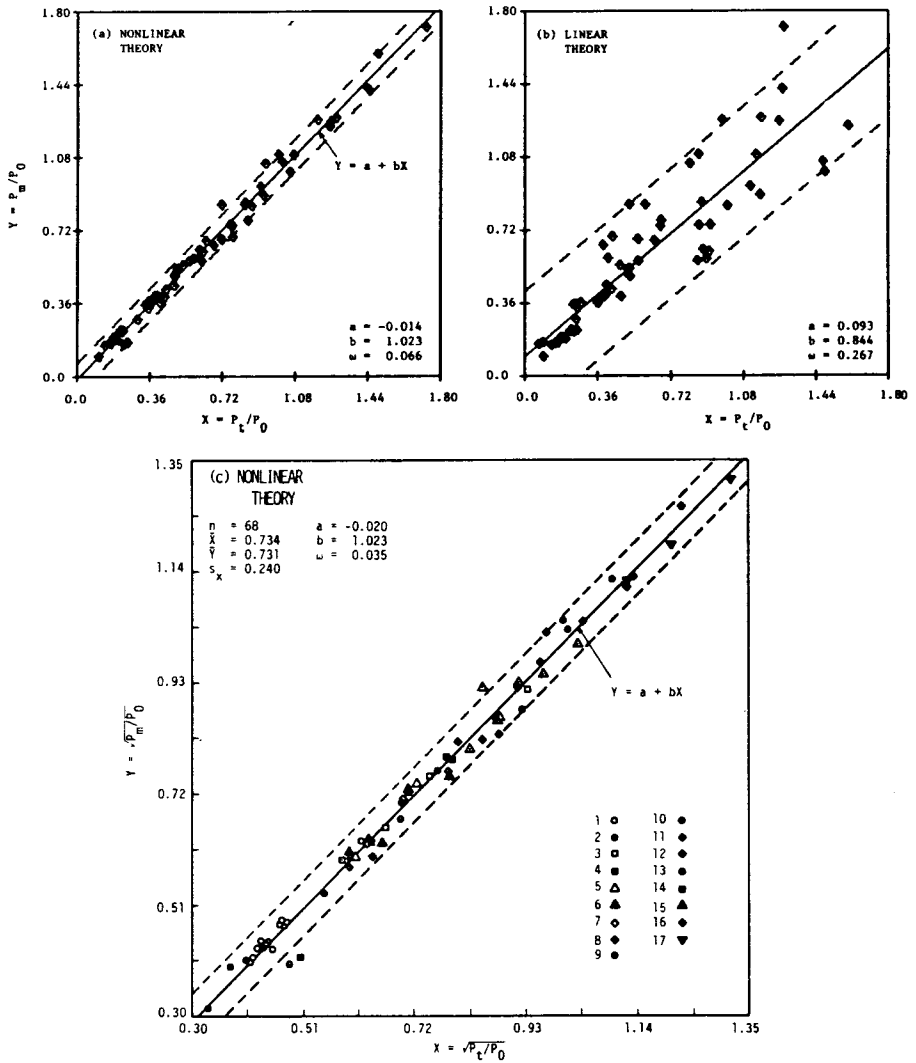

Fig. 1.9. (a) Statistical regression analysis of maximum load data from Figs. 5–6 based on present theory (P_m = measured maximum load, P_t = theoretical maximum load); (b) same, but for linear fracture mechanics; (c) same as (a) but in a different scale (data set numbers – see Table 1).

tary characteristics of concrete. The following approximate formula was found [1]

$$\tilde{G}_f \simeq 0.0214(f_t' + 127)f_t'^2 d_a/E \tag{1.20}$$

in which f_t' must be in psi (psi = 6895 Pa), d_a = maximum aggregate size,

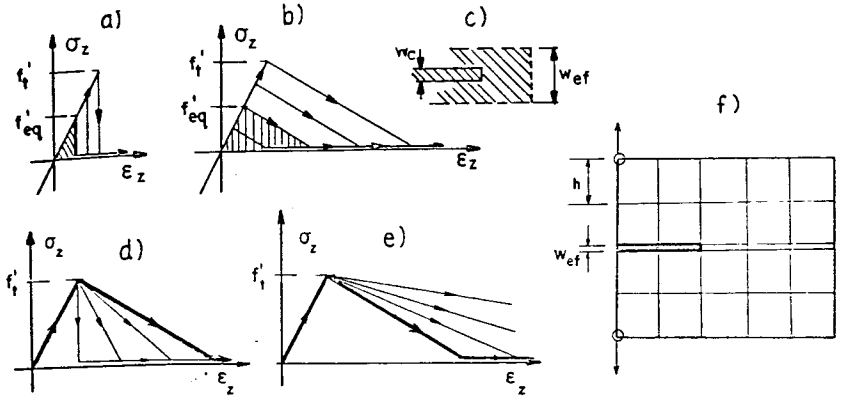

Fig. 1.10. Change of stress-strain relation for fracture process zone needed to ensure correct energy dissipation.

E = elastic modulus, and $\tilde{G}_f$ is in lb/in. The values $\tilde{G}_f$ predicted from Eq. 1.20 are listed in Table 1.1. The coefficient of variation of the errors $G_f - \tilde{G}_f$ is about 16% [1].

It must be emphasized, however, that Eq. 1.20 yields only the fracture energy values for the present nonlinear theory, and not the apparent fracture energy values determined according to linear fracture mechanics or those determined from other theories.

Noting that $G_f \simeq 3d_a f_t'^2(E^{-1} - E_t^{-1})/2$, the following prediction formula for E_t further ensues:

$$E_t \simeq \frac{-69.9\,E}{f_t' + 56.7} \tag{1.21}$$

1.3 Finite element implementation

Effect of element size. Eq. 1.16 gives the upper bound on the finite element size for the present formulation. However, for large structures such as dams or reactor vessels, much larger finite elements need to be used and should be sufficient. This is indeed possible if the correct value of fracture energy G_f is preserved. To preserve it, the strength limit f_t' needs to be reduced to a lower value f_{eq}', called the equivalent strength [6,59,60]. We may either consider a vertical stress drop (Figure 1.10a) or keep the correct declining slope E_t (Figure 1.10b).

Consider a vertical stress drop and assume a uniform stress distribution across the crack band. The condition of preserving the correct fracture energy for crack band advance Δa is $\Delta U = \Delta U_2 - \Delta U_1 = G_1 \Delta a$

where $\Delta U_1 = (c_f^2 w_{ef} \Delta a/2E')[\sigma_1(\sigma_1 - \nu'\sigma_3) + \sigma_3(\sigma_3 - \nu'\sigma_1)]$ = strain energy in the frontal element before its cracking, $\Delta U_2 = (k_w w_{ef} \Delta a/2E')\sigma_1'^2$ = strain energy in this element after cracking; σ_3, σ_2 = initial transverse and longitudinal normal stresses in the element, σ_1' = longitudinal normal stress after cracking; $w_{ef} = h$ = element side if the crack band runs in a square mesh parallel to a mesh line; c_f = empirical coefficient (close to 1) taking into account the actual nonuniform stress distribution in the finite element; and for plane stress $E' = E$, $\nu' = \nu$, while for plane strain $E' = E/(1 - \nu^2)$, $\nu' = \nu/(1 - \nu)$ where E = Young's modulus of concrete and ν = its Poisson ratio. The formation of cracks has no effect on stress σ_1 parallel to cracks, and assuming that no loading change occurs which would change σ_1 during the crack advance, it follows that $\sigma_1' = \sigma_1$. Also, set $\sigma_3 = f_{eq}'$ = equivalent strength, and substitute $G_f = w_c f_t'^2(E^{-1} - E_t^{-1})/2$ as determined from a uniaxial test. From the condition $\Delta U_2 - \Delta U_1 = G_f \Delta a$, it is found that

$$f_{eq}' = c_f \left(\frac{2G_f E'}{w_{ef} r_f} \right)^{1/2} = c_f f_t' \left[\left(1 + \frac{E}{-E_t} \right) \frac{w_c}{w_{ef} r_f} \right]^{1/2},$$

$$r_f = 1 - 2\nu' \frac{\sigma_3}{\sigma_1} > 0 \text{ (vertical stress drop)} \tag{1.22}$$

The strength value f_{eq}' used in analysis must be increased as the element size, w_{ef}, decreases. Furthermore, a compressive normal stress parallel to the crack plane causes a reduction of f_{eq}' or the effective fracture energy. This result agrees with experience. However, the decrease of f_{eq}' due to r might be too strong since, at $\nu \simeq 1/6$, a compression $\sigma_1 = -6\sigma_3$ would reduce the tensile strength to zero, while biaxial failure test data indicate that the tensile strength is nonzero for any ratio σ_3/σ_1. This means that the effective fracture energy is probably also variable, as a function of σ_1/σ_3, which is neglected in Eq. 1.22 (cf. Eq. 1.13). Nevertheless, for $\sigma_1/\sigma_3 \leqslant -6$, the tensile strength is, no doubt, greatly reduced and so Eq. 1.22 might be acceptable for practical purposes. In previous works [6,59,60], coefficient r_f was not used ($r_f = 1$); the effect, however, was almost nil since σ_1/σ_3 was negligible in the examples solved.

Coefficient c_f, which takes into account the nonuniformity of strain distribution enforced in the frontal finite element by its shape function, may be calibrated empirically, so that the results would agree with those obtained from the energy criterion (Eq. 1.33 in the sequel). For a square element consisting of two identical constant strain triangles, $c_f\sqrt{2} = 0.921$ [6], while for that consisting of four identical constant strain triangles (with a central node condensed out), $c_f\sqrt{2} = 0.826$ [59]. For a four-node square with a single-point numerical integration and Flanagan-Belytschko's optimal orthogonal (elastic) hour-glass control [61], $c_f = 0.74$, as determined by P. Pfeiffer at Northwestern University.

If the finite element size w_{ef} is up to a few time w_c then it is best to modify the stress-strain diagram in such a manner that both G_f and f_t' are preserved. This may be achieved by replacing the actual downward slope E_t by an effective one $\tilde{E}_t$ (Figure 1.10d). The condition of equal energy dissipation is $w_c f_t'^2(E^{-1} - E_t^{-1})/2 = w_{ef} f_t'^2(E^{-1} - \tilde{E}_t^{-1})/2$, which yields the rule

$$-\tilde{E}_t = \frac{E}{\frac{w_c}{w_{ef}}\left(1 - \frac{E}{E_t}\right) - 1} \tag{1.22a}$$

Thus, the downward slope $\tilde{E}_t$ must be made steeper as the finite element is made larger. There is a limit for this; a vertical stress drop, for which $1/\tilde{E}_t = 0$, and Eq. 1.22a indicates that this happens when $w_{ef} = w_c(1 - E/E_t)$. So, a change of downward slope (Eq. 1.22) can be used to achieve correct energy dissipation only if

$$w_{ef} \leqslant w_0 = w_c \left(1 + \frac{E}{-E_t} \right) \tag{1.22b}$$

If the finite element needs to be made larger, then one must keep a vertical stress drop and adjust the strength limit according to Eq. 1.22; see Figure 1.10a.

For relatively small structures it may be sometimes desirable to use finite elements smaller than $w_c = 3d_a$ (Figure 1.10f). Leaving aside (for lack of data) the question of how important it is to keep a blunt fracture front, the correct fracture energy may then be preserved by using a downward slope $\tilde{E}_t$ that is milder (less steep) than the actual one, E_t. This slope may again be calculated from Eq. 1.22a, in which $w_c/w_{ef} > 1$. Obviously, there is now no mathematical limit on how small w_{ef} can get. Note that if one reduces only the width of the finite elements in the crack band, permitting these elements to become elongated rectangles (Figure 1.10f), then a reduction of w_{ef} to a very small volume makes this approach equivalent to that of Hillerborg et al. [18], in which one uses a stress displacement relation, the displacement being $\delta = w_{ef}\varepsilon_x$.

Another possibility of preserving the correct fracture energy is to keep the actual downward slope E_t and change the peak stress value from f_t' to f_{eq} (Figure 1.10b). This may be less realistic than the previous method (Eq. 1.22a) for $w_{ef} \leqslant w_0$, but is simpler and avoids the limitation in Eq 1.22b. In this approach the stress-strain diagram remains geometrically similar, and so this approach is easier to implement if one uses a curved

stress-strain diagram. The energy balance condition remains the same as before except that $1/E'$ must now be replaced with $(1 - E/E_t)/E'$. Making this replacement in Eq. 1.22, one obtains

$$f'_{eq} = c_f\left(1 + \frac{E}{-E_t}\right)^{-1/2}\left(\frac{2G_f E'}{w_{ef} r_f}\right)^{1/2} = c_f f'_t\left(\frac{w_c}{w_{ef} r_f}\right)^{1/2} \quad \text{(correct slope } E_t\text{)} \tag{1.23}$$

where again $r_f = 1 - 2\nu'\sigma_3/\sigma_1$. In contrast to Eq. 22, this equation should apply even for small structures (nonlinear fracture range). One should also realize that the sudden stress drop is an inappropriate assumption for dynamic finite element programs since it generates spurious shock waves [62,63,64].

For larger structures, it is found that the present method with an abrupt stress drop gives results which are in excellent agreement with the exact solutions for sharp cracks, and approximate these solutions just as well as the method of sharp interelement cracks. This has been demonstrated by Bažant and Cedolin [59,6,60,7] and one of these demonstrations is shown in Fig. 1.12 in which a nondimensionalized load parameter is plotted versus the crack length, a. The specimen is a rectangular panel with a center crack, loaded by a uniform normal stress at top and bottom. The calculation has been carried out for three different meshes shown in Fig. 1.11, with finite element sizes in the ratios 4 : 2 : 1. (Note that the exact solutions are slightly different for each mesh because the boundary of each mesh was not exactly the same.) We see that, with finer meshes, the present method can be used to obtain linear fracture mechanics solutions.

The energy actually dissipated per unit extension of the crack band in the finite element mesh is $W' = wf'^2_t(E^{-1} - E_t^{-1})/2$, which is proportional to the width w of the frontal finite element. So, by reducing the element size to zero ($w \to 0$), the energy that needs be supplied to produce the fracture becomes vanishingly small if f'_t, E and E_t are constant. This conspicuously demonstrates the irrationality of using the same complete stress-strain diagram regardless of the element size.

The foregoing deductions regarding the effect of element size are based on the premise that the cracking front is single-element wide. This premise is justified by two reasons:

1) If the fracture front is considered to be two or more elements wide, then one finds that a deformation increment of localization type (see Sec. 4.2 in the sequel) consumes negative energy, i.e. the multi-element width of the cracking front is unstable.

2) If the loading step is so small that the strain in only one element goes over the peak stress point within this step, it is impossible to obtain

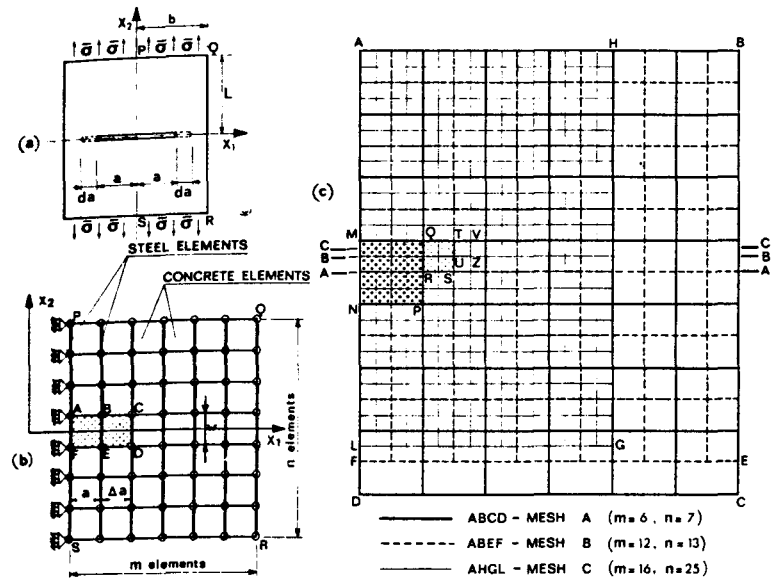

Fig. 1.11. Numerical example of center-cracked rectangular panel and finite element meshes used (after Bažant and Cedolin, 1980).

a multiple-element cracking front. Cracking of one finite element relieves the stress from its neighbor element on the side, and for this reason this neighbor element can never be made to crack in subsequent loading steps. One can get both finite elements to crack only if the loading step is sufficiently large.

In the currently existing large finite element codes, propagation of distributed (smeared) cracking from one element to another is being determined on the basis of the tensile strength criterion. It is well known that such a calculation cannot converge to correct results, since refinement of the element size to zero leads to infinite stress concentrations just ahead of the front cracked element, causing that the load needed for further extension of the crack band tends always to zero. It has not been however generally recognized that the use of the strength criterion can lead to very large errors. According to the numerical results of Bažant and Cedolin [6,59,60], the differences in the results can be as large as 100% when the finite element sizes differ as 4 : 2 : 1. To demonstrate it, some of these results are reproduced in Fig. 1.11, in which the failure load needed to cause further extension of the crack band is plotted for the same panel as in Fig. 1.11 against the length of the crack band. The curves obtained for meshes A, B, C of finite element sizes 4 : 2 : 1 are seen to be very far apart, whereas the curves for the finite element results on the basis of the equivalent strength approach for the abrupt stress drop

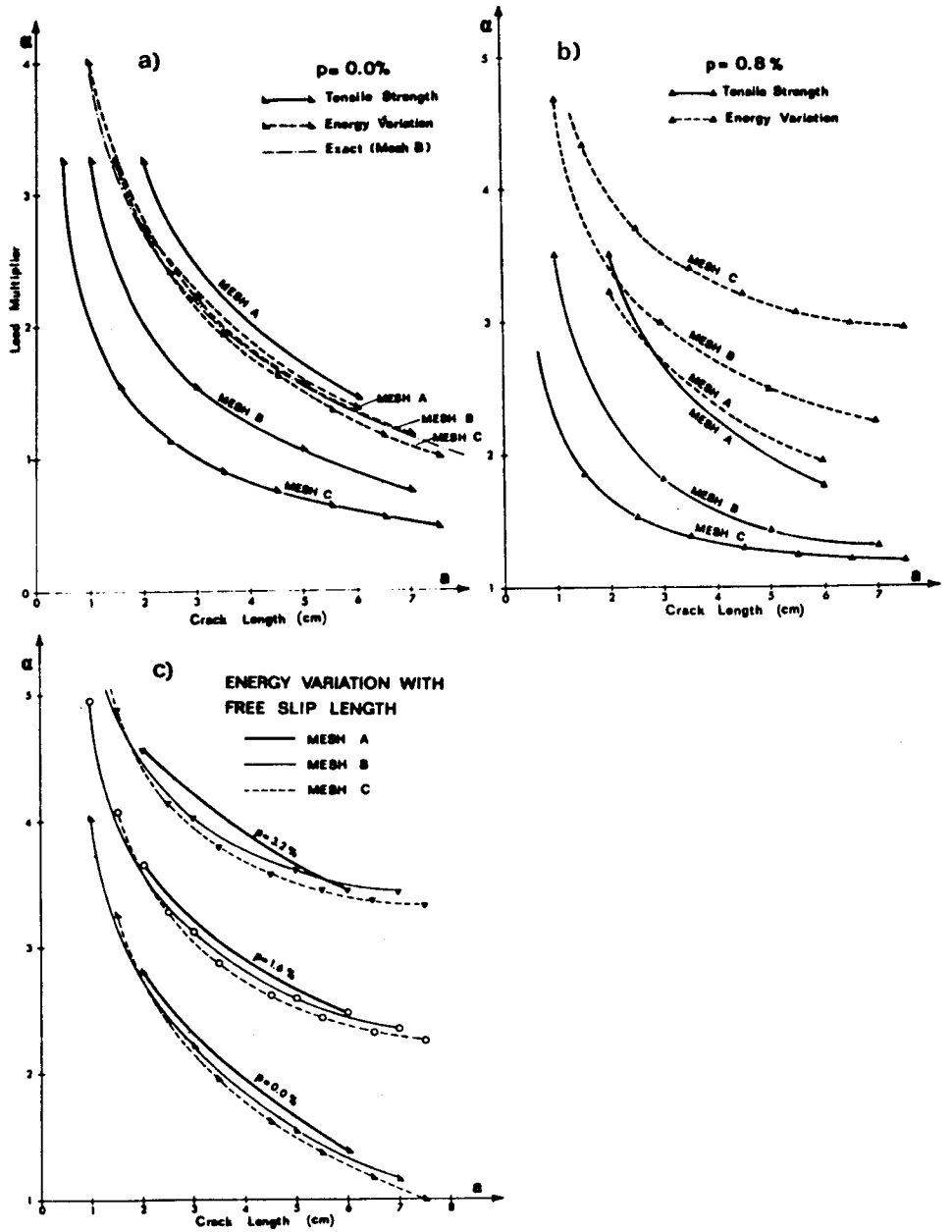

Fig. 1.12. Results for different mesh sizes for the panel from Fig. 1.11 (a) unreinforced, (b) reinforced, no bond slip, (c) various reinforcements, bond slip (after Bažant and Cedolin, 1980), (p = reinforcement ratio).

(as well as those obtained on the basis of energy criterion in Eq. 1.33 below) agree with each other well; see Figure 1.12. The difference between the curves is negligible and tends to zero as the mesh is refined. The curves for the equivalent strength criterion closely agree with those for the energy criterion.

The calculation results in Figure 1.2c further demonstrate that also in the case of gradual strain softening, the finite element results strongly depend on the chosen mesh size, and thus are unobjective. When, however, the downward slope is varied to preserve the same energy, the results for various meshes are about the same; see Figure 1.12c.

The foregoing examples demonstrate that strength criteria are fundamentallly at fault, except for plastic failures, characterized by constant rather than decreasing stress during failure. This is true not only of tensile failure of plain concrete but also of reinforced concrete, and of shear and compression failures whenever they exhibit strain softening. Eventually, it will be necessary to develop fracture mechanics for compression and shear failures of concrete if consistent results, independent of the chosen mesh size, should be achieved.

On the other hand, the use of strength criterion in the literature often yielded results that agreed well with measurements. This must have been due to one of the following two reasons:

(1) The measurements were made on laboratory specimens the size of which was the minimum possible with regard to the aggregate size. In this case, $f'_{eq} \simeq f'_t$ and the strength analysis is correct (see the discussion below Eq. 1.46). However, engineers need to extrapolate from such laboratory structures to much larger real structures, and this is in question.

(2) Many concrete structures are fracture-insensitive, i.e., the tensile strength of concrete has very little effect on the failure load. These include the bending failure of beams or plates (which must be designed, according to ACI Standard 318 [65], so that steel fails plastically before concrete fails in compression), or failure of spiral or tied columns, in which the confinement makes concrete relatively ductile. To determine whether the structure if fracture-insensitive, the analyst needs to analyze his structure twice – once for the actual strength value, and once for a zero strength value. If the results of both analyses are not approximately the same, fracture mechanics analysis is required.

As the size of the structure, and thus the size of the finite element, becomes very large, the value of the equivalent strength (Eq. 1.22 or 1.23) obviously tends to zero. In the limit, the no-tension material is obtained. This approach was pioneered in the mid-1960's by Zienkiewicz et al. as a method for the cracking analysis of large rock masses.

Effect of mesh inclination. In a general situation, the fracture direction need not be parallel to the mesh lines. A smoothly curved or inclined

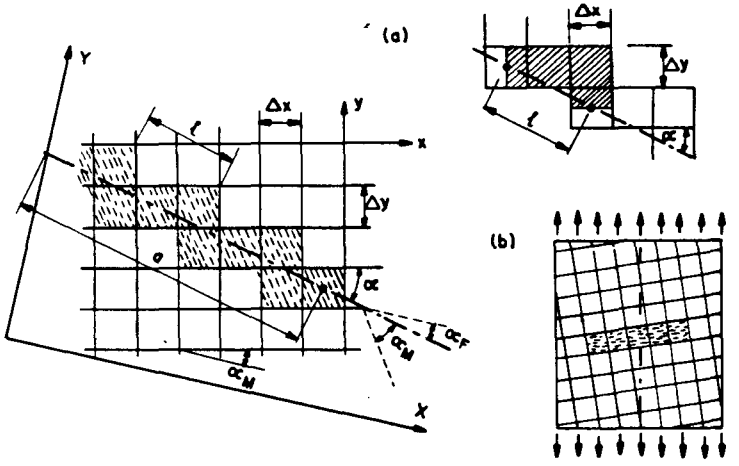

Fig. 1.13. (a) Zig-zag crack band propagation in finite element mesh in skew direction; (b) False bias in crack direction caused by a slightly slanted mesh.

crack or crack band may then be conveniently represented as a zig-zag crack band through the finite element mesh; see Fig. 1.13. Numerical studies indicated that the equivalent strength and energy criteria may still be used but must be modified.

Consider a rectangular mesh of mesh sizes Δx and Δy (Figure 1.13). Let α_F be the orientation angle of the zig-zag crack band (overall fracture direction), α_M be the orientation angle of mesh lines x, and α_C be the direction of the cracks (microcracks) within the finite element (Figure 1.13). To be determined is the effective width w_{ef} of a smooth crack band which is equivalent to the zig-zag band. Consider one cycle, of length l, on the line connecting the centroids of the elements in the zig-zag band. The number of elements per cycle l in the x-direction is $N_x = l \cos \alpha/\Delta x$, and the number of those in the y-direction is $N_y = l \sin \alpha/\Delta y$ where $\alpha = |\alpha_F - \alpha_M|$ $(0° \leqslant \alpha \leqslant 90°)$ (Figure 1.13). The area of the zig-zag band per cycle l is $(N_x \Delta y)\Delta x + (N_y \Delta x)\Delta y$. This area must equal the area $l w_{ef}$ of the equivalent smooth crack band, in order to assure the same energy content (assuming same stresses). This condition yields

$$w_{ef} = \Delta x \sin \alpha + \Delta y \cos \alpha \quad \text{or} \quad w_{ef} = c_\alpha h, \quad c_\alpha = \sqrt{2} \cos(45° - \alpha) \tag{1.24}$$

where the second equation applies to a square mesh $(\Delta x = \Delta y = h)$. Thus, we see that the value of w_{ef} to be substituted into Eqs. 1.22 or 1.23 for the equivalent strength depends on the inclination α of the mesh with regard to the fracture direction. Note also that the correction factor due to α is always between 1.0 and 1.41.

By a similar argument, for a three-dimensional orthogonal mesh of

steps Δx, Δy, Δz, the equivalent width of a three-dimensional zig-zag band may be shown to be

$$w_{ef} = |\nu_1|\Delta x + |\nu_2|\Delta y + |\nu_3|\Delta z \tag{1.25}$$

where ν_1, ν_2, ν_3 are the direction cosines of the normal of the fracture plane (overall fracture direction) with regard to the mesh coordinates.

Instead of Eq. 1.24 for effective width, a somewhat different equation, namely, $w_{ef} = h/\cos \alpha$, was used in previous work based on a different argument. For $\alpha = 0$ and $\alpha = 45°$, this equation gives the same values of w_{ef} as Eq. 1.24, and between 0 and 45° it gives slightly smaller values of w_{ef} (not smaller by more than 17%). However for α close to 90°, the equation $w_{ef} = h/\cos \alpha$ is inapplicable; it cannot be correct when $\alpha \to 90°$ since it would give $w_{ef} \to \infty$, which in turn, would yield $f'_{eq} \to 0$, causing the equivalent strength criterion to always incorrectly indicate that a crack band parallel to the mesh would always jump to the side, perpendicular to the crack direction [66]. Eq. 24 or 25 avoids this problem.

Although the foregoing equations give correct overall energy dissipation by a zig-zag crack band, they do not completely avoid a directional bias due to the mesh as far as determining the direction of individual jumps of the crack band front is concerned. For example, if a square mesh in the center-cracked rectangular panel is slanted, but only moderately so (Figure 1.13b), then the criterion in Eq. 1.24, used in comparison with the maximum principal stress, indicates the crack band to run straight along the mesh line, i.e. in the inclined direction, while correctly it should zig-zag so as to conform to an overall horizontal direction. It appears rather difficult to avoid this type of bias. On the other hand, for a 45° slant of a square mesh, this problem does not occur and the crack band propagates zig-zag in an overall horizontal direction. Various methods to avoid the bias due to the slant of the mesh are being studied [66–68].

The calculation results must be also objective not only with regard to the choice of the element size but also with regard to the choice of mesh inclination. To demonstrate it, the example shown in Figure 1.11 has been calculated [60] for a square mesh whose sides are inclined at 45° with regard to the side of the rectangular panel. The results of this calculation are shown in Figure 1.15, in which case 1b corresponds to this inclined mesh and case 1a to a square mesh whose sides are parallel to the sides of the panel. An excellent agreement of these two calculations is seen. Similar agreement has been found for the inclined meshes when the element size is varied [60]. A 26.6° inclination of the square mesh has also been considered, and the results were again satisfactory, although the scatter was larger than for the 45° inclination [60].

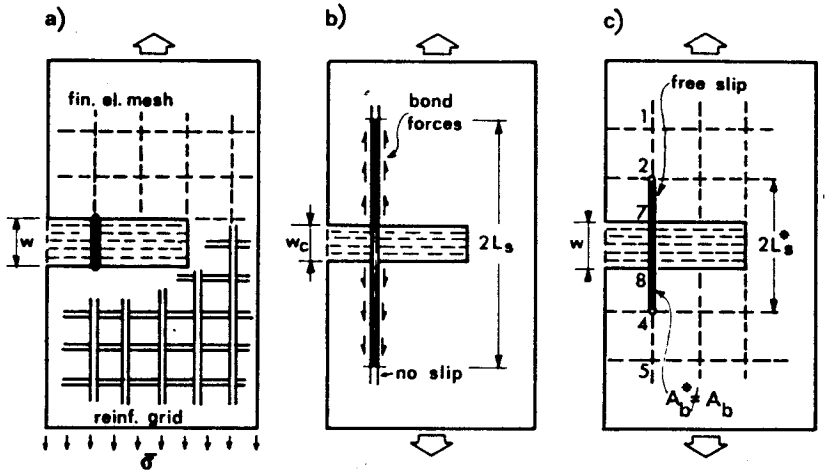

Fig. 1.14. Illustration of bond slip and equivalent free bond slip length L_s^* (after Bažant and Cedolin, 1980).

Effect of reinforcement and bond slip. It has been customary in finite element analysis of reinforced concrete to assume that the steel bars are rigidly attached to concrete in the nodes of the mesh. This treatment is, however, not only physically unjustified but also unobjective with regard to the choice of mesh, and causes incorrect convergence. The bars connecting the nodes on the opposite sides of the crack band represent an elastic connection, the stiffness of which varies inversely as the distance between the nodes, i.e., the width w of the crack band. Thus, as the mesh size is refined to zero (and the crack band width tends to zero), the stiffness of the connection across the crack band increases to infinity, which prevents opening of the crack band. So it is clear that no cracking can be obtained in the limit of a zero element size.

The effect of the mesh size on the results is demonstrated in Figure 1.12b where the load parameter is plotted vs. crack length a for a rectangular panel [59]. The panel is the same as before, but is reinforced by regularly and densely spaced vertical bars of various reinforcement ratios p. We see that the results for the three meshes of sizes 4 : 2 : 1 differ greatly, not only for the constant strength criterion but also for the energy criterion.

To obtain an objective and properly convergent formulation, one must take into account the bond slip. The bond slip occurs over a certain length, L_s (Figure 1.14). The most realistic treatment of bond slip would call for using separate nodes for concrete and steel connected by some nonlinear linkage elements representing forces transmitted by bond. However, this approach would be too cumbersome. In the spirit of the

approximations involved in the smeared crack band model, it should be sufficient to introduce the bond slip in such a way that the stiffness of the connection provided by the steel bars crossing the crack band would be roughly correct and independent of the finite element mesh.

Thus, to simplify the formulation, the actual curvilinear variation of the bond forces and the axial forces in the bars may be replaced by an idealized piece-wise constant variation of the bond force and the corresponding piece-wise linear variation of the actual axial force in the bars (Figure 1.14). The latter may further be replaced by a piece-wise constant variation of the axial force, such that the overall extension of the bar over the distance of the bond slip would be roughly the same.

An estimate of L_s will be made. Let A_b = cross section area of bar. Since the bar force $A_b\sigma_s$ must equilibrate the remote bar force $A_b\sigma_s'$, plus the bond force $U_b'L_s$, the bond slip length is $L_s = (\sigma_s - \sigma_s')A_b/U_b'$ (Figure 1.14) where U_b' = ultimate bond force per unit length of bar, as determined by pull-out tests; σ_s, σ_s' = tensile stress in the steel bar at the point where it crosses the crack band, and at the end of the slipping segment, respectively. Furthermore, σ_s' may be approximately related to σ_s; $A_b\sigma_s$ must equal the force per bar carried jointly by steel and concrete at the end of the slipping segment where the strain, $\varepsilon_s = \sigma_s'/E_s$, is the same for concrete and steel. Thus $[E_s p + E_c(1-p)]\sigma_s'/E_s = p\sigma_s$ or $\sigma_s' = \sigma_s n' p/(1-p+n'p)$ in which $n' = E_s/E_c$ = ratio of elastic moduli of steel and concrete, and $p = A_s/(A_c + A_s)$ = steel ratio. The following result is obtained [59]:

$$L_s = \frac{A_s}{U_b'}(\sigma_s - \sigma_s') \simeq \frac{A_b}{U_b'}\frac{1-p}{1-p+n'p}\sigma_s. \tag{1.26}$$

This equation gives the bond-slip length as a fixed property characteristic of the steel-concrete composite.

For the purpose of finite element analysis, the actual bond-slip length L_s may be replaced by some modified length L_s^* such that the steel stress over this length is uniform and the slip of steel bar within concrete may be considered as free. The length L_s^* is determined from the condition that the extension of the steel bar over the length L_s would remain the same. In this manner, the following expression for the equivalent free bond-slip length can be derived [59]:

$$L_s^* = \frac{A_b^*(1-p)}{2[A_b(1-p+pn) - pnA_b^*]}\left[L_s + w_0\left(1 - \frac{s_c}{4L_s}\right)\right] \tag{1.27}$$

where w = width of the element-wide crack band, s_c = spacing of cracks within the crack band ($s_c \simeq d_a$) and A_b^* = the cross-section area of bar

chosen for computations. One may conveniently choose such A_b^* that Eq. 1.27 give a length which coincides with a distance between two nodes of the mesh. As a crude approximation

$$L_s^* = \tfrac{1}{2}L_s \qquad \text{if} \quad A_b^* = A_b. \tag{1.28}$$

Using Eq. 1.27, the finite element analysis of the center-cracked rectangular panel, the same one as before (Figure 1.11), yields consistent results when finite elements of different sizes are used (Figure 1.12c) [60]. Further, it has been demonstrated [60] that the use of different mesh sizes for a reinforced panel yields consistent results even when the mesh is inclined; see Figure 1.15 for a 45° mesh inclination and Figure 1.16 for a 26.6° inclination.

The formula for the equivalent strength of concrete needs to be generalized to reflect the bond slip effect. The stiffness of the concrete-steel composite over band width w_c for loading normal to the crack band may be written as $C_1 = (1-p^*)E_c/w_c + c_p p' E_s/L_s'$ where E_s, E_c = Young's moduli of steel and concrete, $L_s' = L_s^* \cos\alpha_s$ = actual free bond-slip length projected on the normal to the crack band, α_s = angle of the reinforcing bars with this normal, $p' = p^* \cos^2\alpha_s$ where $\cos^2\alpha_s$ represents a correction of stiffness of the steel bars due to their inclination (satisfying the condition that the stiffness be zero when $\alpha_s = 0$), and c_p = empirical correction factor introducing the effect of deformation of concrete outside the element that cracks but lies within length L_s^*. The deformation f_{eq}'/C_1 should equal the deformation f_{eq}^0/C_0 where f_{eq}^0 = equivalent strength in absence of reinforcement, as given before, and $C_0 = E_c(1-p')/w_c$ = stiffness of concrete across the band width w_c. From the condition $f_{eq}'/C_1 = f_{eq}^0/C_0$, the following expression for f_{eq}' for sudden stress drop may be obtained after algebraic rearrangements:

$$f_{eq}' = c_f \left(\frac{2G_f E_c}{w_{ef} r_f}\right)^{1/2} \left(1 + c_p \frac{E_s}{E_c}\frac{p}{L^*}\cos\alpha_s\right) \tag{1.29}$$

if $1-p$ is replaced by 1 (normally $p \ll 1$). This formula is the same as that derived in [60]. by using the expression for the asymptotic displacement field near the tip of an equivalent sharp crack [40], except for one difference: The dependence on α_s. By solving a number of examples for reinforced panels on the basis of the energy criterion, and requiring that the use of f_{eq}' would yield approximately the same results, a table of optimum values of c_p for various α_p was set up [60]; approximately, $c_p \approx 0.7$ for all α_s. Note that Eq. 1.29 satisfies the obvious condition that f_{eq}' must become the same as given by Eq. 1.22 when $\alpha_s = 90°$, or $p = 0$, or $E_s = 0$, or $L^* \to \infty$.

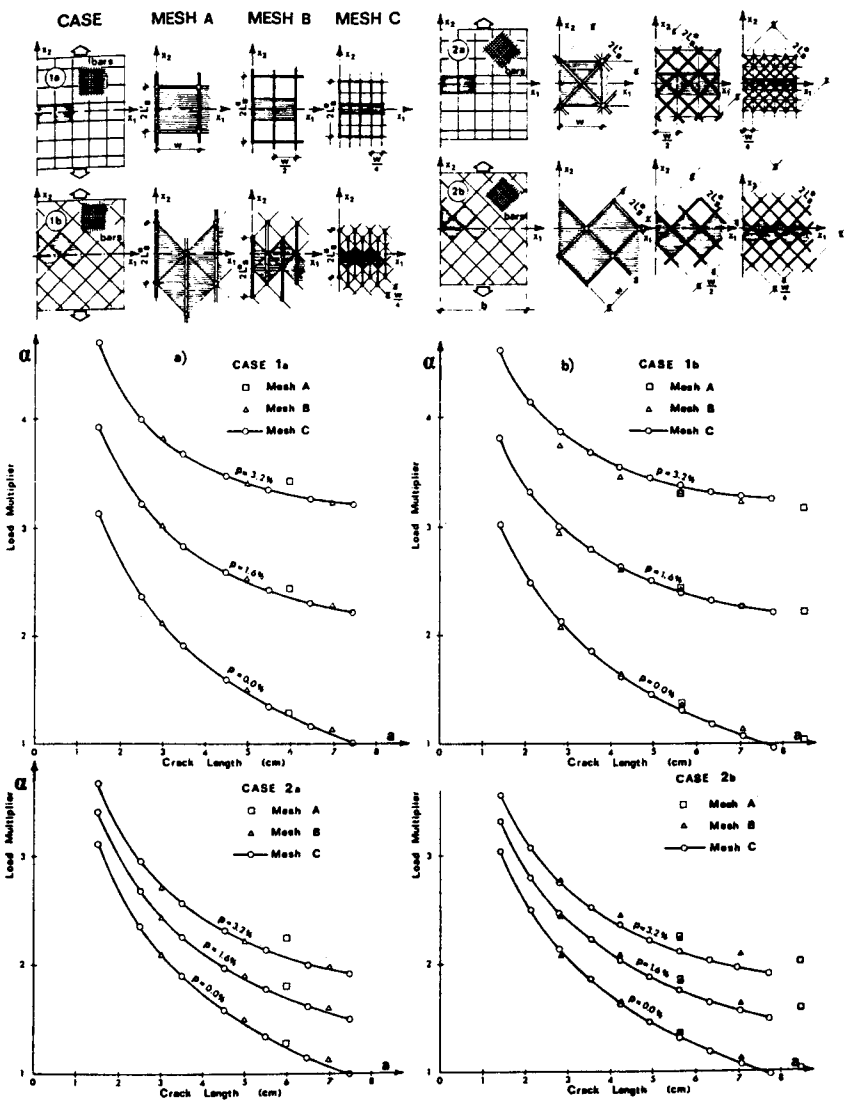

Fig. 1.15. Results for various finite element sizes for zig-zag crack band in a 45° inclined mesh and parallel mesh, both for energy criterion and equivalent strength (after Bažant and Cedolin, 1983).

A more realistic continuum treatment of reinforcement and bond slip would be to approximate the reinforcing net by a continuum that is allowed to slip against the continuum representing concrete, and consider that the distributed (volume) forces transmitted between the two continua depend on the relative slip displacement. This would be, however, more complicated.

chosen for computations. One may conveniently choose such A_b^* that Eq. 1.27 give a length which coincides with a distance between two nodes of the mesh. As a crude approximation

$$L_s^* = \tfrac{1}{2}L_s \qquad \text{if} \quad A_b^* = A_b. \tag{1.28}$$

Using Eq. 1.27, the finite element analysis of the center-cracked rectangular panel, the same one as before (Figure 1.11), yields consistent results when finite elements of different sizes are used (Figure 1.12c) [60]. Further, it has been demonstrated [60] that the use of different mesh sizes for a reinforced panel yields consistent results even when the mesh is inclined; see Figure 1.15 for a 45° mesh inclination and Figure 1.16 for a 26.6° inclination.

The formula for the equivalent strength of concrete needs to be generalized to reflect the bond slip effect. The stiffness of the concrete-steel composite over band width w_c for loading normal to the crack band may be written as $C_1 = (1-p^*)E_c/w_c + c_p p' E_s/L_s'$ where E_s, E_c = Young's moduli of steel and concrete, $L_s' = L_s^* \cos\alpha_s$ = actual free bond-slip length projected on the normal to the crack band, α_s = angle of the reinforcing bars with this normal, $p' = p^* \cos^2\alpha_s$ where $\cos^2\alpha_s$ represents a correction of stiffness of the steel bars due to their inclination (satisfying the condition that the stiffness be zero when $\alpha_s = 0$), and c_p = empirical correction factor introducing the effect of deformation of concrete outside the element that cracks but lies within length L_s^*. The deformation f_{eq}'/C_1 should equal the deformation f_{eq}^0/C_0 where f_{eq}^0 = equivalent strength in absence of reinforcement, as given before, and $C_0 = E_c(1-p')/w_c$ = stiffness of concrete across the band width w_c. From the condition $f_{eq}'/C_1 = f_{eq}^0/C_0$, the following expression for f_{eq}' for sudden stress drop may be obtained after algebraic rearrangements:

$$f_{eq}' = c_f \left(\frac{2G_f E_c}{w_{ef} r_f}\right)^{1/2} \left(1 + c_p \frac{E_s}{E_c}\frac{p}{L^*}\cos\alpha_s\right) \tag{1.29}$$

if $1-p$ is replaced by 1 (normally $p \ll 1$). This formula is the same as that derived in [60]. by using the expression for the asymptotic displacement field near the tip of an equivalent sharp crack [40], except for one difference: The dependence on α_s. By solving a number of examples for reinforced panels on the basis of the energy criterion, and requiring that the use of f_{eq}' would yield approximately the same results, a table of optimum values of c_p for various α_p was set up [60]; approximately, $c_p \simeq 0.7$ for all α_s. Note that Eq. 1.29 satisfies the obvious condition that f_{eq}' must become the same as given by Eq. 1.22 when $\alpha_s = 90°$, or $p = 0$, or $E_s = 0$, or $L^* \to \infty$.

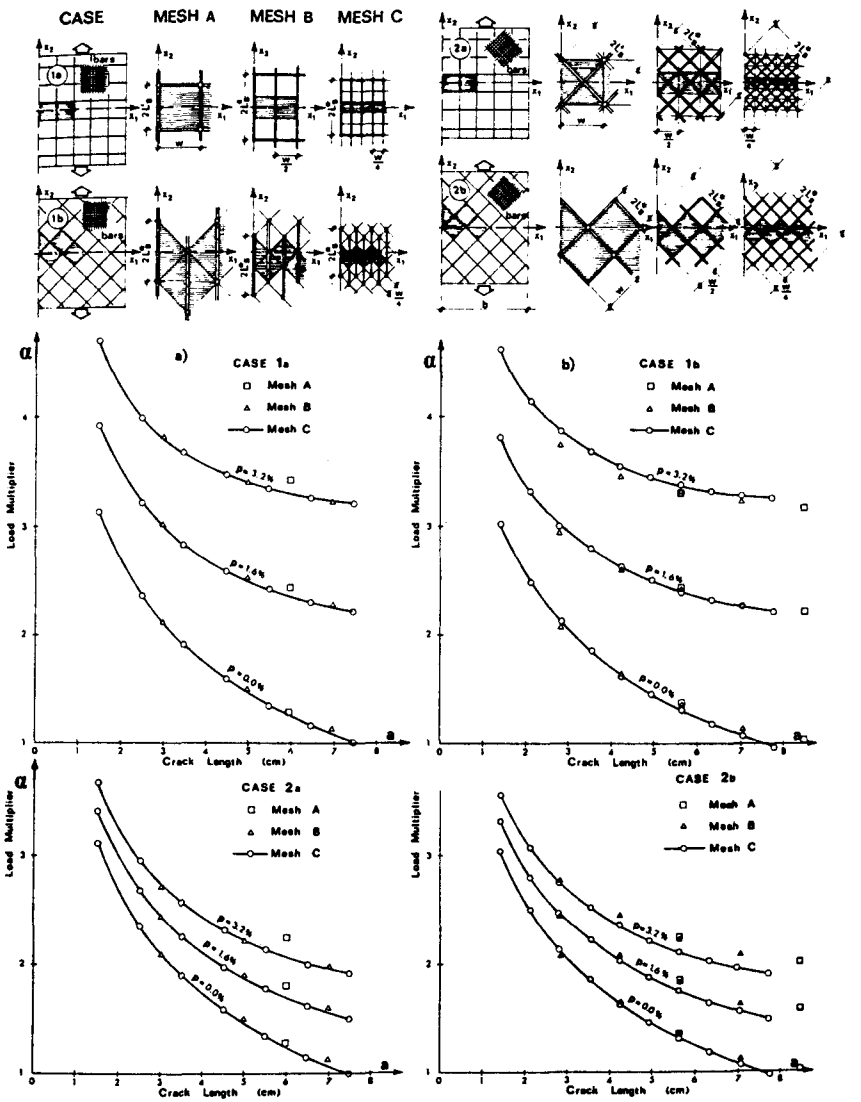

Fig. 1.15. Results for various finite element sizes for zig-zag crack band in a 45° inclined mesh and parallel mesh, both for energy criterion and equivalent strength (after Bažant and Cedolin, 1983).

A more realistic continuum treatment of reinforcement and bond slip would be to approximate the reinforcing net by a continuum that is allowed to slip against the continuum representing concrete, and consider that the distributed (volume) forces transmitted between the two continua depend on the relative slip displacement. This would be, however, more complicated.

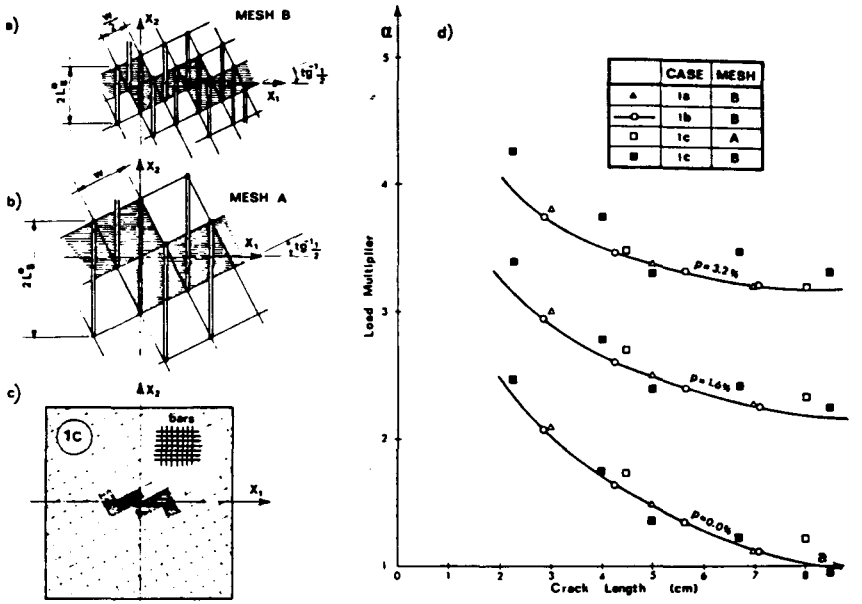

Fig. 1.16. Results for various finite element sizes for zig-zag crack band in a 26.6° inclined mesh, both for energy criterion and equivalence strength (after Bažant and Cedolin, 1983).

1.4 Energy considerations

Energy criterion for crack bands. When a structure is so large that a sudden stress drop may be considered, and fracture energy is the only important fracture property, the energy criterion may be directly implemented in a finite element program [6,59]. One needs to evaluate in the program the amount of energy, ΔW, that is available for fracture as the crack bands extends by length Δa of one finite element.

A similar problem is the extension of a notch, and energy analysis of this case was made by Rice [69]. The case of a crack band differs from that of a notch by the fact that, as the element of volume ΔV ahead of the crack front gets cracked (Figure 1.17), it loses merely the capability of transmitting stresses across the crack plane, but remains capable of carrying normal stresses parallel to the crack planes. Moreover, one must take into account the fact that the volume ΔV may contain reinforcing bars which, in the uncracked state, transmit to concrete interface forces. We consider now the steel-concrete composite, and distinguish steel and concrete by subscripts s and c. Assuming the material to be elastic (and the applied forces to be conservative), the variation of the potential energy of the structure due to the extension of the crack band into volume ΔV is independent of the path in which this extension happens.

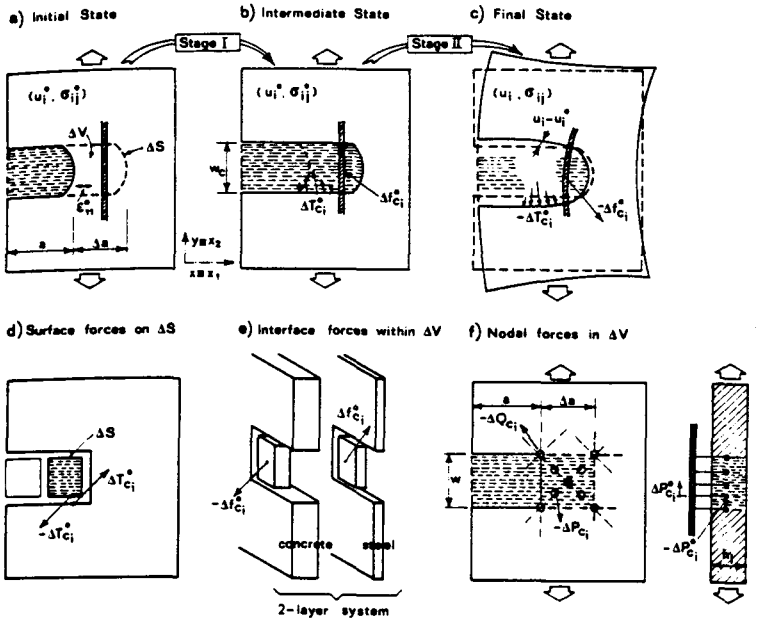

Fig. 1.17. Assumed stages of extension of crack band to explain energy criterion (after Bažant and Cedolin, 1980).

Consequently, as in [6], the crack extension may be decomposed in two stages.

Stage I. Cracks are created in concrete inside volume ΔV of the element ahead of the crack in the direction of principal tensile stress (Figure 1.17b), while, at the same time, the deformations and stresses in the rest of the body are imagined to remain fixed (frozen). This means that one must introduce surface tractions $\Delta T_{c_i}^0$ applied on the boundary ΔS of volume ΔV, and distributed forces $\Delta f_{c_i}^0$ applied at the concrete-steel interface, such that they replace the previous action of concrete that cracked upon the remaining volume $V - \Delta V$ and upon the reinforcement within ΔV.

Stage II. Next, forces $\Delta T_{c_i}^0$ and $\Delta f_{c_i}^0$ (Figure 1.17c) are released (unfrozen) by gradually applying the opposite forces $-\Delta T_{c_i}^0$ and $-\Delta f_{c_i}^0$, reaching in this way the final state.

Let u_i^0 and ε_{ij}^0 be the displacements and strains before the crack band advance, and let u_i and ε_{ij} be the same quantities after the crack band advance. For the purpose of analysis, the reinforcement may be imagined to be smeared in a separate parallel layer undergoing the same strains as concrete. The interface forces between steel and concrete, $\Delta f_{c_i}^0$, then appear as volume forces applied on the concrete layer.

Upon passing from the initial to the intermediate state (Stage I), the strains are kept unchanged, while the mechanical properties of concrete

inside ΔV are varied. Thus, the corresponding stress changes in concrete in ΔV are given by $\Delta\sigma_{11}^{c} = \sigma_{11}^{c^0} - E_c'\varepsilon_{11}^0 = (\varepsilon_{11}^0 + \nu_c'\varepsilon_{22}^0)E_c'/(1-\nu_c'^2) - E_c'\varepsilon_{11}^0$; $\Delta\sigma_{22}^{c} = \sigma_{22}^{c^0}$; $\Delta\sigma_{12}^{c} = \sigma_{12}^{c^0}$. Here, $\sigma_{ij}^{c^0}$ denotes the stress fraction carried before cracking by concrete alone, defined as force in concrete per unit area of the steel-concrete composite; E_c and ν_c are the Young's modulus and Poisson's ratio of concrete. The conditions $E_c' = E_c$ and $\nu_c' = \nu_c$ apply to plane strain and $E_c' = E_c/(1-\nu_c^2)$ and $\nu_c' = \nu_c/(1-\nu_c)$ to plane strain. Assuming that cracks in concrete propagate in the direction of the principal stress just ahead of the crack, one has $\Delta\sigma_{12}^{c} = \sigma_{12}^{c^0} = 0$ in the above expressions. The change in potential energy of the system during Stage I in Figure 1.17b is given by the elastic energy initially stored in ΔV and released by cracking, i.e.,

$$\Delta W = -\int_{\Delta V} \tfrac{1}{2}\left(\sigma_{ij}^{c^0}\varepsilon_{ij}^0 - E_c'\varepsilon_{11}^{0^2}\right)\mathrm{d}V. \tag{1.30}$$

The change in potential energy during Stage II in Figure 1.17 is given by the work done by the forces $\Delta T_{c_i}^0$ and $\Delta f_{c_i}^0$ while they are being released, i.e.,

$$\Delta L = \int_{\Delta S} \tfrac{1}{2}\Delta T_{c_i}^0\left(u_i - u_i^0\right)\mathrm{d}S + \int_{\Delta V} \tfrac{1}{2}\Delta f_{c_i}^0\left(u_i - u_i^0\right)\mathrm{d}V. \tag{1.31}$$

Coefficients 1/2 must be used because, for a sufficiently small Δa, the forces T_{c_i} and f_{c_i} vary almost linearly during Stage II and reduce to zero at the end of Stage II.

Not all of the energy that is supplied to the element that cracks from the rest of the structure and from the unloading of concrete between the cracks is available for producing new crack surfaces. Part of this energy is consumed by the bond slip of reinforcing bars during cracking within volume ΔV. This part may be expressed [60] as:

$$\Delta W_b = \int_s U_b'\delta_b \mathrm{d}s \tag{1.32}$$

where δ_b represents the relative tangential displacement between the bars and the concrete, U_b' is the average bond force during displacement δ_b per unit length of the bar (force during the slip) and s is the length of the bar segment within the fracture process zone w_c (and not within volume ΔV since the energy consumed by bond slip would then depend on the chosen element size and would thus spoil the objectivity and proper convergence of the fracture criterion). Approximately, $U_b' \simeq$ ultimate bond force.

The energy criterion for the crack band extension may now be

expressed as

$$\begin{aligned}\Delta U = G_f\Delta a - \Delta W - \Delta L - \Delta W_b &> 0 \text{ stable}\\ &= 0 \text{ critical}\\ &> 0 \text{ unstable}\end{aligned} \tag{1.33}$$

where ΔU = energy that must be externally supplied to the structure to extend the crack band of width h by length Δa. (ΔU = total energy in the case of rapid, or adiabatic, fracture, and ΔU = Helmholtz's free energy in the case of slow, or isothermal, fracture.) If $\Delta U > 0$, then no crack extension can occur without supplying energy to the structure, and so the crack band is stable, does not propagate. If $\Delta U < 0$, crack band extension provokes a spontaneous energy release by the structure, which is an unstable situation, and so the crack extension must happen; the crack then extends in a dynamic manner, and the excess energy $-\Delta U$ is transformed into kinetic energy. If $\Delta U = 0$, no energy needs to be supplied and none is released, and so the crack band may extend in a static manner; in this case $G_f + \Delta W_b/\Delta a = (\Delta W + \Delta L)/\Delta a$ = finite difference approximation to the energy release rate of the structure. For this approximation to be second-order accurate, the corresponding crack band length a should be considered to reach up to the centroid of the frontal element that undergoes cracking.

For practical calculation, the volume integral in Eq. 1.30 needs to be expressed in terms of nodal displacements using the shape functions of the finite element. The boundary integral in Eq. 1.31 is evaluated from the change of nodal forces acting on volume ΔV from the outside [59]. Among the terms in Eq. 1.33, ΔW and ΔW_b normally are relatively small and often may be neglected, yielding $\Delta L/\Delta a = G_f$ as the approximate energy criterion [70].

The energy ΔL released from the surrounding body into ΔV may be, alternatively, also calculated as the difference between the total strain energy contained in all finite elements of the structure before and after the crack advance. According to the principle of virtual work, the result is exactly the same as that from Eq. 1.31 [6,59]. This calculation is possible, however, only if the structure is perfectly elastic whereas Eq. 1.31 is correct even for inelastic behavior (assuming Δa to be so small that T_{c_i} and f_{c_i} vary almost linearly during Stage I). It should also be mentioned that Y.T. Pan, A. Marchertas and coworkers at Argonne National Laboratory [66,71] calculate ΔL in their finite element analyses (using the crack band approach) by means of the J-integral. They keep the integration contour the same for various crack lengths. Their calculation yields the same ΔL because their integration contour passes only

through the elastic part of the structure (except for crossing the crack band behind the front where, however, the stresses are almost zero).

In the case of a zig-zag, inclined crack band, the value of Δa in Eq. 1.33 must be replaced by the effective extension Δa_{ef} in the direction of the equivalent smoothed crack band. The notation from Figure 1.13a will be adopted. Similarly to the derivation of Eq. 1.24, assume that Δa_{ef} is the same for each crack band advance within the cycle l, whether the advance is in the x- or y-direction. Then $\Delta a_{ef} = l/N$ where $N = N_x + N_y$ = number of elements per cycle l (Figure 1.13a). This condition yields

$$\Delta a_{ef} = \left(\frac{\cos \alpha}{\Delta x} + \frac{\sin \alpha}{\Delta y} \right)^{-1} \quad \text{or}$$

$$\Delta a_{ef} = \frac{h}{\sqrt{2}\, \cos(45^\circ - \alpha)}, \quad (0 \leqslant \alpha \leqslant 90^\circ) \tag{1.34}$$

where the first equation applies to any rectangular mesh, and the second one to a square mesh ($\Delta x = \Delta y = h$).

Various numerical examples confirm the use of Eq. 1.34 (or some similar equation) is objective in that it gives results that are essentially independent of the choice of the mesh [66–68].

Strain localization instability and interpretation of tensile test. The formation of fracture through a gradual deformation of a finite fracture process zone may be treated as an instability of a nonlinear continuum, in which a uniformly distributed strain localizes into a band of finite width, w_c, at the boundary of which there is a jump in the value of strain while the stress is continuous. With regard the shear failures in an infinite medium, the concept of strain-localization instability was analyzed in detail by Rice [72] and others, with particular attention to the effect of geometric nonlinearities. A stability analysis of strain localization in tensile failures, with particular attention to finite size bodies and to a combination of strain-softening and unloading was presented in [4,5].

Following previous work [5], it is instructive to analyze the failure of a uniformly stressed specimen subjected to uniaxial tension (Figure 1.18). Such a specimen may serve as an approximate model for the fracture process zone. The specimen is loaded through a spring of spring constant C which represents either the spring constant of a testing machine per unit cross section area of the specimen, or the stiffness (per unit area) of the elastic support provided to the fracture process zone by the surrounding structure (the dimension of C is N/m per m^2, i.e., N/m^3). Let the cross section of the specimen be $A = 1$. The appearance of the crack band in the specimen may be considered as a sudden finite jump by distance

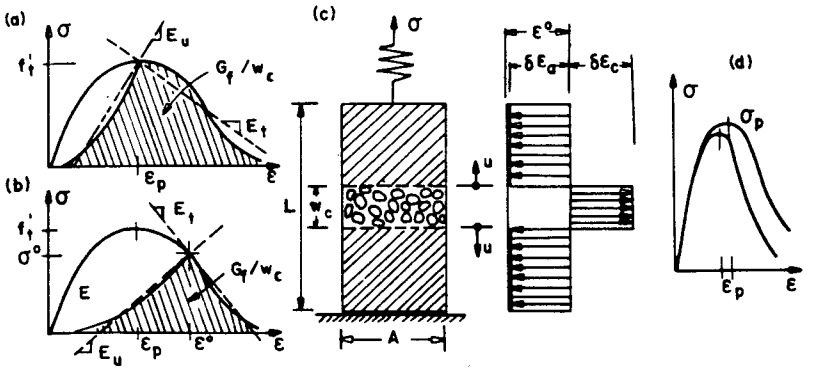

Fig. 1.18. (a–c) Strain-localization in a tensile specimen serving as model for fracture process zone; (d) possible effect of size on stress-strain diagram.

$\Delta a = 1$ in which the front of the crack band moves from the left face to the right face of the specimen (Fig. 1.18). For a uniaxial stress state of an unreinforced specimen of length L, Eqs. 1.30 and 1.31 take the form

$$\Delta W = \frac{w_c}{2} \sigma^0 \varepsilon^0 = \frac{w_c}{2} \sigma^0 \frac{\sigma^0}{\bar{E}_u} \tag{1.35}$$

$$\Delta L = \tfrac{1}{2}\sigma^0 (\Delta u - \Delta u_0) = \tfrac{1}{2}\sigma^0 \left[(L - w_c) \frac{\sigma^0}{\bar{E}_u} + \frac{\sigma^0}{C} \right] \tag{1.36}$$

in which σ and ε are the axial stress and strain; $\Delta u - \Delta u_0$ is the change in the relative displacement between the opposite face of the crack band of width w_c; and $\bar{E}_u$ is the average unloading modulus (Figure 1.18c).

Alternatively, ΔW can be calculated from the changes of strains ε_c in the crack band and c_a outside the crack band. To satisfy equilibrium in the tensile specimen in Figure 1.18c, the stress change $\delta\sigma$ must be the same inside and outside the crack band, and thus

$$\delta\varepsilon_c = \delta\sigma / E_t, \quad \delta\varepsilon_a = \delta\sigma / E_u. \tag{1.37}$$

The energy consumed in the crack band and the energy released from the rest of the specimen may now be calculated as

$$\Delta U_c = \frac{w_c}{2} \delta\sigma \delta\varepsilon_c = w_c \frac{(\delta\sigma)^2}{-2E_t} \tag{1.38}$$

$$\Delta U_a = \tfrac{1}{2}\delta\sigma\left[(L - w_c)\delta\varepsilon_a + \frac{\delta\sigma}{C}\right] = (L - w_c)\frac{(\delta\sigma)^2}{2E_u} + \frac{(\delta\sigma)^2}{2C}. \tag{1.39}$$

Expressing now the stability conditions similarly to Eq. 1.33, one has

$$\begin{aligned} \Delta U = \Delta U_c - \Delta U_a &> 0 \text{ stable} \\ &= 0 \text{ critical} \\ &< 0 \text{ unstable} \end{aligned} \tag{1.40}$$

Considering a finite stress change from σ^0 to 0, i.e., $\delta\sigma = -\sigma^0$, for which E_u and E_t in Eqs. 1.38 and 1.39 must be replaced with the average unloading modulus $\bar{E}_u$ and with the average tangent modulus $\bar{E}_t$ ($\bar{E}_t < 0$), respectively, one may substitute Eqs. 1.33 and 1.35–39 into the criticality condition $\Delta U = \Delta U_c - \Delta U_a = 0$. The resulting equation involves G_f, and solving it for G_f one gets

$$\bar{G}_f = \frac{w_c}{2}\left(\frac{1}{\bar{E}_u} - \frac{1}{-\bar{E}_t}\right)\sigma^{0^2} \tag{1.41}$$

in which a bar is attached to G_f to indicate that this is an apparent fracture energy value. It is not a constant since it depends on the stress σ^0 at which the fracture begins, which is governed by an incremental stability condition and is not necessarily equal to the peak stress σ_p.

In case that the instability which produces fracture happens right at the peak stress point, Eq. 1.41 provides

$$G_f = \frac{w_c}{2}\left(\frac{1}{\bar{E}_u} + \frac{1}{-\bar{E}_t}\right)\sigma_p^2 \tag{1.42}$$

which is a constant and represents the fracture energy value corresponding to the value used in the fracture model to fit test data. The value of G_f is characterized by the cross-hatched area in Figure 1.18a limited by the unloading and the softening branches emanating from the peak stress point.

When a curved stress-strain diagram is considered, one should in general, distinguish two types of instability: incremental instability (in the small, tangential) and instability in the large. The former concerns infinitely small displacements, the latter concerns complete failure. The value of σ^0 at which the instability occurs may be determined from Eq. 1.40 by substituting Eqs. 1.38 and 1.39 in which, for the incremental instability, one uses the incremental moduli E_t and E_u, and for the instability in the large, one uses the $\bar{E}_t$ and $\bar{E}_u$ instead. This yields the

critical states [4,3]:

$$\frac{-E_t}{E_u} = \left(\frac{L}{w_c} - 1 + \frac{E_u}{Cw_c}\right)^{-1} \text{ (incremental)} \tag{1.43}$$

$$\frac{-\bar{E}_t}{\bar{E}_u} = \left(\frac{L}{w_c} - 1 + \frac{\bar{E}_u}{Cw_c}\right)^{-1} \text{ (in the large).} \tag{1.44}$$

As the strain in a tensile specimen is increased, E_t, E_u, $\bar{E}_t$ and $\bar{E}_u$ all vary as a function of strain ε. Two types of failure may occur: (1) either the incremental critical state (Eq. 1.43) is reached first, or (2) the critical state in the large (Eq. 1.44) is reached first. In the first case, failure is static and occurs when Eq. 1.44 becomes satisfied. In the second case, failure cannot happen statically, however when Eq. 1.43 is satisfied later, there is an excess energy ($-\Delta U$) for the instability in the large, and then the failure occurs dynamically as a snap-through instability, $-\Delta U$ being converted into kinetic energy.

Considering the stress-strain diagram to be bilinear and E_u to be constant (Fig. 1.2) has the advantage that failure instability occurs always at the peak stress point. The fracture energy G_f is then constant and equals the entire area under the tensile stress-strain diagram. Whether this simplification is adequate for practical analysis of concrete structures should be examined more closely.

From Eqs. 1.43 and 1.44 it is noted that when the loading frame is very soft ($C \to 0$), or when the specimen is very long ($L/w_c \to 0$), the strain localization starts at $E_t = 0$, i.e., at the peak stress point. When the loading frame is very stiff ($C \to \infty$), and when the specimen is very short ($L = w_c$), Eq. 1.43 indicates a large magnitude of $|E_t|$, and so instability never occurs. These are the requirements for being able to measure the complete stress-strain curve. Eqs. 1.43 and 1.44 may be used also to calculate the stiffness C of the loading frame needed to carry out tensile tests with stable strain softening.

The analysis of strain localization sheds light on the interpretation of the direct tensile test. The question is whether the strain can be evaluated from the measured displacement assuming the strain distribution to be uniform. The conditions in Eqs. 1.43 and 1.44 answer this question in the affirmative. Indeed, if the stress can be measured, it means that specimen is not unstable, since otherwise measurement would be impossible. And if it is not unstable, it means that the strain localization has not occurred, i.e., the strain must be uniform (in the macroscopic sense, of course; we do not consider microstresses here). So, in a stable direct tensile test, the strain-softening zone can be wider than w_c, which is a different situation than in fracture process zones. There, since fracture is being formed, the

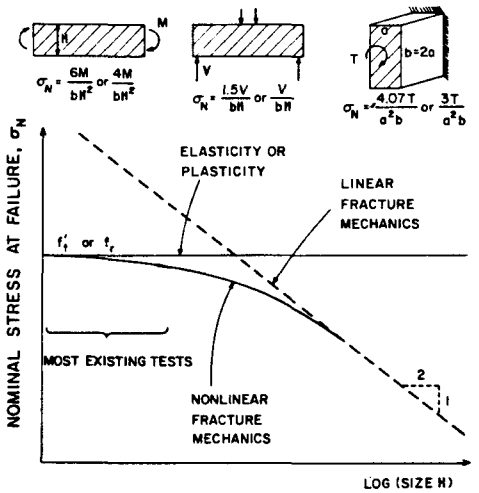

Fig. 1.19. Structural size effect.

strain must localize, and a constant width w_c of the strain-localization zone may be a good approximation.

A related question, raised by some experimentalists, is whether not only the failure point, but also the shape of the stress-strain diagram (Figure 1.18d) is affected by the stiffness of the loading frame. In a deterministic analysis, the stress-strain diagram should be considered as unique, unaffected by the loading frame. The analysis in [5] shows that observed variations of peak stress σ_p (tensile strength) as a function of machine stiffness can be explained by the effect of statistical inhomogeneity of the material on strain localization. These effects are significant only when the material is very inhomogeneous (poor quality concrete).

Structural size effect. The main purpose of fracture mechanics is to correctly capture the size effect in the ultimate load capacity of a structure. The size effect may be illustrated by considering structures of different sizes but the same shape (e.g., beams of the same crack length-to-depth ratio, and the same span-to-depth ratio), and plotting the logarithm of nominal stress at failure, $\log \sigma_N$, versus $\log \lambda$ where $\lambda = d/d_a$, d = structure size (characteristic dimension), d_a = maximum aggregate size; see Figure 1.19. σ_N may be defined as P/bd (P = failure load, b = thickness), possibly times some constant characterizing the shape of the structure. According to all strength criteria (i.e., stress-based failure criteria), such as those used in elastic, plastic or elastoplastic design (as well as viscoelastic or viscoplastic design), σ_N is independent of d (see the examples of beam bending, shear or torsion in Figure 1.19). Thus, the

plot of $\log \sigma_N$ versus $\log \lambda$ is a horizontal line (Figure 1.19), and the only difference between elasticity and plasticity is the level at which this line is drawn.

For linear fracture mechanics, this plot is completely different. It is known that σ_N varies inversely as $\sqrt{d}$ for all linear fracture mechanics solutions, and so the slope of the plot of $\log \sigma_N$ vs. $\log \lambda$ is a straight line of slope $-1/2$; see Figure 1.19.

The finite element solutions for the crack band theory with gradual strain-softening represent a gradual transition from the horizontal line for the strength criterion to the downward sloping straight line for the linear fracture mechanics; see Figure 1.19. With the exception of very large and massive concrete structures, such as dams, most concrete structures fall into this transition range, in which neither the linear fracture mechanics nor the strength criterion is applicable. Failures in this transition range are obviously more difficult to analyze than those for the two limiting cases, and this is the main challenge in failure analysis of concrete structures.

In laboratory testing, the model structures have normally been made the smallest size possible with regard to the aggregate size (cross sections of 5 to 15 aggregate diameters). Thus, most of the laboratory tests of beams, plates, panels, slabs, shells, etc. carried out thus far around the world fall into the initial, nearly horizontal range of the diagram in Figure. 1.19. Obviously, such tests miss the size effect. Present methods of design embodied in the codes are all based on strength criteria, elastic or plastic, and therefore they give an incorrect, unsafe extrapolation to larger sizes characteristic of actual structures. This fact is certainly a matter of concern, and calls for reexamination of existing design procedures for those failures that are of brittle nature; e.g. the diagonal shear failure and torsion failure of beams, punching failure of slabs or shells, shear failure of deep beams and panels, cryptodome failure of top plate in a reactor vessel, etc. Recently it has become popular to apply to these failures plastic analysis, even though the failure is caused by concrete cracking. This trend is, in the writer's opinion, dubious and has led to successful comparisons with test data only because a wide range of sizes has not been tested in the laboratory.

The case of punching shear failure of slabs might be a good illustration. Plasticity analysis can be made to agree with the existing laboratory data only if the tensile strength is considered to be about $f'_c/200$, which is about 20-times less than the correct value of tensile strength. The proper conclusion from such an agreement should not be that plasticity of concrete works, but that it does *not* work, and that fracture mechanics, is, therefore, necessary. Obviously, the small value of nominal stress at failure must be due to the fact that the existing laboratory test data do not pertain to the initial horizontal portion of the diagram in Figure 1.19.

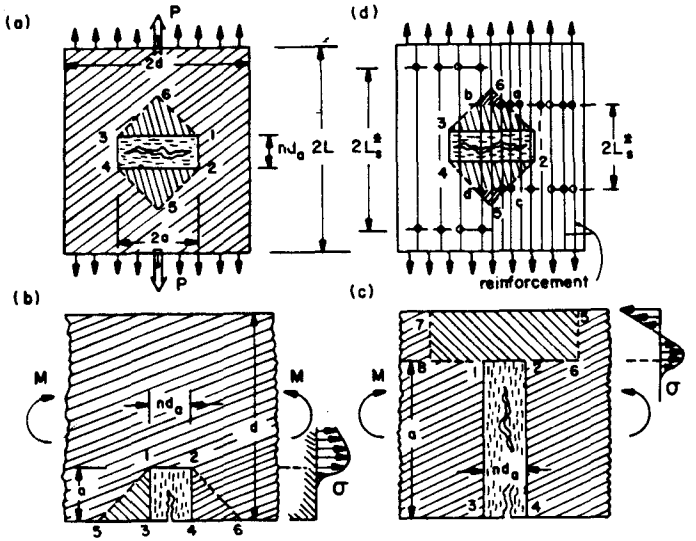

Fig. 1.20. Approximate analysis of energy release for various crack band situations.

Let us now try to derive a simple function to describe the typical transition curve in Figure 1.19. Consider first a center-cracked rectangular panel (Figure 1.20a) of thickness b, width $2d$, and a sufficiently large length $2L$. The panel is loaded by vertical normal stresses σ at top and bottom. The crack band is horizontal, symmetrically located, and has length $2a$ and width $w_c = nd_a$ ($n \approx 3$, d_a = aggregate size). Before cracking, the strain energy density in the panel is uniform and equals $\sigma^2/2E$. The formation of the crack band may be imagined, as an approximation, to relieve stress and strain energy from the area 1254361 in Figure. 1.20(a), in which the "stress diffusion" lines $\overline{25}$, $\overline{45}$, $\overline{16}$, $\overline{36}$ have a certain fixed slope k_1 (close to 1). The energy release is

$$W = W_1 + W_2, \quad W_1 = 2k_1 a^2 b \frac{\sigma^2}{2E}, \quad W_2 = 2nd_a ab \frac{\sigma^2}{2E}. \tag{1.45}$$

Cracking is imagined to occur at fixed top and bottom boundaries such that the contribution of the work of load σ on the boundaries is zero. The potential energy release rate of the panel then is $\partial W/\partial a$, and the energy criterion in Eq. 1.33 reads $\partial U/\partial a = 2G_f b - \partial W/\partial a = 2bG_f - 2(2k_1 a + nd_a)b\sigma^2/2E = 0$. After substituting $G_f = nd_a(1 - E/E_t)f_t'^2/2E$ (Eq. 1.15), p may be solved from this equation; this yields $\sigma = Af_t^*$ with

$$f_t^* = \frac{f_t'}{\sqrt{1 + C\lambda}}, \quad \lambda = \frac{d}{d_a} (\geqslant n \approx 3) \tag{1.46}$$

where

$$A = \sqrt{1 + \frac{E}{-E_t}}, \quad C = \frac{2k_1}{n}\frac{a}{d}. \tag{1.47}$$

A and C are constants when geometrically similar beams are considered. They are independent of the size. f_t^* may be called the *size-reduced strength*. It is a characteristic of the entire structure (and must be distinguished from f_{eq}, which is a characteristic of one finite element).

As a second example, consider a crack band of length a and width $w_c = nd_a$ ($n \approx 3$) in a rectangular unreinforced beam of thickness b and depth d, subjected to bending moment M. First consider that $a \ll d$ (short cracks). The formation of the crack band may be imagined, as an approximation, to relieve the strain energy from the area 1264351 in Figure 1.20b, where the "stress diffusion" lines $\overline{15}$ and $\overline{26}$ have a certain empirical slope k_1 close to 1. Before cracking, the strain energy density at the tensile face of beam is $\sigma_1^2/2E$ where $\sigma_1 = 6M/bd^2$, and the same value approximately applies over the whole region 1264351 if $a \ll d$. Thus, the total energy release is $W = W_1 + W_2$, $W_1 = k_1 a^2 \sigma_1^2/2E$, $W_2 = nd_a a\sigma_1^2/2E$. The potential energy release rate of the beam is $\partial W/\partial a$, and the energy criterion in Eq. 1.33 reads $\partial U/\partial a = bG_f - \partial W/\partial a = bG_f - b(2k_1 a + nd_a)(6M/bd^2)^2/2E = 0$. Substitute $G_f = nd_a(1 - E/E_t)f_t'^2/2E$ and evaluate the derivative $\partial W_1/\partial a$ of constant M. Then substitute $M = \sigma_N(d-a)^2/c_1$ (where c_1 = const. = 6 for elastic strength analysis, and $c_1 = 4$ for plastic strength analysis), and express σ_N from the resulting equation; this yields $\sigma_N = Af_t^*$ where f_t^* is given by Eq. 1.46 with

$$A = \frac{c_1}{6}\left(\frac{d}{d-a}\right)^2 \sqrt{1 + \frac{E}{-E_t}}, \quad C = \frac{2k_1}{n}\frac{a}{d}. \tag{1.48}$$

Again C and A are constants when geometrically similar beams are considered.

Thirdly, consider the same beam but $a - d \ll d$ (short ligament); Figure 1.20c. Let $U = bG_f a - (M\theta/2) - W_0$. Here, W_0 = strain energy of beam if no crack existed, which is independent of a, and θ = additional rotation caused by crack band. Since the force resultants of the bending stresses over the ligament are zero, these stresses should affect only a region of size $d - a$, according to St. Venant's principle. It may be imagined that the localized bending moment M transmitted through the ligament $d - a$ affects the region 1265781 in Figure 1.20c, with segments $\overline{18}$ and $\overline{26}$ equal to $k_0(d-a)$ where k_0 = empirical constant, close to 1. Approximately, $\theta = [2k_0(d-a) + nd_a]M/EI_1$ where $I_1 = b(d-a)^3/12$ = inertia moment of the ligament section. Substitute $G_f = (1 -$

$E/E_t)nd_a f_t'^2/2E$, and evaluate the derivative $\partial(M\theta/2)/\partial a$ at constant M. Inserting the result, as well as the relation $M = \sigma_N(d-a)^2/c_1$, into the condition $\partial U/\partial a = G_f - \partial(M\theta/2)/\partial a = 0$, and solving σ_N from the resulting relation, it follows that $\sigma_N = Af_t^*$ where f_t^* is again given by Eq. 1.46, in which

$$A = \frac{c_1}{6}\sqrt{1+\frac{E}{-E_t}}\,; \quad C = \frac{4k_0}{3}\frac{d-a}{d}. \tag{1.49}$$

Eq. (1.46) can be derived for various other situations, e.g., edge-cracked panels, crack band in infinite medium, double-cantilever specimen, etc. The solutions are approximate in the evaluation of energy release; however, this causes uncertainty only in the constants k_1 and k_0, but not in the form of Eq. 1.46.

It appears that Eq. 1.46 might be of general applicability. This can be verified by a dimensional analysis. Let the geometry of a given two-dimensional structure of thickness b be characterized by some set of dimensions d, l_1, l_2, $l_3,\ldots,l_n$, and consider all geometrically similar structures such that the ratios $\xi_i = l_i/d$ $(i = 1, 2,\ldots,n)$ are the same, so that size of the structure may be characterized by one characteristic dimension d. From the preceding examples, note that fracture needs to be described by two independent parameters – length a of the crack band, and width nd_a of the cracking front. It may be noted further (e.g., from Eq. 1.45) that the strain energy relieved by cracking may be expressed as $W = W_1 + W_2$ where W_1 is the strain energy relieved from the outside of the crack band, which is proportional to a^2 (e.g., strain energy contained in triangular areas 136 and 245 in Figure 1.20a), and W_2 is the strain energy relieved from within the area and_a occupied by the crack band. To nondimensionalize these variables, one may set $a^2 = \alpha_1^2 d^2$ and $and_a = \alpha_2 d^2$ where α_1 and α_2 are the nondimensional parameters

$$\alpha_1 = \frac{a}{d}, \quad \alpha_2 = \frac{and_a}{d^2} \tag{1.50}$$

representing the nondimensional length and the nondimensional area of the crack band. The energy release by crack band formation may now be generally expressed as

$$W = f(\xi_i, \alpha_1, \alpha_2)\left(\frac{P}{bd}\right)^2 \frac{d^2 b}{2E} \tag{1.51}$$

where P is the given applied force or loading parameter, and function f depends on the shape of the structure and of the crack band, but is independent of size d. The condition of crack band propagation is

$\partial W/\partial a = G_f b$, and differentiating equation (1.51) at constant ξ_i (similar structures) leads to $(f_1/d + f_2 nd_a/d^2)P^2/2bE = G_f b$ in which the notations $f_1 = \partial f/\partial\alpha_1$ and $f_2 = \partial f/\partial\alpha_2$ have been adopted. Setting $G_f = nd_a(E^{-1} - E_t^{-1})f_t'^2/2$ (Eq. 1.15), $P = \sigma_N bd$, and $d = \lambda d_a$, yield the relation $\sigma_N = Af_t^*$, where f_t^* is again given by Eq. 1.46 and

$$\lambda = \frac{d}{d_a}, \quad A = \sqrt{\frac{1}{f_2}\left(1+\frac{E}{-E_t}\right)}, \quad C = \frac{f_1}{nf_2} \tag{1.52}$$

where A and C are constant as the structure size is varied.

To sum up, the essential property which has led to Eq. 1.46 is the dependence of energy release on both the crack band area and the crack band length. If the energy release depended only on the crack band length ($f_2 = 0$), one would get $\sigma_N = (2G_f E/f_1)^{1/2}/\sqrt{d}$, which is the size dependence of linear fracture mechanics. If it depended only on the crack band area ($f_1 = 0$), one would get the size dependence of plasticity ($\sigma_N = \text{const.}$).

It may be concluded that Eq. 1.46 is of general applicability, as long as the two nondimensional parameters α_1 and α_2 (and no further parameters) are needed, and suffice, to characterize fracture.

For a small size relative to the size of aggregate, $\lambda \to 0$, $f_t^* \to f_t'$, and $\sigma_N = Af_t'$. For a very large size, $\lambda \to \infty$, the relation

$$f_t^* \simeq f_t'/\sqrt{C\lambda} \quad (\lambda \to \infty). \tag{1.53}$$

holds. Thus, Eq. 1.46 asymptotically approaches the size effect of linear fracture mechanics. Fracture-insensitive behavior is also a special case of Eq. 1.46; $C \simeq 0$.

Eq. 1.46 may be checked against the test data of Walsh [56] who tested geometrically similar three-point bent specimens of various beam depths d. His test results for six different concretes are plotted in Fig. 1.21 as Y vs. λ where $Y = (f_t'/\sigma_N)^2$. In such plots Eq. 1.46 is a straight line of slope C/A^2 and Y-intercept $1/A^2$. The regression lines corresponding to Eq. 1.46 are plotted in Fig. 1.21. It is seen that they agree reasonably well with the data. For strength theory, the regression lines would have to be horizontal, which is certainly not the case, and for linear fracture mechanics, the regression lines would have to pass through the origin, which is also evidently not the case.

Reinforcement located near the fracture front may have influence, too. To examine it, consider the same center-cracked rectangular panel as before (Figure 1.20d), reinforced by vertical steel bars which are spaced uniformly and so closely that a smeared modeling is possible. The panel is loaded on top and bottom by uniform normal stress σ. Before cracking,

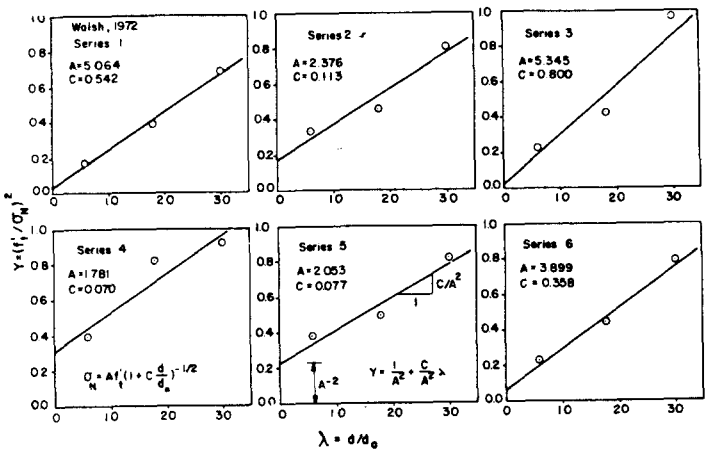

Fig. 1.21. Regression analysis of Walsh's (1972) fracture data.

the stress in concrete is $\sigma_c = \kappa_c \sigma$ where $\kappa_c = E_c/[E_c(1-p)+E_s p]$; p = steel ratio; E_c, E_s = Young's elastic moduli of concrete and steel. When cracks form, the steel bars slip near the cracks, as discussed before (Eq. 1.27). For the same reasons as before, the frictional slip may be replaced over the actual bond-slip length $2L_s$ by free (frictionless) slip over a modified, free bond-slip length $2L_s^*$ (Eq. 1.27), and assume perfect bond beyond this length (Figure 1.20d). Consider that $L_s^* = L_s/2$.

Formation on fracture relieves the stress in concrete from the region 1254361 in Figure 1.20(d), in which the "stress-diffusion" lines 16, 25, 36, 35 have a certain constant slope k_1. The stress relief is, however, complete only if this region is entirely within the free bond slip length $2L_s^*$; Figure 1.20(d). If crack band length a is so large that this region reaches beyond the free bond slip length, then the tensions in the steel bars introduce tensile stress into concrete within the triangular regions 5ab and 6cd in Figure 1.20(d). The value of stress in steel within the slip region, σ_{sL}, is less than (but probably close to) the stress that the steel carried before cracking, i.e., $\sigma_{sL} < \kappa_s \sigma$ where $\kappa_s = L_s/[E_c(1-p)+E_s p]$. Thus, the stress resultant per unit area, applied on these triangular regions is $< p\kappa_s\sigma$, which produces in concrete within the triangular regions the stress σ_c' such that $\sigma_c' < \kappa_c(p\kappa_s\sigma)$. This gives

$$\sigma_c' = c_t p \kappa_s \kappa_c \sigma \tag{1.54}$$

where c_t is a coefficient less than 1 but probably close to 1. The strain energy release from the panel of thickness b may now be expressed as

$$W = \left[(k_1 a^2 + and_a)\frac{(\kappa_c\sigma)^2}{2E_c} - \frac{H_a}{k_1}(k_1 a - 2L_s^*)^2 \frac{\sigma_c'^2}{2E_c} \right] b \tag{1.55}$$

where $H_a = 1$ if $k_1 a > 2L_s^*$, and $H_a = 0$ if $k_1 a \leqslant 2L_s^*$.

In the energy balance, the energy consumed by bond slip should be included. The maximum slip of bars is at the crack axis and is roughly $(f_t'/E_c)L_s$. At the ends of length $2L_s$ the slip is zero, and so the mean slip is about $f_t' L_s/2E_c$. The bond stress is roughly U_b' per unit length of bar, as determined from pull-out tests. The number of steel bars per unit cross section of panel is p/A_b where A_b = cross-section area of one bar, and $L_s \simeq 2L_s^*$. So the work of bond stresses over length L_s per unit advance of the crack band is

$$W_b' = \frac{p}{A_b}\frac{f_t' L_s^*}{E_c} U_b' b \tag{1.56}$$

where b = panel thickness. In Eqs. 1.56 and 1.55, further substitution leads to $L_s^* = L_s/2 = c_L A_b/2U_b'$ where $c_L = \sigma_s - \sigma_s'$ as defined in Eq. 1.26.

The energy balance condition for crack band advance may now be written as $bG_f + W_b' = \partial W/\partial a$, where $G_f = nd_a(1 - E_c/E_t)f_t'^2/2E_c$. Differentiating Eq. 1.55 and substituting, we obtain $\sigma_c = A' f_t'$ where $\sigma_c = \kappa_c \sigma$ and

$$f_t^* = \frac{f_t'}{\sqrt{1 + C'\lambda}}, \quad \lambda = \frac{d}{d_a} (\geqslant n = 3) \tag{1.57}$$

$$A' = \sqrt{A_1/B_1}, \quad C' = C_1/B_1, \quad A_1 = 1 - \frac{E_c}{-E_t} + \frac{pc_L}{nd_a f_t'},$$

$$B_1 = 1 + H_a \frac{2c_L}{nd_a}\frac{A_b}{U_b'}(c_t p \kappa_s)^2, \quad C_1 = \frac{2k_1}{n}\left[1 - 2H_a(c_t p \kappa_s)^2\right]\frac{a}{d}. \tag{1.58}$$

Consider now geometrically similar panels (same a/d), with same steel ratio p, and same bars, i.e., same A_b (also, $c_L \simeq$ constant). Then, Eq. 1.57 indicates the same type of dependence on structure size, λ, as Eq. 1.46, except that coefficient C' is larger than C. This shifts the asymptotic declining straight line in the plot of $\log f_t^*$ versus $\log \lambda$ to the right; see Figure 1.22a. If the steel bar size is increased with the structure size, the size effect becomes somewhat more pronounced since f_t^* decreases as A_b increases.

The size effect in reinforced structures is seen to be less pronounced for smaller sizes of the structure, but for large enough structure sizes the size effect becomes just as significant as for unreinforced structures since the asymptotic slope remains $-1/2$. This is, however, true only if the reinforcement remains elastic. For a long enough crack band, the opening in the center of its length becomes sufficiently large to cause the steel to

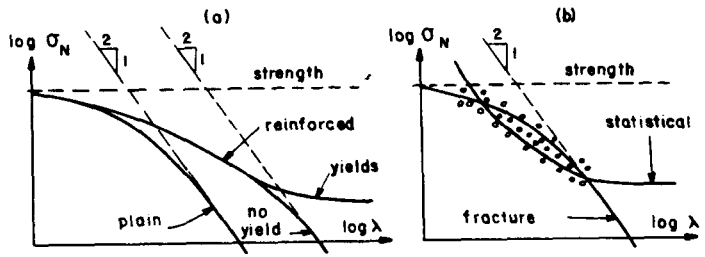

Fig. 1.22. (a) Structural size effects in reinforced concrete structures, and (b) statistical size effect of strength in structures.

yield, and that will completely alter the size effect. If the steel bars are yielding, the strains are so large that all resistance of concrete is lost, and the load is resisted by reinforcement alone. In that case, the value of σ becomes size independent. Therefore, in reinforced structures, the plot of $\log f_t^*$ versus $\log \lambda$ eventually stops decreasing and approaches a horizontal line. However, this limiting plastic value might be too low for practical purposes.

Finally, it is instructive to compare the results to the well-known statistical size effect. Concrete is heterogeneous, and the strength varies randomly throughout a concrete structure. This variation is independent of structure size. The stress gradient, on the other hand, normally varies inversely with the structure size, and the region of peak stress becomes larger in a larger structure. Therefore, the chance of encountering low strength in the peak stress region is higher in a larger structure, and so the apparent strength must decline with structure size. However, the decline stops when the peak stress region becomes much larger than the low strength regions. Therefore, all theories of the statistical size effect produce a plot of $\log \sigma_N$ versus $\log \lambda$ which tends to a horizontal asymptote. This is completely different from the fracture-mechanics size effect (Fig. 1.22b), except when yielding of reinforcement makes the response plastic.

It seems that many observed size effects in concrete structures should have been explained by fracture mechanics rather than statistical variation of strength. The dependence of the apparent bending strength on the depth of plain concrete beams is a blatant example. If the test data do not cover a very large range of λ, both theories seem to work. This may be misleading for extrapolations.

1.5 Applications and practical analysis

Diagonal shear failure of beams. Eq. 1.46 may be applied to introduce the size effect into various existing strength-based formulas for failure of concrete structures. For example, the ACI or CEB-FIP code formulas for the diagonal shear failure of beams with longitudinal reinforcement but without web reinforcement involve no size effect. In an on-going study at Northwestern University, J.K. Kim and Bažant analyzed failure data for over 300 beams which have been tested in various laboratories throughout the world and were reported in the literature. After determining and optimizing an approximate semiempirical formula (similar to that in ACI Code) for the nominal shear stress σ_N at failure as a function of the shear span and of the longitudinal reinforcement ratio, the dependence of σ_N on the size parameter $\lambda = d/d_a$ has been analyzed statistically, using Eq. 1.46 for regression analysis of existing data of diagonal shear failure of beams without web reinforcement, notably the data by Kani, Leonhardt, Bhal, Walraven, Taylor, Rüsch and Swamy [77–83].

Although most existing test data involve very small beam depths, there exist a few data which involve beams of various depths. One result of the ongoing study is the diagram in Figure 1.23 [84]. It is seen that the data points are not well approximated by a horizontal line, which would mean the absence of fracture mechanics type size effect; the data points agree well with the function in Eq. 1.46, plotted as the solid curve. This is better illustrated by statistical regression analysis in Figure 1.24, in which $Y = \sigma_N^{-2}$ is plotted versus λ. Function $f_t^*(\lambda)$ appears in this plot as a straight line of the equation $Y = \bar{a} + \bar{b}\lambda$ where $\bar{a} = (Af_t')^{-2}$, $\bar{b} = C\bar{a}$. Absence of the size effect would mean a horizontal regression line in Figure 1.24, and this is clearly contradicted by the data. Despite a large scatter, the data points exhibit an upward straight-line trend. Thus, the existing data clearly confirm a significant size effect and justify Eq. 1.46.

Based on this analysis, it seems that most of the code formulas for predicting the strength of structural members would be improved by replacing in them f_t' with f_t^*. A more detailed investigation is needed, however, and coefficient C needs to be determined for each case.

Reinhardt [85,86] has recently studied some of these data, and found that they reasonably agree with a linear fracture mechanics size effect ($C\lambda \gg 1$). This type of size effect would correspond in Figure 1.24 to a straight regression line passing through the origin, and in Figure 1.23, this would correspond to an inclined straight regression line rather than a curvilinear regression. It is seen from this figure that such trends are not confirmed when all available test data are considered. The size effect of linear fracture mechanics would be too strong. Clearly, the bulk of existing test results for diagonal shear failure indicates the need for a nonlinear fracture theory.

As an example of finite element fracture analysis, the results obtained by Cedolin and Bažant [60] may be presented for the shear failure of the panel sketched in Figure 1.25, which is reinforced only by horizontal steel bars concentrated near the bottom of the panel, and is loaded by a

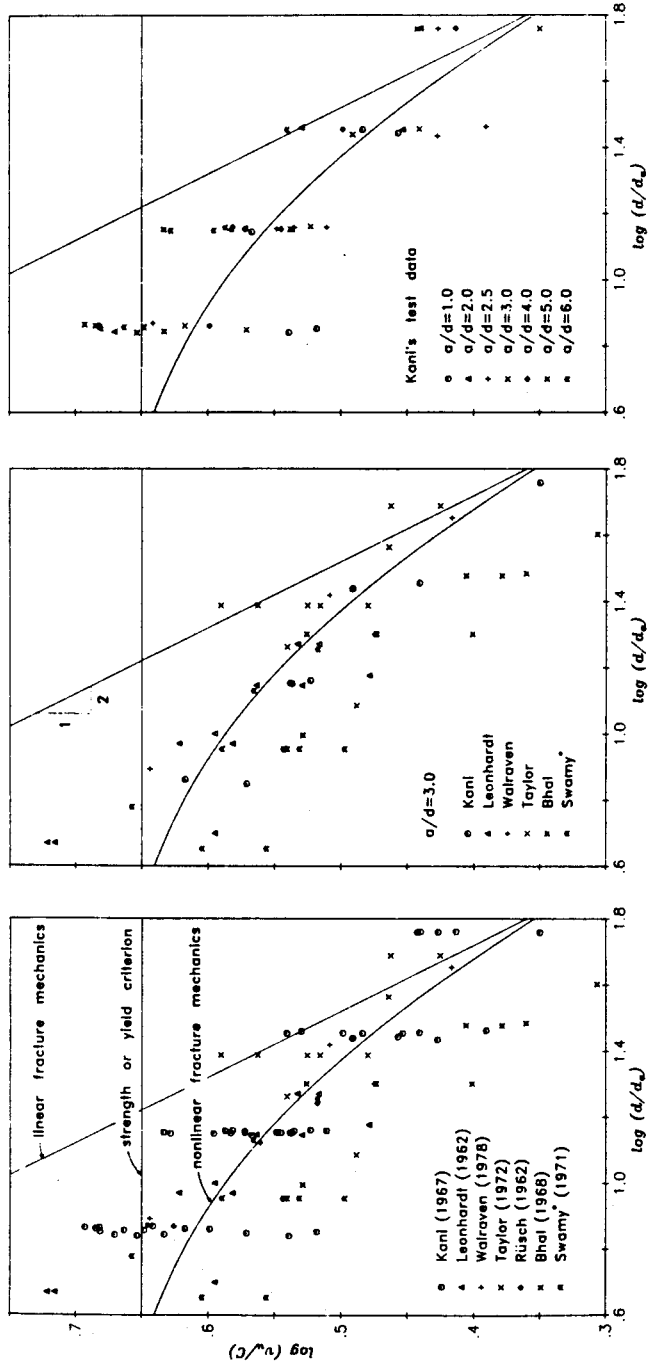

Fig. 1.23. Analysis of test data from various laboratories on diagonal shear failure of beams without web reinforcement (after Bažant and Kim, 1983).

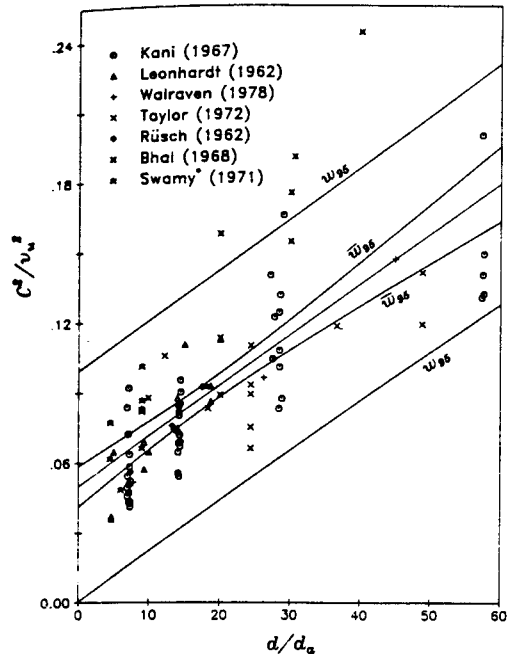

Fig. 1.24. Same data as in fig. 23a plotted in linear regression.

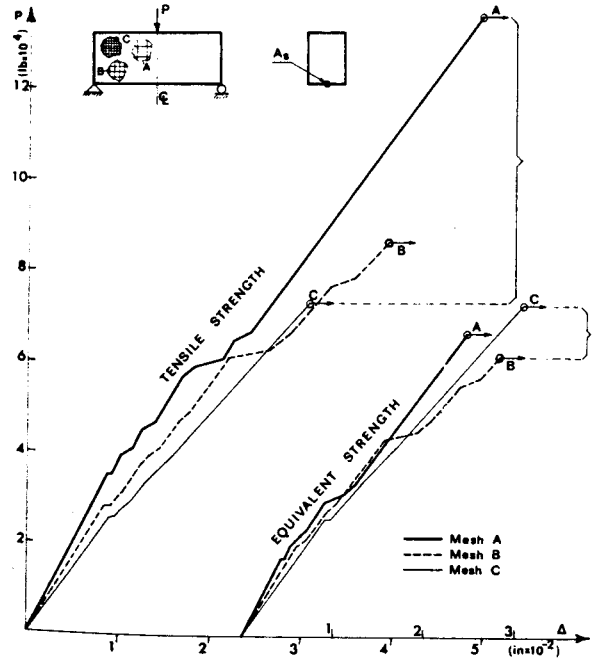

Fig. 1.25. Finite element analysis of shear failure of deep beams (after Bažant and Cedolin, 1982, 1983).

vertical force at midspan. The crack band path is not known is advance but is to be found. Among the elements sharing a side with the crack front element, the crack band was assumed to spread into that element in which the principal tensile stress is the largest. The analysis was carried out both for the actual tensile strength f_t' and for the equivalent strength f_{eq}'. The displacement at the loading point was introduced in small increments. At each load step, Newton-Raphson iterative procedure was used to redistribute the unbalanced nodal forces due to cracking until a stable crack band configuration was reached. Linear elastic behavior was assumed for concrete in compression.

The analysis was carried out for three different meshes (A, B and C in Figure 1.25), in which the finite element sizes are in the ratio 4 : 2 : 1. The load-deflection curves obtained for these three meshes are plotted in Figure 1.25. Even though this problem is less sensitive to the value of tensile strength than others, the deflection curves are more consistent for the equivalent strength criterion. The element size effect is largest for the value of the load at which the cracking zone reaches a certain fixed distance from the top. This distance was fixed as one-half of the size of the element in the crudest mesh (A), which then equals a distance of one element for mesh B, and of two elements for mesh C. The loads for which the cracking zone reaches this distance from the top are indicated in Figure 1.25 by horizontal arrows. For the equivalent strength criterion, they differ from each other much less than they do for the fixed tensile strength criterion. Furthermore, it was found (see Closure of [59]) that the crack patterns for meshes A, B and C are rather different and, in particular, the cracking zone for the finest mesh is not diffuse but localizes into narrow, separate crack bands of single element width at the front. This behavior is obtained, however, only when the loading steps are taken to be so small that no more than one element cracks during the first iteration of each loading step.

Deflections of cracking beams. As another application, consider deflections of unprestressed reinforced concrete beams. Their deflections are

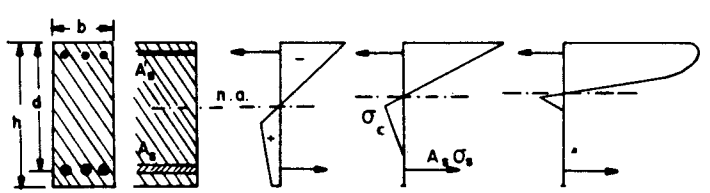

Fig. 1.26. (a) Stress-distribution in cross sections of beams with tensile-strain softening: (b) calculated beam deflections (Bažant and Oh, 1983) and their comparison with tests by Gerstle et al. (1964, 1965), Burns and Siess (1966), and Hollington (1970).

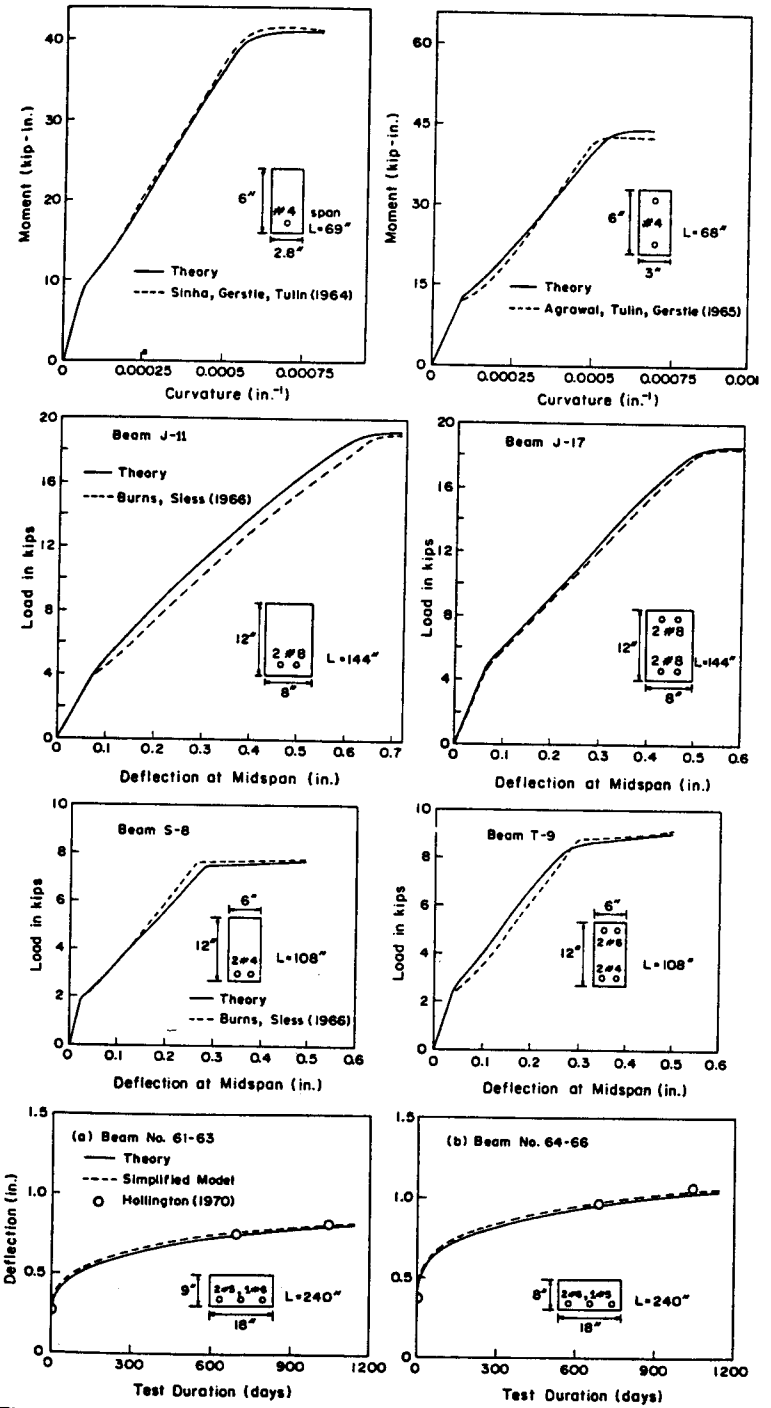

Fig. 1.26 (b).

considerably less than those calculated under the assumption of no cracking; obviously the beams crack, even under service loads. On the other hand, if one assumes a no-tension material (which is the accepted approach to strength analysis, justified by the fact that strength is determined by the weakest cross section rather than the overall mean behavior), then the calculated deflections are much larger than the measured ones. This phenomenon, which is usually referred to as "tension-stiffening," is due to progressive microcracking of concrete in the tensile zone of beam, and so it should be possible to obtain correct deflections using our present bilinear stress-strain relation with strain softening (Figure 1.26).

This was done in [87]. The value of E_t was predicted from Eq. 1.21. On the compression side, Saenz' expression for strains due to uniaxial compression was assumed. The uniaxial stress-strain diagram of steel was considered as elastic–perfectly plastic, and the average strain of steel was assumed to be equal to the average strain of concrete at the same level. Based on these assumptions, the typical distributions of normal stress in concrete were as shown in Figure 1.26a.

As far as the cracking front is concerned, it is assumed here that the cracking does not localize and the strain everywhere follows the kinematic constraint expressed by the usual assumption that the cross sections remain plane and normal. The localization of cracking into certain cross sections is assumed to be prevented by tensile reinforcement and by the constraint provided to the cracking front by the compression zone (for deep beams, or for shear failures, the absence of localization cannot be assumed, of course).

Calculations based on the foregoing assumptions were compared [87] with the measurements of beam curvatures and deflections reported in the literature [89–92]. No fitting of data was attempted, i.e., no material parameter was adjusted to improve the fit. The comparisons are shown in Figure 1.26. The agreement is good, much better than the corresponding case when the tensile resistance of concrete is neglected. It was also shown [87] that the calculations give essentially the same results as the well-known Branson's empirical formula [76] within its range of validity (service loads). This success indirectly lends further support to our stress-strain relation for fracture.

The foregoing analysis of deflections, which applies to short time loading, was further extended to long-time loading. The effective modulus method was used to take concrete creep into account. The creep properties were predicted on the basis of double power law [93]. Since this creep law does not apply for the tensile strain-softening range, and since creep in this range may be expected to be larger, the tensile creep deformations were multiplied by an empirical coefficient c_ϕ the value of which was determined so as to get the best fit of measured long-time

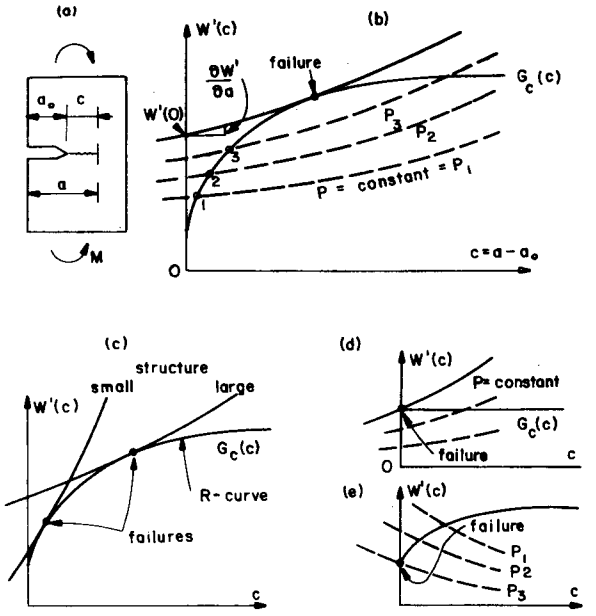

Fig. 1.27. Determination of crack extension from R-curves.

deflections ($c_\phi \simeq 3$). No other material parameter was adjusted. The results of calculations were compared [87] with the long-time deflections of beams tested by Hollington [94]; the agreement was again good (Figure 1.26). Furthermore, the long-time deflections have been calculated for typical singly and doubly reinforced beams, and were compared with an ACI empirical formula. The agreement was good again [87], and in particular, the strong effect of compression reinforcement on creep deflections of cracked beams, as known from tests, was predicted correctly.

Application of R-curves. For practical nonlinear fracture analysis, it is helpful to use the approach of resistance curves, or R-curves [95,41]. R-curve is the curve of effective or apparent fracture energy G_c as a function of the extension a of a crack from a notch (Figures 1.27a and 1.27b). For materials which deviate from linear fracture mechanics, it is found that the amount of energy per unit crack extension, which flows into the fracture process zone, increases as the crack extends until it stabilizes at some constant limiting value, G_f, unless some boundaries or loads are near the fracture front.

As shown in the foregoing (Figure 1.6), in the crack band approach, the R-curve can be predicted from the tensile strain-softening stress–strain relation. The predictions are different for different body geometries, or

different loads and loading paths. It appears, however, that the shape of the R-curve (Figure 1.27) is nearly the same for most situations. Even though this can be exactly true only for infinitely short extensions of a crack from a notch, the R-curve can be assumed, for most purposes, to be approximately a fixed material property, independent of body geometry and the type of loading [41], as proposed in 1961 by Krafft et al. [95]. This assumption was proven to be rather successful for ductile fracture of metals [41]. Following the work in [96], a simple form of fracture analysis of concrete using the R-curve approach will be outlined.

Consider that the effective fracture energy, G_c, depends on c where $c = a - a_0$, a = length of crack with the notch, a_0 = length of the notch; $G_c = G_c(c)$. The energy that must be supplied to the structure is $U = \int G_c da - W(a)$ (if the thickness of the body is $b = 1$), where W = release of strain energy from the body, and G_c effective fracture energy at distance a from the notch. An equilibrium state of crack occurs when no energy needs to be supplied to change a by δa, i.e., when $\delta U = 0$ or $\delta U = (G_c - W')\delta a = 0$ or

$$W'(a) = G_c(c) \tag{1.59}$$

where $W'(a) = \partial W/\partial a$ = energy release rate, and $c = a - a_0$. The equilibrium crack state is stable if the second variation $\delta^2 U$ is positive, i.e., $\delta^2 U = \frac{1}{2}(\partial G_c/\partial a - \partial^2 W/\partial a^2)\delta a^2 > 0$ or $\partial G_c(c)/\partial c > \partial W'(a)/\partial a$. The limit of stability, i.e., failure, occurs if

$$\frac{\partial W'(a)}{\partial a} = \frac{\partial G_c(c)}{\partial c}. \tag{1.60}$$

For most structural situations, the strain energy release rate increases as the crack grows, i.e. $W'(a) > 0$. By elastic structural analysis, the curve $W_1'(a)$ corresponding to a unit load can be calculated. Then, for any load P, $W'(a) = P^2 W_1'(a)$. In Figure 1.27, we sketch the curves $W'(a)$ for a set of increasing P-values, P_1, P_2, P_3,... According to Eq. 1.59, the equilibrium states of crack extension for various loads are given by the intersections of these curves with the curve $G_c(c)$. These states are, according to Eq. 1.60, stable if the slope of the $G_c(c)$-curve is larger than the slope of the $W'(a)$-curve (see points 1, 2, 3 in Figure 1.27b). As the crack grows, the difference between the slopes $\partial G_c/\partial a$ and $\partial W'/\partial a$ gradually diminishes until the slopes become equal at the failure point (Figure 1.27); this point represents a critical state (or failure state) according to Eq. 1.60. Beyond this point, the crack extension is unstable. In the case that $W' < 0$ for all a, Eq. 1.60 is always satisfied. The crack is then stable for all a (Figure 1.27e).

In the case that G_c = constant = G_f, Eq. 60 reads $0 > \partial W'/\partial a$. This

condition can never be satisfied if W' increases with a (Figure 1.27d). Thus, the fact that a stable crack growth from a notch exists implies that G_c cannot be constant but must increase.

For an approximate estimate of the values of $W'(a)$, one may use linear fracture mechanics provided that crack length a is interpreted as the equivalent length that gives the same remote stress field as the crack band. It might be difficult to actually determine this equivalent crack length for a given situation, but for practical purposes this is not necessary since the actual crack length at failure need not be known.

In a recent study [96], R-curves were used to analyze fracture test data from the literature [44,45,47–49,51,53,56] obtained with bent specimens or center-cracked specimens (the same data as used in Figures 1.5 and 1.6). The R-curve was assumed in the form

$$G_c(c) = G_f\left(1 - \beta_c e^{-c/c_1 d_a}\right) \qquad (c = a - a_0) \tag{1.61}$$

where G_f, β_c and c_1 are constants to be found by fitting test data, and d_a = maximum aggregate size. A more general expression, namely $G_c = G_f[1 - \beta_f \exp(-c/c_1 d_a)^q]^r$ was also studied but $q = r = 1$ was found to be about optimum. The energy release rates, $W_1'(a)$, for unit load ($P = 1$), were calculated as $W_1'(a) = K_1^2/E$ from the existing analytical expressions for the stress intensity factor K_1, as listed for these specimens in Tada's manual [97]. The computational algorithm was as follows:

(1) Set the values of G_f, β_f, c_1, Δa ($= 0.01\ a_0$), and set $a = a_0$.
(2) Increment a, replacing a with $a + \Delta a$. Set $c = a - a_0$.
(3) For each a, calculate $W_1'(a)$, and since $W' = W_1' P^2$ determine the load corresponding to a as $P = [G_c(c)/W_1'(a)]^{1/2}$. If this value of P is larger than the previous P-value, return to 2.
(4) Now $\partial G_c/\partial c < \partial W'/\partial a$, i.e. the specimen fails. Set $P_{max} = P$. (One could interpolate for the exact a at which $\partial G_c/\partial c = \partial W'/\partial a$ but this is not necessary if Δa is as small as $0.01\ a_0$.) Evaluate deviation of given test data from the theory as $\Delta P_{error} = P_m - P_{max}$ where P_m = measured value of maximum load.
(5) Repeat steps (1) to (4) for another case of the same test series (e.g., another notch depth a_0 or another beam depth H), and accumulate the sum $\Phi = \Sigma(\Delta P_{error}/P_0)^2$ where P_0 = prediction of failure load according to the bending strength theory (based on the ligament section).

The foregoing algorithm (computer subroutine) is then used with a library optimization algorithm, such as Marquardt-Levenberg's, to vary the values of G_f, β_f and c, until those values which give min Φ are determined. In this manner, it was found [96] that the values $\beta_f = 0.72$ and $c_1 = 1.85$ are nearly optimum for all concretes tested, while the values of G_f vary substantially from concrete [96]. Note that the optimum

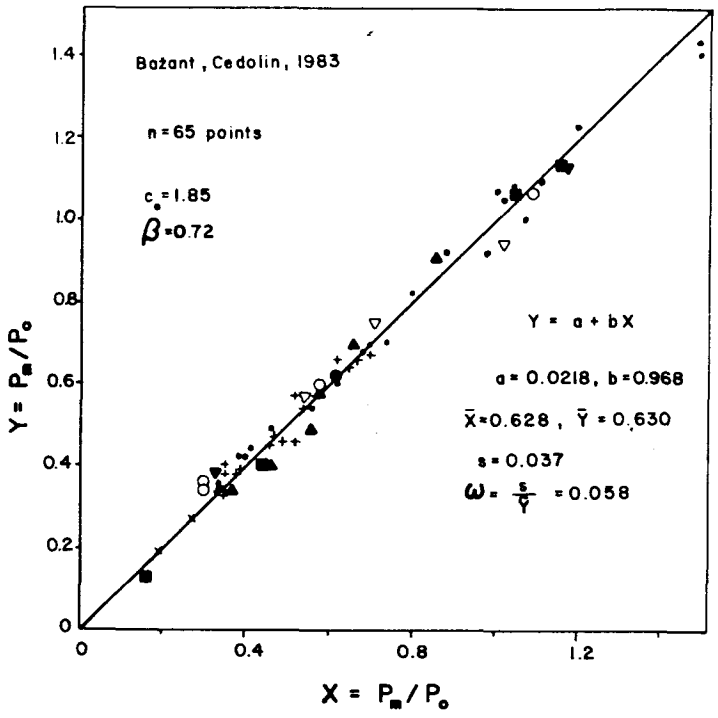

Fig. 1.28. Statistical comparison of measured failure loads with R-curve calculations for various test data from literature (after Bažant and Cedolin, 1983).

G_f values for the R-curve approach are not the same as those for the finite element crack band approach.

To get an idea of the error magnitude, Figure 1.28 reproduces from [96] a plot of Y versus X where $Y = P_t/P_0$, $X = P_m/P_0$, P_m = measured P_{max}, $P_t = P_{max}$ obtained from the R-curve analysis for the optimum material parameters determined as just described. This figure includes the data from [44,45,47–49,51,53,56]. By regression analysis, the standard deviation at the data centroid is found to be 0.037, and the coefficient of variation 5.8%. This is quite satisfactory and proves the applicability of the R-curve approach. Note that the error for the crack band finite element model (Figure 1.9) is about the same.

The R-curve analysis may be simplified if the energy release rate $W'(a)$ may be approximated by a straight line within the R-curve region, and if the R-curve is described by a parabola

$$G_c(c) = G_f\left[1 - \beta_f\left(\frac{c}{c_1 d_a} - 1\right)^2\right] \qquad (0 \leqslant c \leqslant c_1 d_a). \tag{1.62}$$

Eqs. 1.59 and 1.60 then become $P^2 W_1'' = \partial G_c/\partial c$ and $P^2(W_1' + W_1'' c) =$

$G_c(c)$. Substituting Eq. 1.62, we may reduce these two equations to a quadratic equation for c:

$$\left(\frac{c}{c_1 d_a} - 1\right)^2 - \frac{2}{c_1 d_a}\left(\frac{W_1'}{W_1''} + c\right)\left(\frac{c}{c_1 d_a} - 1\right) = \frac{1}{\beta_f}. \tag{1.63}$$

Solving c from this equation, $G_c(c)$ may be evaluated and the failure load may be calculated as $P_{max} = G_c(c)/(W_1' + W_1'' c)$. For this solution, it suffices to determine from linear fracture analysis the values of W_1' and W_1'' at $a = a_0$ (and for unit load).

If $W'_1(a)$ is approximated by a parabola, an algebraic equation of fourth degree must be solved to determine c.

In another recent study [98], the R-curve approach has been used under the assumption that the nonlinear zone is negligibly small compared to specimen dimensions, crack length and ligament size. In this case, the stress field near the nonlinear zone may be solved considering that the crack tip is surrounded by an infinite elastic medium.

1.6 Crack development

Crack spacing at uniform strain. Crack spacing has a major influence on the crack width, which in turn, affects structural performance, including shear transfer, tensile stiffness, energy absorption capability, ductility and corrosion resistance. Recently, fracture mechanics energy analysis has been used to derive formulas for the spacing of parallel cracks produced by tension [88]. Only some simple solutions will be indicated here.

Consider one steel bar of diameter D embedded in the axis of concrete cylinder of diameter b (Figure 1.29). If the cross-section area of concrete per bar is replaced by a circular area, this situation may be used also as an approximate model for concrete reinforced by a regular array of parallel bars subjected to a uniform uniaxial tension. Consider equidistant cracks normal to the bar, denote their initial spacing as 2s (Figure 1.99), and try to determine the formation of further cracks that halve the spacing to s. In the light of the preceding theory, there are now two criteria to consider:

(1) The strength criterion decides whether the strain can exceed the strain value ε_p for peak stress, f_t'. If there is no bond slip, the strength criterion simply is

$$\varepsilon_s \geqslant f_t'/E_c \qquad \text{(strength, no slip)}. \tag{1.64}$$

If there is bond slip, and the ultimate bond force U_b' per unit length of

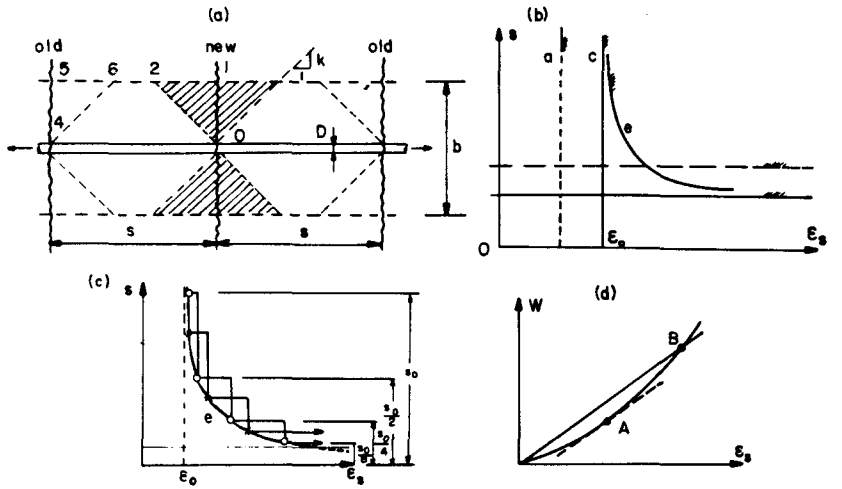

Fig. 1.29. (a) Parallel cracks normal to a reinforced bar, and (b) limits on crack spacing and strain at cracking. (a-strength, no slip; b-strength, slip; c-energy, no slip; d-energy, slip; e-curve for more accurate solution) (after Bažant and Oh, 1983).

bar is constant and is given, there results the equilibrium condition $U_b' L_b = A_c f_t'$ where $A_c = (b^2 - D^2)\pi/4 =$ area of concrete, and $L_b =$ length over which there is slip. Since $L_b \leqslant s$, it follows that

$$s \geqslant \frac{\pi f_t'(b^2 - D^2)}{4U_b'} \qquad \text{(strength, slip)}. \tag{1.65}$$

(2) For the energy criterion, the release of strain energy caused by cracking may be estimated by imagining that the formation of the crack relieves the strain energy from the shaded triangular region in Figure 1.29, limited by "stress-diffusion" lines of empirical slope k, close to 1. Assuming that $2s \geqslant k(D - b)$, these triangular areas do not overlap, and the volume per crack obtained by rotating these areas about the bar axis is $V_1 \simeq \pi b^3/12k$, in which D^3 is neglected in comparison with b^3. The strain energy density before cracking is $\sigma_1^2 V_1/2E_c$ where $\sigma_1 = E_c \varepsilon_s$ if there is no bond slip. The strain energy release due to formation of the new cracks between the original ones is $\Delta W \simeq V_1 \sigma_1^2/2E_c$. For the cracks to form, this must equal or exceed the energy consumed by the crack formation, which is $G_f \pi b^2/4$, D^2 being again neglected compared to b^2. This yields the condition

$$\varepsilon_s \geqslant \left(\frac{6kG_f}{E_c b}\right)^{1/2} \qquad \text{(energy, no slip)}. \tag{1.66}$$

A similar formula may be derived for the case $2s < k(D-b)$.

If there is bond slip, then $\sigma_1 = U_b' s/(\pi b^2/4)$. Using this to express ΔW_1, as before, the following condition is obtained:

$$s \geqslant \left(\frac{3\pi^2 k E_c G_f b^3}{8U_b'}\right)^{1/2} \qquad \text{(energy, slip)}. \tag{1.67}$$

Eqs. 1.64 to 1.67 give boundaries of halving of crack spacing in the plot of spacing s versus steel strain ε_s; see Figure 1.29. In [88], more involved formulas based on more realistic assumptions are given; for them, the boundaries in Figure 1.29 become smoothly curved giving a one-to-one correspondence between ε_s and s (curve e in Figure 1.29b and 1.29c). Only with such a formulation it is possible to describe successive halvings of crack spacing at increasing strain [88]; Figure 1.29c.

In Eqs. 1.66 and 1.67, the energy criterion is used in an unorthodox manner. Instead of using the energy balance condition for small increments (or rates), the energy balance condition was used for the transition from no crack to a complete crack. This always indicates the cracking to occur somewhat later in the loading process than does the incremental energy condition (at point B instead of point A in Figure 1.27d). It seems that when analyzing cracks that are not much longer than the aggregate size, it makes no sense to consider infinitesimal crack length increments since a continuum model makes no sense on that scale.

As the strain is increased, some mutually very remote cracks form first, and all subsequent crack formation may be assumed to evolve by means of halving of the spacing, to which Eqs. 1.64 to 1.67 apply. The manner of crack formation differs depending on whether the strength criterion or the energy criterion is fulfilled first. The strength criterion (Eq. 1.64 or 1.65) indicates merely that ε_s exceeds the strain ε_p for peak stress. Therefore, if only the strength criterion is fulfilled, it means that microcracking begins but complete cracks do not necessarily form. For that to happen, the energy criterion (Eq. 1.66 or 1.67) must become also satisfied. In this case, the crack formation is obviously gradual, static.

If the energy criterion (Eq. 1.66 or 1.67) is satisfied first, cracks cannot begin to form, and so they cannot form at all. Then, if the strength criterion (Eq. 1.64 or 1.65) becomes satisfied later, there is an excess energy available for crack formation. The excess energy gets converted into kinetic energy, and so the cracks form suddenly, dynamically (emitting sound), in the manner of snap-through instability.

The theory just briefly outlined permitted achieving satisfactory comparisons with the measurements of crack spacing s and crack width w. As an example, Figure 1.30, taken from [88], shows a comparison with Chi and Kirstein's data [100], in which the crack width is estimated as

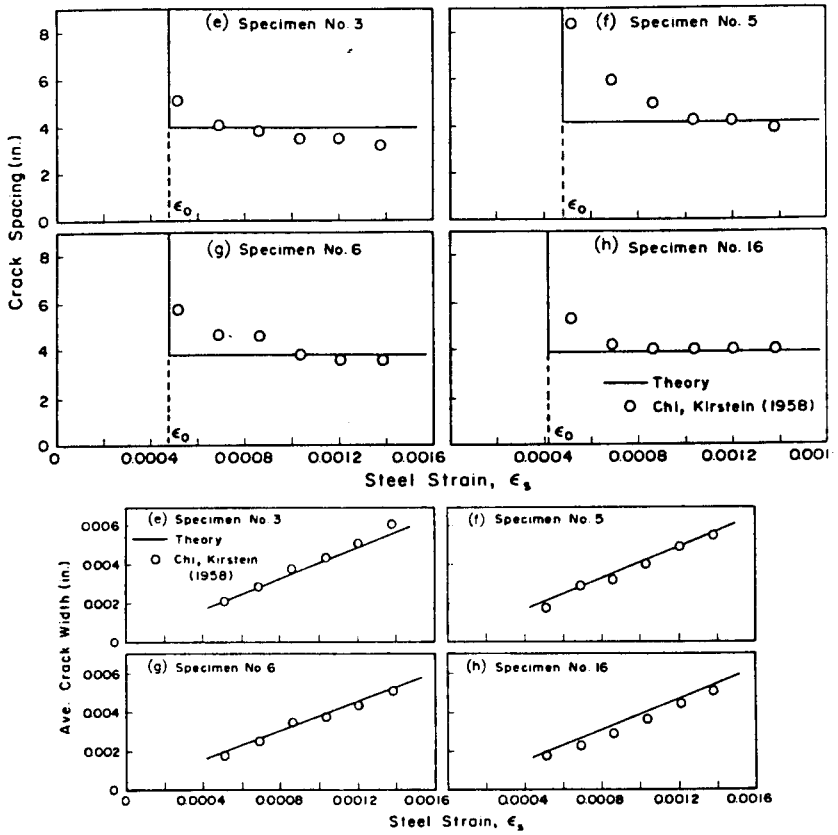

Fig. 1.30. Comparisons of theory with Chi and Kirstein's (1958) measurements of crack spacing and crack width (after Bažant and Oh, 1983).

$w = \varepsilon_s s$. Other data, e.g. those by Clark [101], Kaar and Mattock [102], Hognestad [103], and Mathey and Watstein [104] have been also successfully fitted [88].

Drying shrinkage cracks. Due to relatively small tensile strength and large shrinkage strains, drying typically produces cracks in concrete. If they are densely spaced and hair-thin they do little damage; however, long-time deformations are usually greatly affected. In particular, the drying creep as well as shrinkage cannot be realistically predicted without taking the effect of cracking and its evolution into account [105,106].

Consider just one typical problem: the initial spacing of drying cracks at the surface of a concrete halfspace. Using diffusion theory with given diffusivity of moisture in concrete, one can calculate profiles of specific moisture content of concrete at various times after the start of drying.

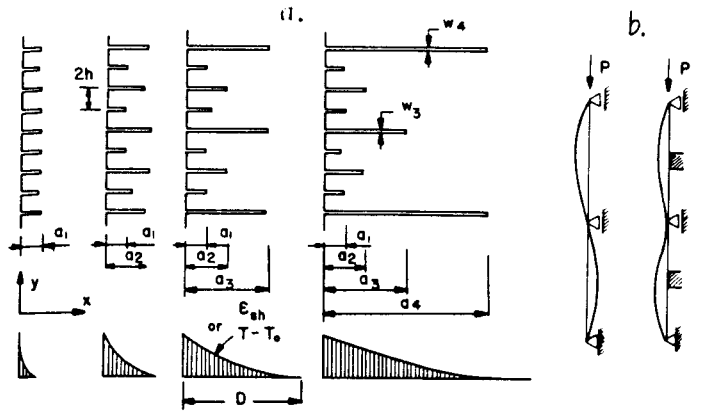

Fig. 1.31. System of parallel shrinkage or thermal cracks in a halfspace, and illustrations of constraint on instability mode by analogy with beam.

From these, one can get the profiles $\varepsilon_{sh}(x)$ of the free (unrestrained and incompatible) shrinkage strains. Assume that the environmental humidity is constant, and the moisture transmission at the surface is perfect. Then these profiles may be regarded as approximately parabolic.

Let x, y, z be Cartesian coordinates, x being normal to the halfspace surface. The stresses produced by the shrinkage strains may be solved from the conditions $(\sigma_y^0 - \nu\sigma_z^0)/E_{\text{eff}} - \varepsilon_{sh} = 0$ and $\sigma_z^0 = \sigma_y^0$, where ν = Poisson's ratio of concrete and $E_{\text{eff}} = E/(1+\phi)$ = effective modulus for elastic deformation plus creep, $\phi = \phi(t, t_0)$ = creep coefficient, which is a function of drying duration $t - t_0$ and age t_0 at drying start. Thus we obtain $\sigma_y^0 = \sigma_z^0 = \varepsilon_{sh}(x)E_{\text{eff}}/(1-\nu)$.

Assume now that a sudden formation of cracks normal to y-axis (Figure 1.31) reduces stress σ_y^0 to 0, i.e., the stress change is $\Delta\sigma_y = -\sigma_y^0$. Let $\Delta\sigma_z$ be the change of σ_z, and let $\Delta\varepsilon_y^m$ be the change of strain in concrete between the cracks. From Hooke's law $\Delta\varepsilon_y^m = (-\sigma_y^0 - \nu\Delta\sigma_z)/E$ and $\Delta\varepsilon_z = (\Delta\sigma_z + \nu\sigma_y^0)/E = 0$, the solution of which is $\Delta\sigma_z = -\nu\sigma_y^0$, $\Delta\varepsilon_y^m = -(1-\nu^2)\sigma_y^0/E$. The loss of strain energy due to cracking per unit area of halfspace surface is $\Delta W_1 = \int_0^D(\sigma_y^0 + \frac{1}{2}\Delta\sigma_y)\Delta\varepsilon_y^m dx$ or $\Delta W_1 = \int_0^D(\sigma_y^0/2)(1-\nu^2)(\sigma_y^0/E)dx = [E_{\text{eff}}/(1-\nu)]^2\int_0^D \varepsilon_{sh}^2(x)dx(1-\nu^2)/2E$. Assuming the profile of $\varepsilon_{sh}(x)$ to be parabolic, we may substitute $\varepsilon_{sh}(x) = (1 - x/D)^2\varepsilon_{sh}^0$ for $x \leqslant D$, and $\varepsilon_{sh}(x) = 0$ for $x \geqslant D$, where ε_{sh}^0 = constant = shrinkage strain at halfspace surface, and D = penetration depth of drying (which is a function of drying duration $t - t_0$). Integration then yields $\Delta W_1 = 0.1\ DE[\varepsilon_{sh}^0/(1+\phi)]^2(1+\nu)/(1-\nu)$.

Stresses σ_y^0 actually are not reduced completely to zero. Therefore, the actual potential energy release will be $r\Delta W_1$ where r is a certain fraction

$(0 < r < 1)$ which can be determined only by exact solution of the stress field. Probably r is between 0.6 and 0.8. The energy balance during crack formation requires that $r\Delta W_1 s \geq G_f a$, where a = crack depth. This yields the condition

$$s \geq \frac{10(1-\nu)G_f}{r(1+\nu)E}\left(\frac{1+\phi}{\varepsilon_{sh}^0}\right)^2 \frac{a}{D} \qquad \text{(energy)} \tag{1.68}$$

derived, without creep, in [99]. Note that factor $1/(1+\phi)$ is applied to ε_{sh}^0, not E. The cracks, however, form early in the drying process, and then $\phi \simeq 0$.

The ratio a/D, as well as the ratio a/s, can be determined by linear fracture analysis; this was done by finite elements [74], and yielded a/D as a certain function of D/s. For short cracks, one may use $a/D \simeq 1.5$ and $a \simeq 2s$ as very crude estimates.

For typical properties of concrete, Eq. 1.68 yields $s \simeq 5$ cm, and for typical properties of hardened portland cement paste, $s \simeq 3$ mm. The corresponding crack widths, calculated as $w \simeq s\varepsilon_{sh}^0$, are 0.03 mm for concrete, and 0.004 mm for cement paste [105]. Cracks as fine as this are obviously not visible. Moreover, they are so fine that they cannot be continuous. So, the drying cracks must begin as microcrack zones, which means that concrete may still transmit substantial normal tensile stress across the cracks. This is not necessarily so, however, at a later stage of drying, as it will be shown in the next section.

The strength criterion simply requires that $\sigma_y \geq f_t'$ or

$$\varepsilon_{sh}^0 \geq \frac{f_t'}{E}(1-\nu)(1+\phi) \qquad \text{(strength)}. \tag{1.69}$$

This criterion decides whether progressive microcracking can start but not whether complete cracks form.

If the surface shrinkage ε_{sh}^0 is sufficiently large, Eq. 1.69 is satisfied before Eq. 1.68 and then the initial drying cracks form gradually, statically. If ε_{sh}^0 is not large enough, the cracks can never initiate, regardless of the penetration depth D. However, some other disturbance can make the strength criterion satisfied, and then the cracks form dynamically.

In testing shrinkage and creep at drying, deleterious cracking may be avoided on very thin specimens if the environmental humidity is varied gradually and sufficiently slowly. Formulas indicating the maximum admissible drying rate have been developed [105]. Also, a formula for cracking of a tubular drying specimen has been derived, using the global energy balance for complete crack formation [105]. Another interesting question is a possible coupling between drying and cracking due to the effect of cracking on diffusivity.

Crack system instability. Whereas the cracks in a tensioned reinforced bar may become denser as the loading proceeds, in some other situations, they may become sparser. This is so for cracks growing toward a compression region, a typical example of which is the system of parallel equidistant drying cracks or cooling cracks growing perpendicularly to the surface of a halfspace (Fig. 1.31).

In general, the work, U, that needs to be done to produce cracks of lengths a_i in an elastic body may be expressed as [107,99]

$$U = W(a_1, a_2, \ldots, a_n; D) + \sum_{i=1}^{N} \int_0^{a_i} G_{f_i}\, da_i' \tag{1.70}$$

where W = strain energy, G_{f_i} = fracture energy = material property (which could depend on a_i), D = loading parameter which represents here the penetration depth of drying. The equilibrium state of cracks is characterized by a zero value of the first variation of U, i.e.,

$$\delta U = \sum_{i=1}^{m} (W_i + G_{f_i})\delta a_i + \sum_{j=m+1}^{k} W_j \delta a_j = 0 \tag{1.71}$$

where $W_i = -\partial W/\partial a_i$ = energy release rates; $i = 1, \ldots, m$ are the cracks which grow $(\delta a_i > 0)$; $j = m+1, \ldots, k$ are those which close $(\delta a_i < 0)$; and $i = k+1, \ldots, N$ are those which neither grow nor close $(\delta a_i = 0)$. Since Eq. 1.71 must be satisfied for any admissible δa_i, it follows, for equilibrium (nondynamic) crack extensions,

$$\text{for } \delta a_i > 0: \quad -W_i = G_{f_i}; \qquad \text{for } \delta a_i < 0: \quad W_i = 0. \tag{1.72}$$

The first condition is the well-known Griffith failure criterion [40], identical to Eq. 1.33. The cases $-W_i > G_{f_i}$ and $-W_i < 0$ cannot happen for equilibrium states because Eq. 1.71 could give $\delta U < 0$. So it follows that only the following crack length variations are admissible:

$$\begin{aligned} &\text{for } -W_i = G_{f_i}: && \delta a_i \geq 0 \\ &\text{for } 0 < -W_i < G_{f_i}: && \delta a_i = 0 \\ &\text{for } W_i = 0: && \delta a_i \leq 0 \end{aligned} \tag{1.73}$$

Equivalent statements can be made in terms of the stress intensity factors $K_i = (-W_i/E)^{1/2}$.

The question of stability of the states which satisfy the equilibrium conditions (Eq. 1.71) is decided by the second variation of W [107,99]:

$$\delta^2 U = \tfrac{1}{2}\sum_{i=1}^{n}\sum_{j=1}^{n} U_{ij}\delta a_i \delta a_j \begin{cases} > 0 \text{ for all admissible } \delta a_i \ldots \text{stable} \\ = 0 \text{ for some admissible } \delta a_i \ldots \text{critical} \\ < 0 \text{ for some admissible } \delta a_i \ldots \text{unstable} \end{cases} \tag{1.74}$$

in which $U_{ij} = \partial^2 U/\partial a_i \partial a_j$. When G_{f_i} are independent of a_i (the usual case, except if one uses the R-curve approach), $U_{ij} = W_{ij} = \partial^2 W/\partial a_i \partial a_j$. So, stability is decided not by the energy release rates but by their derivatives. Eq. 1.74 further implies

$$\det{}_n(U_{ij}) \begin{cases} > 0 \text{ for all } n, \delta a_i \text{ all admissible} \ldots \text{stable} \\ = 0 \text{ for some } n, \text{ admissible } \delta a_i \ldots \text{critical} \\ < 0 \text{ for some } n, \text{ admissible } \delta a_i \ldots \text{unstable} \end{cases} \tag{1.75}$$

where $\det_n$ = principal minors of matrix U_{ij} of sizes $n \leqslant N$. The eigenvector δa_i corresponding to the critical state is determined from the equation system [107,99]:

$$\sum_{j=1}^{n} U_{ij}\delta a_j = 0. \tag{1.76}$$

Consider now the parallel cracks that are initially of equal length (Figure 1.31), and examine when the increments of a_i can become different, alternating between δa_1 and δa_2. In the 2×2 matrix U_{ij} $(= W_{ij})$, there is the need to check the sign of $U_{22} = \det_1(U_{ij}) = \partial^2 U/\partial a_2^2$, and of $\det(U_{ij})$. If $\det(U_{ij}) = 0$, then $U_{12}U_{21} = U_{11}U_{22}$ or $U_{12}^2 = U_{11}^2$ (since $a_1 = a_2$), and the eigenvector is then given by $U_{11}\delta a_1 + U_{12}\delta a_2 = 0$ and $U_{21}\delta a_1 + U_{22}\delta a_2 = 0$. Thus, if $\partial U/\partial a_1 > 0$, it follows that $\delta a_2/\delta a_1 = -W_{11}/W_{21} = -W_{12}/W_{22}$. Now, since the energy release rates $(-\partial W/\partial a_i)$ should decrease with increasing a_i if the crack system is stable before the point of instability, it is expected that $W_{22} > 0$ and $W_{12} > 0$, and numerical calculations confirm that [107,99]. Thus, either δa_2 or δa_1 must be negative. A negative δa_i is, however, impossible if $-\partial W/\partial a_i = G_f$ (growing crack). So, this type of instability cannot happen.

This interesting situation is analogous to that of buckling of a continuous beam with two spans (Figure 1.31) which are constrained so that they can buckle only to the left. Without those one-sided constraints, the spans would buckle in opposite directions (the first critical state). The

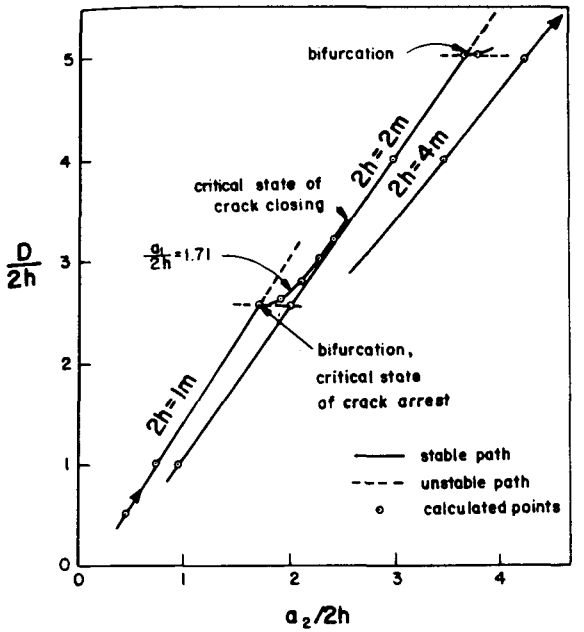

Fig. 1.32. Evolution of crack lengths in a system of parallel cracks in Fig. 31 (after Bažant, Ohtsubo, Aoh, 1979).

presence of one-sided constraints makes the first critical state inapplicable and causes that the beam can buckle only in the second critical mode, in which both spans deflect to the left. The same must happen for the crack system, i.e. instability can arise only due to the second critical condition, $W_{22} = 0$. In that case, since the eigenvector is given by $W_{22}\delta a_2 + W_{21}\delta a_1 = 0$, it follows that $W_{21}\delta a_1 = 0$, and since $W_{21} \neq 0$ according to numerical calculations, $\delta a_1 = 0$, while δa_1 cannot be negative since $-\partial W/\partial a_i = G_f$. So, there exists an instability such that $\delta a_1 > 0$ and $\delta a_2 = 0$ at constant D.

These conclusions and further, more detailed analysis [99] indicate the following evolution of the parallel crack system. Equally spaced drying cracks extend at first at equal length $(a_1 = a_2)$ as the drying front advances into the halfspace. The (2×2) determinant of $\partial^2 U/\partial a_1 \partial a_2$ vanishes first, but this does not represent any critical state. Subsequently, $\partial^2 U/\partial a_2^2$ vanishes, and this does represent a critical state at which each other crack gets arrested. Further growth of cracks at equal length is impossible since it is unstable (as $\partial^2 U/\partial a_2^2 < 0$), even though the energy balance condition (Eq. 1.71) is satisfied. Rather, cracks a_2 suddenly jump ahead at constant a_1 and constant D (Figure 1.32). Then cracks a_2 extend again gradually as the drying proceeds (D increases). At the same time, cracks a stop growing and $\partial U/\partial a_1$ gradually diminishes as a_2 and D increase, until $\partial U/\partial a_1$ becomes zero; this represents a second critical

state, which can be shown to correspond to a vanishing (2×2) determinant of U_{ij}. At this point, cracks a_2 suddenly close over a certain part of their length at constant a_2 and D. Thereafter, cracks a_2 grow at increasing D. Because cracks a_1 are closed, this is equivalent to the initial situation with equal crack lengths, but the spacing is doubled. The process then gets repeated at doubled spacing, quadrupled spacing, etc. (For a precise numerical calculation of this process, see [99].)

The foregoing behavior is true for a two-dimensional problem. In three dimensions, the behavior is similar but the cracks form hexagonal prisms rather than parallel planes. Some hexagon sides successively close and the hexagon sizes multiply, as the remaining cracks open ever more widely during drying. Drying mud-flats (in dried lakes) demonstrate this behavior [108,109].

The closing of cracks during the progress of drying has the effect that the spacing and the width of the open cracks doubles at each critical state. Numerical calculations [99,74] show that the lengths of the leading cracks and the spacing of the open cracks fluctuate within the limits

$$0.67\, D \leqslant a \leqslant 0.77\, D, \quad 0.39\, D \leqslant s \leqslant 0.61\, D \tag{1.77}$$

where the first limit corresponds to the start of closing of every other crack, and the second limit to the completion of their closing. According to these inequalities, the average crack length and average crack spacing are

$$a \simeq 0.72\, D, \quad s \simeq 0.69\, a \simeq 0.5\, D. \tag{1.78}$$

As the open cracks are getting more widely spaced, their opening w increases. Roughly, $w = s\varepsilon_{sh}$ (s = spacing). The drying cracks become visible when, roughly, $s\varepsilon_{sh} \geqslant 0.2$ mm, and considering that $\varepsilon_{sh} = 0.0006$, this happens for $s \geqslant 30$ cm, $D \geqslant 60$ cm and $a \geqslant 43$ cm. The required value D is so large that cracks caused by drying in massive concrete walls cannot become visible except after many years.

From the foregoing conclusion, it follows that the drying cracks normally are too narrow to form distinct, sharp, and continuous cracks. Rather, what has been referred to as cracks must be cracking bands (or microcrack bands). The foregoing conclusion does not apply in other situations, e.g., when cracking releases flexural strain energy. For example, thin-wall tubular specimens exposed to drying may develop longitudinal cracks in a radial plane. It was shown [105] that these cracks form when the shrinkage strain reaches the value

$$\varepsilon_{sh} = \left(\frac{1-\nu}{1+\nu} \frac{12 G_f}{\pi r E_{ef}} \right)^{1/2} \tag{1.79}$$

where r = radius up to midthickness of tube wall. For a typical cement paste specimen of $r = 7.5$ mm, the critical shrinkage strain is achieved by a drop from 100% to 90% relative humidity [105].

In various types of tests of concrete or cement paste specimens, e.g., in measurements of shrinkage and drying creep as a material property, sorption isotherms, internal surface areas, etc., it is important to make sure that no tensile cracks or microcracks be produced by drying (or cooling). This problem was analyzed in detail in [105] from the viewpoints of both linear and nonlinear diffusion theories. If one considers a linear time variation of surface humidity, a perfect moisture transmission at the surface, and a planar wall of thickness b, then the maximum rate of change of environmental relative humidity h_e to assure a crack-free state is found to be [105]

$$\mathrm{Max}\left(\frac{\mathrm{d}h_e}{\mathrm{d}t} \right) = 0.14 \frac{C}{b^2} \tag{1.80}$$

where C = moisture diffusivity. For typical properties of structural concrete, this gives the rate 2.2% humidity change per year for a 6-inch thick slab, which means that prevention of cracking cannot be assured in normal specimens. The bulk of existing test data grossly violates this condition. For an 0.75 mm thick wall, the maximum rate is 10% humidity change per hour, and so tests of material properties at drying must be carried out on extremely thin specimens, made of cement paste or fine mortar, if cracking should be avoided. (Note, however, that cracking can be also avoided by applying sufficient biaxial compression parallel to the surface, and then large specimens are usable.)

The gradual closing of some cracks at the expense of a wider opening of others exists in various other situations. For example, it has been demonstrated [75] that equally spaced bending cracks growing toward the neutral axis in an unreinforced or reinforced beam subjected to bending or eccentric compression can exhibit this type of behavior. However, it is also found that here this question is only academic since this type of behavior is possible only for reinforcement percentages below about 0.18%, which do not represent realistic situations. For normal reinforced beams and plates, the bending cracks do not exhibit the instability just analyzed and maintain the same spacing, which is analyzed in a preceding section from another viewpoint.

Crack path and shear fracture. The question of determining the crack path is rather difficult and the present knowledge is fragmentary. For many situations, it seems, one may assume that the crack propagates in such a direction that a Mode I situation would prevail at fracture front, (i.e., the stress and displacement fields would be symmetric). The Mode I

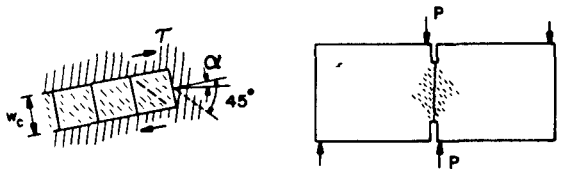

Fig. 1.33. Shear fracture as a band of inclined microcracks.

situation is justified by the experimental fact that, due to crack surface roughness, the ratio of crack slip increment to crack opening increment is nearly zero at very small openings [28]. However, if Mode I always applied, then shear fracture would be impossible, yet it exists in certain situations, e.g., that pictured in Figure 1.33 where the shear zone is narrow and concentrated. If the fracture would propagate in Mode I, it would extend in 45° inclined directions which would quickly bring the crack front into a zone of small principal tensile stress and arrest the crack.

Shear fractures probably develop as a band of 45° inclined microcracks, which themselves are of Mode I (symmetric) type (Figure 1.33). This concept of shear fracture can be modeled by finite elements using the blunt crack band approach. In this case, the fracture energy for the band of inclined cracks would probably be about the same as for tensile (Mode I) crack band, i.e., equal to G_f. However, the multiaxial stress state at the crack front needs to be taken into account. Thus, if the frontal element is subjected to pure shear, Eq. 1.22 ($\sigma_3 = -\sigma_1$) yields the equivalent strength in diagonal tension:

$$f'_{eq_{II}} = \frac{1}{\sqrt{1+2\nu'}} f'_{eq_I} \tag{1.81}$$

where f'_{eq_I} is the equivalent strength in pure tension (Mode I), as given by Eq. 1.22 with $r_f = 1$.

1.7 General model for progressive fracturing

Microplane Model. For some types of loading, especially the dynamic ones, it may happen that a principal tensile stress of direction z causes only partial cracking and fracture is completed later by superimposing another loading of different principal strain direction. For such situations, one needs a softening stress-strain relation that can be applied for general loading paths, in particular, loading paths with rotating principal

stress directions. For this purpose, the stress-strain relation used before (Eq. 1.12) needs to be generalized.

An attractive method to do this is the microplane model developed in [110,111]. This model is defined by specifying the constitutive properties by a relation between the stresses and strains acting within the microstructure on a plane of any orientation. This involves no tensorial invariance restrictions. These restrictions can then be satisfied by a suitable combination of planes of various orientations, e.g., in the case of isotropy, each orientation must be equally frequent.

The idea of defining the inelastic behavior independently on planes of different orientation within the material, and then in some way superimposing the inelastic effects from all planes, has a long history. It appeared in Taylor's work [112] on plasticity of polycrystalline metals. Batdorf and Budianski [113] formulated the slip theory of plasticity, in which the stresses acting on various planes of slip are obtained by resolving the macroscopic applied stress, and the plastic strains (slips) from all planes are then superimposed. The same superposition of inelastic strains was used in the so-called multilaminate models of Zienkiewics et al. [114] and Pande et al. [115,116], and in many works on plasticity of polycrystals. Recently, a model of this type was developed to describe tensile strain-softening due chiefly to microcracking [110]. While in previous works dealing with plasticity of polycrystals, the stresses on various microplanes were assumed to be equal to the resolved macroscopic stress, this new model uses a similar assumption for part of the total strains.

The resultants of the stresses acting on the weak planes over unit areas of the heterogeneous material will be called the microstresses, s_{ij}, and the strains of the heterogeneous material accumulated from the deformations on the microplanes will be called the microstrains, e_{ij}. With regard to the interaction between the micro- and macro-levels, one may introduce the following basic hypotheses [110,111].

Hypothesis I. The tensor of macroscopic strain, ε_{ij}, is a sum of a purely elastic macrostrain ε^a_{ij} that is unaffected by cracking, and an inelastic macrostrain e_{ij} which reflects the stress relaxation due to cracking, i.e.,

$$\varepsilon_{ij} = \varepsilon^a_{ij} + e_{ij} \tag{1.82}$$

Here, Latin lower case subscripts refer to Cartesian coordinates x_i ($i = 1, 2, 3$).

Hypothesis II. The normal microstrain e_n which governs the progressive development of cracking on a microplane of any orientation is equal to the resolved macroscopic strain tensor e_{ij} for the same plane, i.e.,

$$e_n = n_i n_j e_{ij} \tag{1.83}$$

in which n_i = direction cosines of the unit normal $\boldsymbol{n}$ of the microplane, and the repeated Latin lower case subscripts indicate a summation over 1, 2, 3.

Hypothesis III. The stress relaxation due to all microcracks normal to $\boldsymbol{n}$ is characterized by assuming that the microstress s_n on the microplanes of any orientation is a function of the normal microstrain e_n on the same plane, i.e.,

$$s_n = \frac{2\pi}{3} F(e_n). \tag{1.84}$$

The factor $(2\pi/3)$ is introduced just for convenience, as it will later cancel out.

The last hypothesis is similar to that made for shear microstresses and microstrains in the slip theory of plasticity. Hypothesis II is however opposite. There are three reasons for hypothesis II:

(1) Using resolved stresses rather than strains on the microplanes would hardly allow describing strain-softening, since, in this case, there are two strains corresponding to a given stress but only one stress corresponding to a given strain.

(2) The microstrains must be stable when the macrostrains are fixed. It has been experienced numerically that, in the case of strain-softening, the model becomes unstable if resolved stresses rather than strains are used.

(3) The use of resolved strains, rather than stresses, seems to reflect the microstructure of a brittle aggregate material better. The use of resolved stresses is reasonable for polycrystalline metals in which local slips scatter widely while the stress is roughly uniformly distributed throughout the microstructure. By contrast, in a brittle aggregate material consisting of hard inclusions embedded in a weak matrix, the stresses are far from uniform, having sharp extremes at the locations where the surfaces of aggregate pieces are nearest. The deformation of the thin layer of matrix between two aggregate pieces, which yields the major contribution to inelastic strain, is determined chiefly by the relative displacements of the centroids of the two aggregate pieces, which roughly correspond to the macroscopic strain. The microplanes may be imagined to represent the thin layers of matrix and the bond planes between two adjacent aggregate pieces (Figure 1.34), since microcracking is chiefly concentrated there.

In Hypothesis III, the relaxation of shear microstresses s_{nt} caused by the shear and normal microstrains e_{nt} and e_n is neglected. This assumption is probably quite good for very small crack openings, since it has been deduced from test data on shearing of cracks in concrete that no relative shear displacements on the rough interlocked cracks is possible before a certain finite crack opening is produced, and that the shear

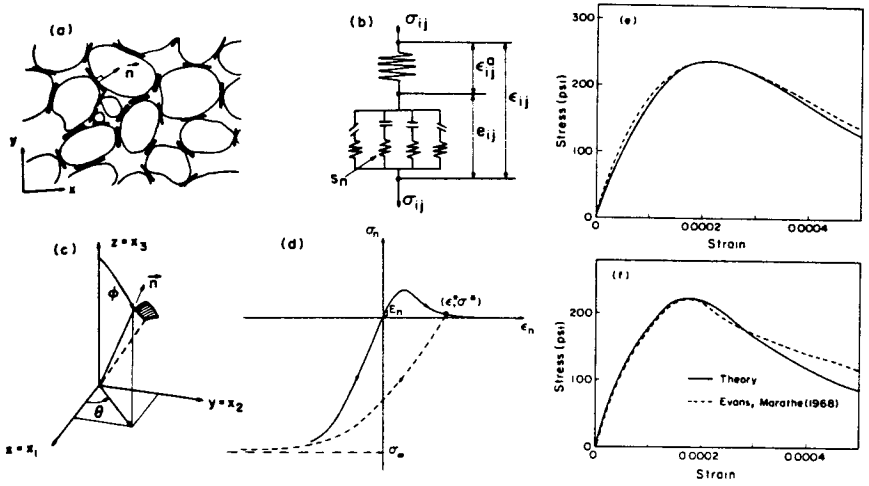

Fig. 1.34. Explanations for microplane model (a–d), and comparison with tests of Evans and Marathe (1968) (e–f).

stiffness of the cracks decreases rather slowly as the crack gradually opens. One must admit, however, that Eq. 1.84 (Hypothesis III) is also useful for its simplicity. It would be much more complicated to assume a general relation between the normal and shear microstresses and microstrains on each plane.

The virtual work of stresses per unit volume may be written, according to Eq. 1.82, as $\delta W = \sigma_{ij}\delta\varepsilon_{ij} = \sigma_{ij}\delta\varepsilon^a_{ij} + \sigma_{ij}\delta e_{ij}$. Summing the virtual work due to $\delta\varepsilon^a_{ij}$ and δe_{ij}, it gives $\delta W = \sigma^a_{ij}\delta\varepsilon^a_{ij} + s_{ij}\delta e_{ij}$, in which s_{ij} is the macrostress tensor resulting from s_n on all planes, and σ^a_{ij} is the stress tensor corresponding to ε^a_{ij}. Since both expressions for δW must hold for any $\delta\varepsilon^a_{ij}$ and any δe_{ij}, $s_{ij} = \sigma^a_{ij} = \sigma_{ij}$. Equilibrium conditions may be expressed by means of the principle of virtual work:

$$\delta W^c = \tfrac{4}{3}\pi\sigma_{ij}\delta e_{ij} = 2\int_S s_n \delta e_n f(\boldsymbol{n})\mathrm{d}S \tag{1.85}$$

in which S represents the surface of a unit hemisphere, the factor $(4\pi/3)$ is due to integrating over the surface of a sphere of radius 1, and $\mathrm{d}S = \sin\delta\mathrm{d}\theta\mathrm{d}\phi$ (Figure 1.34c). Note that there is no need to integrate over the entire surface of the sphere, since the values of σ_n or e_n are equal at any two diametrically opposite points on the sphere. Function $f(\boldsymbol{n})$ introduces the relative frequency of planes of various orientations $\boldsymbol{n}$, contributing to inelastic stress relaxation.

Substituting Eqs. 1.83 and 1.84 into Eq. 1.85 yields $\sigma_{ij}\delta e_{ij} =$

$\int_S F(e_n) n_i n_j \delta e_{ij} f(\boldsymbol{n}) \mathrm{d}S$, and because this must hold for any δe_{ij} it gives

$$\sigma_{ij} = \int_0^{2\pi} \int_0^{\pi/2} F(e_n) n_i n_j f(\boldsymbol{n}) \sin\phi \mathrm{d}\phi \mathrm{d}\theta. \tag{1.86}$$

Furthermore, according to Eq. 1.83, $\mathrm{d}F(e_n) = F'(e_n)\mathrm{d}(e_n) = F'(e_n) n_k n_m \mathrm{d}e_{km}$, and thus the differentiation of Eq. 1.86 finally yields

$$\mathrm{d}\sigma_{ij} = D^c_{ijkm} \mathrm{d}e_{km} \tag{1.87}$$

in which [110,111]

$$D^c_{ijkm} = \int_0^{2\pi} \int_0^{\pi/2} a_{ijkm} F'(e_n) f(\boldsymbol{n}) \sin\phi \mathrm{d}\phi \mathrm{d}\theta, \quad \text{with} \quad a_{ijkm} = n_i n_j n_k n_m. \tag{1.88}$$

D^c_{ijkm} may be called the tangent stiffnesses of the microplane system. Noting that the sequence of subscripts of D^c_{ijkm} is immaterial, it is seen that there are only six independent values of incremental stiffnesses. Eq. 1.88 applies to initially anisotropic solids. For isotropic solids, substitute $f(\boldsymbol{n}) = 1$.

The mathematical structure of the present model may be geometrically visualized with the rheologic model in Figure 1.34b.

The compliance corresponding to the additional elastic strain σ^a_{ij} must satisfy isotropy conditions, and so

$$C^a_{ijkm} = \frac{1}{9K^a}\delta_{ij}\delta_{km} + \frac{1}{2G^a}\left(\delta_{ik}\delta_{jm} - \tfrac{1}{3}\delta_{ij}\delta_{km}\right) \tag{1.89}$$

in which K^a and G^a are certain bulk and shear moduli which cannot be less than the actual initial bulk and shear moduli K and G. For fitting of test data, it was assumed, with success, that $1/G^a = 0$ [110].

Recalling Eq. 1.82 (and Figure 1.34b), the incremental stress-strain relation may be written as

$$\mathrm{d}\sigma_{ij} = D_{ijkm}\mathrm{d}\varepsilon_{km}, \quad \text{with} \quad \left[D_{ijkm}\right] = \left[\left(\mathbf{D}^{c^{-1}}\right)_{ijkm} + C^a_{ijkm}\right]^{-1}. \tag{1.90}$$

Applying Eq. 1.88 to elastic deformations (with $f(\boldsymbol{n}) = 1$), one finds that the matrix in Eq. 1.88 always yields Poisson's ratio $\nu = 1/4$. This is because the microplane shear stiffnesses are neglected. Since $\nu = 1/4$ is not quite true for concrete, the additional elastic strain must be used to make a correction. Now, determine the value of K^a needed to achieve the desired Poisson's ratio ν. Let superscripts c and a distinguish between the values corresponding to D^c_{ijkm} and C^a_{ijkm}. For uniaxial stress, it is found

that $\varepsilon_{11} = \sigma_{11}/9K^a + \sigma_{11}/E^c$ and $\varepsilon_{22} = \sigma_{11}/9K^a - \nu^c\sigma_{11}/E^c$ in which $\nu^c = 1/4$ and $E^c = 2\pi E_n/5$, $E_n = F'(0)$ = initial normal stiffness for the microplane. Since $\varepsilon_{22} = -\nu\varepsilon_{11}$, it follows that [110,111]:

$$K^a = \frac{1+\nu}{9(\nu^c - \nu)}E^c \qquad (\text{for } \nu \leqslant \nu^c). \tag{1.91}$$

This is, of course, under the assumption that $1/G^a = 0$.

The stress–strain relation for the microplanes, relating σ_n to ε_n, must describe cracking all the way to complete fracture, at which σ_n reduces to zero. In view of the kinematics visualized in Figure 34d, it is clear that σ_n as a function of ε_n must first rise, then reach a maximum, and then gradually decline to zero. The final zero value is chosen to be attained asymptotically, since no precise information exists on the final strain at which $\sigma_n = 0$, and since a smooth curve is convenient computationally. The following expressions were used in computations [110] (Figure 1.34d):

$$\text{for } e_n > 0\text{: } \sigma_n = E_n e_n e^{-(k e_n^p)}, \quad \text{for} \quad e_n \leqslant 0\text{:} \quad \sigma_n = E_n e_n \tag{1.92}$$

in which E_n, k and p are positive constants; $k = 1.8 \times 10^7$, $p = 2$.

The integral in Eq. 1.88 has to be evaluated numerically, approximating it by a finite sum [110,111]

$$D^c_{ijkm} = \sum_{\alpha=1}^{N} w_\alpha \left[a_{ijkm} F'(e_n)\right]_\alpha. \tag{1.93}$$

in which α refers to the values at certain numerical integration points on a unit hemisphere (i.e., certain directions), and w_α are the weights associated with the integration points. Since in finite element programs for incremental loading, the numerical integration needs to be carried out a great number of times, a very efficient numerical integration formula is needed. For the slip theory of plasticity, the integration was performed using a rectangular grid in the $\theta - \phi$ plane. This formula is, however, computationally inefficient since the integration points are crowded near the poles, and since in the $\theta - \phi$ plane, the singularity arising from the poles takes away the benefit from a use of high-order integration formula.

Optimally, the integration points should be distributed over the spherical surface as uniformly as possible. A perfectly uniform subdivision is obtained when the microplanes normal to the α-directions are the faces of a regular polyhedron. A regular polyhedron with the most faces is the icosahedron, for which $N = 10$ (half the number of faces); such a formula was proposed by Albrecht and Collatz [118].

TABLE 1.2
Direction cosines and weights for 2×21 points (integrates exactly 9-th degree polynomials).

α	x_1^α	x_2^α	x_3^α	w^α
1	0.1875924741	0	0.9822469464	0.01984126984
2	0.7946544723	−0.5257311121	0.3035309991	0.01984126984
3	0.7946544723	0.5257311121	0.3035309991	0.01984126984
4	0.1875924741	−0.8506508084	−0.4911234732	0.01984126984
5	0.7946544723	0	−0.6070619982	0.01984126984
6	0.1875924741	0.8506508084	−0.4911234732	0.01984126984
7	0.5773502692	−0.3090169944	0.7557613141	0.02539682540
8	0.5773502692	0.3090169944	0.7557613141	0.02539682540
9	0.9341723590	0	0.3568220897	0.02539682540
10	0.5773502692	−0.8090169944	−0.1102640897	0.02539682540
11	0.9341723590	−0.3090169944	−0.1784110449	0.02539682540
12	0.9341723590	0.3090169944	−0.1784110449	0.02539682540
13	0.5773502692	0.8090169944	−0.1102640897	0.02539682540
14	0.5773502692	−0.5	−0.6454972244	0.02539682540
15	0.5773502692	0.5	−0.6454972244	0.02539682540
15	0.3568220898	−0.8090169944	0.4670861795	0.02539682540
17	0.3568220898	0	−0.9341723590	0.02539682540
18	0.3568220898	0.8090169944	0.4670861795	0.02539682540
19	0	−0.5	0.8660254038	0.02539682540
20	0	−0.5	−0.8660254038	0.02539682540
21	0	1	0	0.02539682540

Numerical experience revealed, however, that 10 points are not enough when strain-softening takes place; it was found that the strain-softening curves calculated for uniaxial tensile stresses oriented at various angles with regard to the α-directions significantly differ from each other, even though within the strain-hardening range the differences are not very large. Therefore, more than 10 points are needed, and then a perfectly uniform spacing of α-directions is impossible.

Bažant and Oh [119] developed numerical integration formulas with more than 10 points, which give consistent results even in the strain-softening range. The most efficient formulas, with a nearly uniform spacing of α-directions, are obtained by certain subdivisions of the faces of an icosahedron and/or a dodecahedron [119]. Such formulas do not exhibit orthogonal symmetries. Other formulas which do were also developed [119]. Taylor series expansions on a sphere were applied and the weights w_α were solved from the condition that the greatest possible number of terms of the Taylor series expansion of the error would cancel out. The angular directions of certain integration points were further determined so as to minimize the error term of the expansion. Formulas involving 16, 21, 33, 37 and 61 points were derived, with errors of 10th, 12th and 14th order. Tables 1.2 and 1.3 define two of these numerical integration formulas, with 21 and 25 points, one without, and one with

TABLE 3
Direction cosines and weights for 2×25 points (integrates exactly 11-th degree polynomials) *.

α	x_1^α	x_2^α	x_3^α	w^α
1	1	0	0	0.01269841058
2	0	1	0	0.01269841058
3	0	0	1	0.01269841058
4	0.7071067812	0.7071067812	0	0.02257495612
5	0.7071067812	−0.7071067812	0	0.02257495612
6	0.7071067812	0	0.7071067812	0.02257495612
7	0.7071067812	0	−0.7071067812	0.02257495612
8	0	0.7071067812	0.7071067812	0.02257495612
9	0	0.7071067812	−0.7071067812	0.02257495612
10	0.3015113354	0.3015113354	0.9045340398	0.02017333557
11	0.3015113354	0.3015113354	−0.9045340398	0.02017333557
12	0.3015113353	−0.3015113354	0.9045340398	0.02017333557
13	0.30151113354	−0.3015113354	−0.9045340398	0.02017333557
14	0.3015113354	0.9045340398	0.301513354	0.02017333557
15	0.3015113354	0.9045340398	−0.3015113354	0.02017333557
16	0.3015113354	−0.9045340398	0.3015113354	0.02017333557
17	0.3015113354	−0.9045340398	−0.3015113354	0.02017333557
18	0.9045340398	0.3015113354	0.3015113354	0.02017333557
19	0.9045340398	0.3015113354	−0.3015113354	0.02017333557
20	0.9045340398	−0.3015113354	0.3015113354	0.02017333557
21	0.9045340398	−0.3015113354	−0.3015113354	0.02017333557
22	0.5773502692	0.5773502692	0.5773502692	0.02109375117
23	0.5773502692	0.5773502692	−0.5773502692	0.02109375117
24	0.5773502692	−0.5773502692	0.5773502692	0.02109375117
25	0.5773502692	−.05773502692	−0.5773502692	0.02109375117

$\beta = 25.239401°$

* Note added in proof: This formula was previously obtained by McLaren and is given by Stroud [178] with better accuracy than here.

orthogonal symmetry. These formulas give sufficient accuracy for most practical purposes. For crude calculations, a formula with 16 points [119] may sometimes also suffice. The directions of integration points are illustrated in Fig. 1.35. Also shown are the stress-strain diagrams calculated with the formula for uniaxial tension applied in various directions with regard to the integration points (directions a, b, c, d,...); the spread of the curves characterizes the range of error.

The following numerical algorithm may be used for the microplane model:

(1) Determine $e_n^{(\alpha)}$ from Eqs. 1.82 and 1.83 for all direction $\alpha = 1, \ldots, N$. In the first iteration of the loading step, use ε_{ij} for the end of the previous step, and in subsequent iterations, use the value of ε_{ij} determined for the mid-step in the previous iteration. In structural analysis, repeat this for

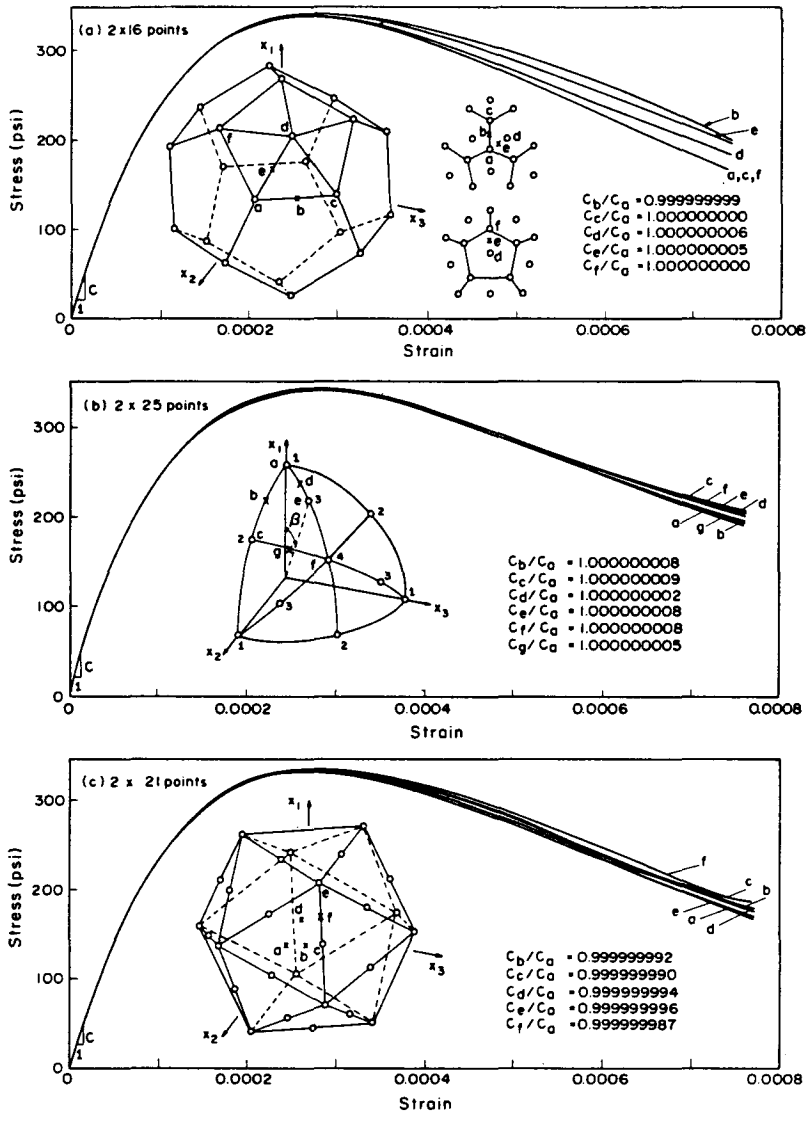

Fig. 1.35. Directions of integration points for some integration formulas for the surface of a sphere, and response curves for universal tension in direction a, b, c, d,... (after Bažant and Oh, 1983).

all finite elements and for all integration points within each finite element.

(2) For all directions $n^{(\alpha)}$, evaluate $F'(e_n)$ for use in Eq. 1.93. Also check for each direction whether unloading occurs, as indicated by violation of the condition $s_n \Delta e_n \geqslant 0$. If violated, replace $F'(e_n)$ with the

unloading stiffness (which may be approximately taken as E_n; however, a better expression exists [120]).

(3) Evaluate D^c_{ijkm} from Eq. 1.88 and D_{ijkm} from Eq. 1.90. In structural analysis, repeat this for all elements and all integration points in each element. When solving stress-strain curves, calculate then the increments of unknown stresses and unknown strains from Eq. 1.90. In structural analysis, solve (by the finite element method) the increments of nodal displacements from the given load increments, and subsequently calculate the increments of ε_{ij} and σ_{ij} for all elements and all integration points in each element. Then advance to the next iteration of the same loading step, or advance to the next loading step.

In simulating uniaxial tensile loading of fixed direction, the unloading criterion is not important since the only unloading occurs at moderate compressive stresses, for which a perfectly elastic unloading may be assumed.

The microplane model can be calibrated by comparison with direct tensile tests which cover the strain-softening response. Such tests, which can be carried out only in a very stiff testing machine and on sufficiently small test specimens, have been performed by Evans and Marathe [21] as well as others [22–25]. Optimal values of the three parameters of the model, E_n, k, and p, have been found [110] so as to achieve the best fits of the data of Evans and Marathe. Some of these fits are shown as the solid lines in Figure 1.34, and the data are shown as the dashed lines. A better test of the model would, of course, be a tensile test under rotating principal stress directions, but such tests have not yet been performed.

Note that, in this theory, one has only two material parameters, E_n and k, to determine by fitting test data. Trial-and-error approach is sufficient for that.

Shear in cracked concrete. The microplane model just described appears capable of modeling also the resistance of cracks in concrete for shear, characterized by crack friction (aggregate interlock effect) and dilatancy. For this purpose, the model needs to be enhanced by more realistic $\sigma_n - \varepsilon_n$ curves for unloading, and if cyclic shearing is considered, then also for reloading. This was done in [120].

Test data are available only for shear loading of blocks (Figure 1.36a) that have been previously fully cracked in tension [28,121–126]. Even though a finite separation is evident from the relative displacement of the blocks, the resistance to shear is not zero, not even at the beginning of shear. Obviously, there must be some contacts between the opposite surfaces even after the tensile stress normal to the crack has already been reduced to zero.

Using the microplane model, we treat the distinct crack in a rectangular test specimen as a band of certain finite width, w_c. This is probably

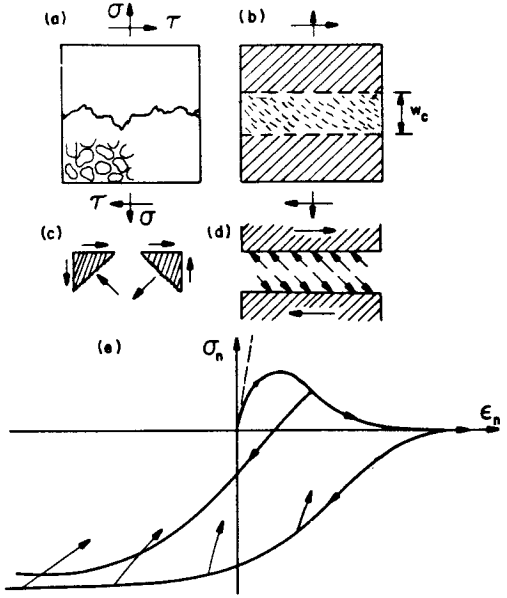

Fig. 1.36. Shear resistance of crack modeled by crack band.

not too unrealistic in view of the roughness of the crack surface, as well as the fact that concrete near the crack must have been microcracked during its previous tensile loading that produced the crack. In numerical simulation, one starts with an intact concrete and implements first uniaxial tensile loading in direction z until the stress σ_z is reduced to zero (in practice, to 0.001 f_t'). Subsequently, either a shear stress τ_{xz} or a shear strain γ_{xz}, depending on the conditions of simulated test, is gradually applied in small increments; see Figure 1.36b. Doing this, the normal strain ε_n on the microplanes inclined $+45°$ (Figure 1.36c) is increased, and so σ_n remains zero on these microplanes. However, ε_n on the microplanes inclined $-45°$ (Figure 1.36c) is decreased, and so contraction (unloading) occurs on those microplanes. For contraction, the normal stiffness is non-zero. Therefore, shear produces in the crack band a set of inclined compression forces illustrated in Figure 1.36d. These forces have a component along the crack, representing crack friction, and a component normal to the crack, representing the pressure opposing dilatancy. If such a pressure is not generated by the support conditions, then a simultaneous expansion (dilatancy) occurs so as to reduce the normal force component to zero.

Figure 1.36e shows the unloading σ_n–ε_n curves that have been used in [120], in which analytical expressions for these unloading curves may be found. Typical response curves which have been simulated with the microplane model are shown in Figure 1.37, where they are compared

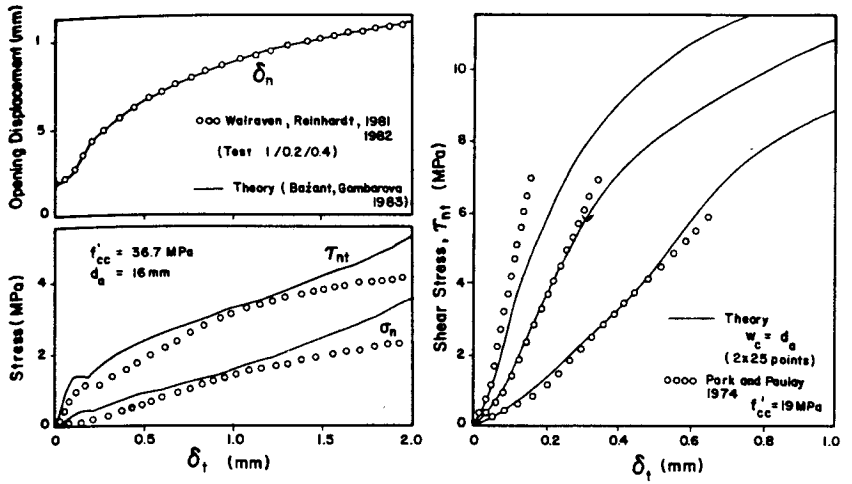

Fig. 1.37. Comparison of crack band model with measurements by Walraven and Reinhardt (1981, 1982) and Park and Paulay (1974) (after Bažant and Gambarova, 1983).

with the data points obtained in Paulay and Loeber tests [121]. In [120], it was shown that this model can fit essentially all the existing data on aggregate interlock or crack shear.

Thus we have a model which correctly describes both the tensile strain-softening up to full fracture and the crack shear in fully fractured concrete. It may be expected that the model would also represent the shear resistance of partially cracked concrete, and perhaps also shear fracture. Another possible use is biaxial (spatial) nonproportional shear loading, i.e., loading of the crack plane by shear stresses τ_{xz} and τ_{yz} (or shear strains γ_{xz} and γ_{yz}) which do not increase in proportion.

If a simultaneous representation of both tensile fracture and crack shear is not needed, one may of course use simpler models consisting in a relation between the stress and relative displacement on the crack. For a realistic description, one must use (in 2 dimensions) both the normal and tangential relative displacements δ_n and δ_t across a crack, and describe the normal and shear stresses on the crack, σ_n and σ_{nt}, as a function of δ_n and δ_t. In an incremental form, such a relation may be written as

$$\begin{Bmatrix} d\sigma_{nn} \\ d\sigma_{nt} \end{Bmatrix} = \begin{bmatrix} B_{nn} & B_{nt} \\ B_{tn} & B_{tt} \end{bmatrix} \begin{Bmatrix} d\delta_n \\ d\delta_t \end{Bmatrix} \tag{1.94}$$

in which $B_{nn}, \ldots, B_{tt}$, called crack stiffness coefficients, depend on δ_n and δ_t. A model of this type was developed and callibrated by test data in [28].

Experimental evidence [28,121–127] reveals that the crack stiffness coefficients are extremely variable depending on the normal and tangen-

tial displacements across the crack. For very small openings, the cracks present a very large resistance to shear, while for large crack openings, this resistance may become quite small. At small crack openings, even a small tangential displacement produces large compressive stresses if dilation of the crack is prevented, while for a wide crack even large tangential displacements do not produce large compressive stresses.

Considering a system of dense, parallel and equidistant cracks, and superimposing the deformations on the crack and those due to solid concrete between the cracks, one can obtain the flexibility matrix of cracked concrete. For small crack openings, this matrix can be written in the following explicit form [28]:

$$\begin{Bmatrix} d\varepsilon_n \\ d\varepsilon_t \\ d\gamma_{nt} \end{Bmatrix} = \begin{bmatrix} C_{11} + A|\sigma_{nt}|^p \sigma_{nn}^{-2}, & C_{12}, & \pm Ap|\sigma_{nt}|\sigma_{nm}^{-1} \\ C_{21}, & C_{22}, & 0 \\ \pm B|\sigma_{nt}|^{p+1}\sigma_{nn}^{-2}, & 0 & C_{33} + 3(p+1)|\sigma_{nt}|\sigma_{nn}^{-1} \end{bmatrix} \begin{Bmatrix} d\sigma_n \\ d\sigma_t \\ d\sigma_{nt} \end{Bmatrix} \tag{1.95}$$

in which A, B, p = material constants which depend on crack spacing; $C_{11}, \ldots, C_{33}$ = flexibility coefficients for the concrete between the cracks, which should properly be larger than those for intact concrete and should reflect the damage done to concrete during previous tensile loading which produced the cracks. The $\pm$ signs refer to shear to the left and to the right. Note that this matrix contains large off-diagonal terms which determine normal stress produced by the shear strain in confined concrete, as well as the shear deformation caused by a change in normal strain at constant shear stress. These effects are neglected in those models in which crack response to shear is described only by assuming a finite, smaller than elastic, shear stiffness.

As a cruder approximation, the crack stiffness matrix can be obtained by assuming frictional dilatant slip with a constant friction coefficient k and a constant dilatancy ratio α_d, defining the magnitude of the ratio of normal to tangential relative displacements across the crack. The result is [29]

$$\begin{Bmatrix} d\sigma_n \\ d\sigma_t \\ d\sigma_{nt} \end{Bmatrix} = \begin{bmatrix} 1 & \nu & \pm 2\alpha_d \\ \nu & \dfrac{E_c}{E^*} + \nu^2 & \pm 2\alpha_d \nu \\ \pm k & \pm k\nu & (\pm 2\alpha_d)(\pm k) \end{bmatrix} \begin{Bmatrix} d\varepsilon_n \\ d\varepsilon_t \\ d\varepsilon_{nt} \end{Bmatrix}. \tag{1.96}$$

It is interesting that this matrix is singular, which is a consequence of the friction relation. However, this singularity does not cause problems in reinforced concrete analysis because the deformation is stabilized by reinforcement or the boundary restraint.

Finally, it should be pointed out that if the slip of cracks should be prevented by reinforcement, then the reinforcement required to balance given loads is larger than that when crack friction is neglected. This is because the tensile reinforcement must balance not only the applied loads but also the normal component of friction on the cracks [117,73]. Consideration of friction leads to a reinforcement design for which the maximum deformations of orthogonally reinforced concrete, which occur in the diagonal directions, are significantly less than for the design in which friction is neglected.

1.8 Conclusion

In conclusion of the present work, it may be emphasized that fracture mechanics offers a realistic and consistent approach to the analysis of cracking in concrete structures. The form of the fracture mechanics to be used must be nonlinear, taking into account the existence at the fracture front of a finite nonlinear zone in which the material undergoes progressive microcracking. This type of fracture modeling is objective in that it is independent of the chosen mesh, and it gives a correct structural size effect. The effect of structure size on the apparent (nominal) strength of concrete is the most important salient feature of fracture mechanics. The present crack band theory gives the size effect as a gradual transition from failures governed by the strength limit to failures governed by fracture energy, with linear fracture mechanics as the limit for very large structures. It appears that introduction of such a size effect into various existing provisions of design codes, such as the ACI Code [65] or the CEB-FIP Model Code [47] would improve the predictions of structural response, particularly when the structure to be designed is much larger than the laboratory structures that were used to verify and calibrate the code provisions. In the writer's opinion, improvement in regard to the size effect should be taken as one important goal for further code development.

References

1. Bažant, Z.P., and Oh. B.H., Crack Band Theory for Fracture of Concrete, Materials and Structures (RILEM, Paris), Vol. 16, pp. 155–177 (1983) (based on [130]).
2. Bažant, Z.P., and Kim, S.S., Plastic-Fracturing Theory for Concrete, Journal of the Engineering Mechanics Division, ASCE, Vol. 105, No. EM3, Proc. Paper 14653, pp. 407–428 (1979).
3. Bažant, Z.P., Crack Band Model for Fracture of Geomaterials, Proc., 4th Intern. Conf. on Numerical Methods in Geomechanics, held in Edmonton, Alberta, Canada, ed. by Z. Eisenstein, Vol. 3 (1982), pp. 1137–1152.

4. Bažant, Z.P., Instability, Ductility and Size Effect in Strain-Softening Concrete, J. of the Engineering Mechanics Division ASCE, Vol. 102, No. EM2, pp. 331–344 – Paper 12042 (1976).
5. Bažant, Z.P., and Panula, L., Statistical Stability Effects in Concrete Failure, J. of the Engineering Mechanics Division, ASCE, Vol. 104, No. EM5, pp. 1195–1212, Paper 14074 (1978).
6. Bažant, Z.P., and Cedolin, L., Blunt Crack Band Propagation in Finite Element Analysis, Journal of the Engineering Mechanics Division, ASCE, Vol. 105, No. EM2, Proc. Paper 14529, pp. 297–315 (1979).
7. Cedolin, L., and Bažant, Z.P., Effect of Finite Element Choice in Blunt Crack Band Analysis, Computer Methods in Applied Mechanics and Engineering, Vol. 24, No. 3, pp. 305–316 (1980).
8. Rashid, Y.R., Analysis of Prestressed Concrete Pressure Vessels, Nuclear Engng. and Design, Vol. 7, No. 4, pp. 334–344 (1968).
9. Mindess, S., and Diamond, S., A Preliminary SEM Study of Crack Propagation in Mortar, Cement and Concrete Research, Vol. 10, pp. 509–519 (1980).
10. Cedolin, L., Dei Poli, S., and Iori, L. Experimental Determination of the Fracture Process Zone in Concrete, Cement and Concrete Research, Vol. 13, pp. 557–567 (1983).
11. Cedolin, L., dei Poli, S., and Iori, L., Experimental Determination of the Stress–Strain Curve and Fracture Zone for Concrete in Tension, Proc., Int. Conf. on Constitutive Laws for Engineering Materials, ed. by C. Desai, University of Arizona, Tucson (1983).
12. Barenblatt, G.I., The Formation of Equilibrium Cracks During Brittle Fracture, General Ideas and Hypothesis. Axially-Symmetric Cracks, Prikladnaya Matematika i Mekhanika, Vol. 23, No. 3, pp. 434–444 (1959).
13. Dugdale, D.S., Yielding of Steel Sheets Containing Slits, J. Mech. Phys. Solids, Vol. 8, pp. 100–108 (1960).
14. Kfouri, A.P., and Miller, K.J., Stress Displacement, Line Integral and Closure Energy Determinations of Crack Tip Stress Intensity Factors, Int. Journal of Pres. Ves. and Piping, Vol. 2, No. 3, pp. 179–191 (1974).
15. Kfouri, A.P., and Rice, J.R., Elastic/Plastic Separation Energy Rate for Crack Advance in Finite Growth Steps, in Fracture 1977 (Proc. of the 4th Intern. Conf. on Fracture, held in Waterloo, Ontario, June 1977), ed. by D.M.R. Taplin, University of Waterloo Press, Vol. 1, pp. 43–59 (1977).
16. Knauss, W.C., On the Steady Propagation of a Crack in a Viscoelastic Sheet; Experiments and Analysis, in The Deformation in Fracture of High Polymers, ed. by H.H. Kausch, Pub. Plenum Press, pp. 501–541 (1974).
17. Wnuk, M.P., Quasi-Static Extension of a Tensile Crack Contained in Viscoelastic Plastic Solid, Journal of Applied Mechanics, ASME, Vol. 41, No. 1, pp. 234–248 (1974).
18. Hillerborg, A., Modéer, M., and Petersson, P.E., Analysis of Crack Formation and Crack Growth in Concrete by Means of Fracture Mechanics and Finite Elements, Cement and Concrete Research, Vol. 6, pp. 773–782 (1976).
19. Petersson, P.E., Fracture Energy of Concrete; Method of Determination, Cement and Concrete Research, Vol. 10, 1980, pp. 78–89, and Fracture Energy of Concrete: Practical Performance and Experimental Results, Cement and Concrete Research, Vol. 10, pp. 91–101 (1980).
20. Suidan, M., and Schnobrich, W.C., Finite Element Analysis of Reinforced Concrete, Journal of the Structural Division, ASCE, Vol. 99, No. ST10, Proc. Paper 10081, pp. 2109–2122 (1973).
21. Evans, R.H., and Marathe, M.S., Microcracking and Stress-Strain Curves for Concrete in Tension, Materials and Structures (RILEM, Paris), No. 1, Jan.–Feb., pp. 61–64 (1968).
22. Heilmann, H.G., Hilsdorf, H.H., and Finsterwalder, K., Festigkeit und Verformung von Beton unter Zugspanungen, Deutscher Ausschuss für Stahlbeton, Heft 203, W Ernst & Sohn, West Berlin (1969).
23. Rüsch, H., and Hilsdorf, H., Deformation Characteristics of Concrete under Axial Tension, Voruntersuchungen, Bericht Nr. 44, Munich (1963).
24. Hughes, B.P., and Chapman, G.P., The Complete Stress-Strain Curve for Concrete in Direct Tension, Bulletin RILEM, No. 30, pp. 95–97 (1966).
25. Petersson, P.E., Crack Growth and Development of Fracture Zones in Plain Concrete and Similar Materials, Doctoral Dissertation, Lund Institute of Technology, Lund, Sweden (1981).
26. Reinhardt, H.W., and Walraven, J.C., Cracks in Concrete Subject to Shear, J. of the Structural Division ASCE, Vol. 108, No. ST1, Paper 16802, pp. 207–224 (1982).
27. ASCE State-of-the-Art Report on Finite Element Analysis of Reinforced Concrete, prepared by a Task Committee chaired by A. Nilson, Am. Soc. of Civil Engrs., New York (1982).
28. Bažant, Z.P., and Gambarova, P., Rough Cracks in Reinforced Concrete, Journal of the Structural Div., Proc. ASCE, Vol. 106, No. ST4, April 1980, pp. 819–842, Paper 15330; Discussion pp. 2579–2581, pp. 1377–1388 (1981).
29. Bažant, Z.P., and Tsubaki, T., Slip-Dilatancy Model for Cracked Reinforced Concrete, Journal of the Structural Division, ASCE, Vol. 106, No. ST9, Paper No. 15704, pp. 1947–1966 (1980).
30. Kupfer, H.B., and Gerstle, K.H., Behavior of Concrete under Biaxial Stress, Journal of the Engineering Mechanics Division, ASCE, Vol. 99, No. EM4, Proc. Paper 9917, pp. 853–866 (1973).
31. Liu, T.C.Y., Nilson, A.H., and Slate, F.O., Biaxial Stress–Strain Relations for Concrete, Journal of the Structural Division, ASCE, Vol. 98, No. ST5, Proc. Paper 8905, pp. 1025–1034 (1972).
32. Rosenthal, I., and Glucklich, J., Strength of Plain Concrete under Biaxial Stress, ACI Journal, pp. 903–914 (1970).
33. Kachanov, L.M., Time of Rupture Process Under Creep Conditions, Izv. Akad, Nauk, SSR, Otd. Tekh, Nauk, No. 8, pp. 26–31 (1958).
34. Janson, J., and Hult, J., Fracture Mechanics and Damage Mechanics, – A Combined Approach, Journal de Mécanique Appliquée, Vol. 1, No. 1, pp. 69–84 (1977).
35. Løland, K.E., Continuous Damage Model for Load-Response Estimation of Concrete, Cement and Concrete Research, Vol. 10, pp. 395–402 (1980).
36. Lorrain, M., On the Application of the Damage Theory to Fracture Mechanics of Concrete, A State-of-the-Art Report, Civil Engineering Department, I.N.S.A., 31077 Toulouse, Cedex, France.
37. Mazars, Mechanical Damage and Fracture of Concrete Structures, 5th International Conference on Fracture, Edited by D. François, Cannes, France, Vol. 4, pp. 1499–1506 (1981).
38. Arrea, M., Ingraffea, A.R., Mixed-Mode Crack Propagation in Mortar and Concrete, Report No. 81–83, Dept. of Structural Engineering, Cornell University, Ithaca, N.Y., Feb. (1982).
39. Knott, J.F., Fundamentals of Fracture Mechanics, Butterworths, London, England (1973).
40. Parker, A.P., The Mechanics of Fracture and Fatigue, E. & F.N. Spon, Ltd. – Methuen, London (1981).
41. Broek, D., Elementary Engineering Fracture Mechanics, Noordhoff International Publishing, Leyden, Netherlands (1974).

42. Mindess, S., The Application of Fracture Mechanics to Cement and Concrete: A Historical Review, Chapter I in "Fracture Mechanics of Concrete", ed. by F.H. Wittmann, Elsevier, The Netherlands (1983).
43. Brown, J.H., Measuring the Fracture Toughness of Cement Paste and Mortar, Magazine of Concrete Research, Vol. 24, No. 81, pp. 185–196 (1972).
44. Carpinteri, A., Experimental Determination of Fracture Toughness Parameters K_{IC} and J_{IC} for Aggregative Materials, Advances in Fracture Research, (Proc., 5th International Conference on Fracture, Cannes, ed. by D. François, Vol. 4, pp. 1491–1498 (1981).
45. Carpinteri, A., Static and Energetic Fracture Parameters for Rocks and Concretes, Report, Instituto di Scienza delle Costruzioni-Ingegneria, University of Bologna, Italy (1980).
46. Entov, V.M., and Yagust V.I., Experimental Investigation of Laws Governing Quasi–Static Development of Macrocracks in Concrete,: Mechanics of Solids (translation from Russian), Vol. 10, No. 4, pp. 87–95 (1975).
47. Gjørv, O.E., Sørensen, S.I., and Arnesen, A., Notch Sensitivity and Fracture Toughness of Concrete, Cement and Concrete Research, Vol. 7, pp. 333–344 (1977).
48. Huang, C.M.J., Finite Element and Experimental Studies of Stress Intensity Factor for Concrete Beams, Thesis Submitted in Partial Fulfillment of the Requirements for the Degree of Doctor of Philosophy, Kansas State University, Kansas (1981).
49. Kaplan, M.F., Crack Propagation and the Fracture of Concrete, American Concrete Institute Journal, Vol. 58, No. 11 (1961).
50. Kesler, C.E., Naus, D.J., and Lott, J.L., Fracture Mechanics – Its Applicability to Concrete, International Conference on the Mechanical Behavior of Materials, Kyoto, August (1971).
51. Mindess, S., Lawrence, F.V., and Kesler, C.E., The J-Integral As a Fracture Criterion for Fiber Reinforced Concrete, Cement and Concrete Research, Vol. 7, pp. 731–742 (1977).
52. Naus, D.J., Applicability of Linear-Elastic Fracture Mechanics to Portland Cement Concretes, Thesis Submitted in Partial Fulfillment of the Requirements for the Degree of Doctor of Philosophy, University of Illinois at Urbana-Champaign (1971).
53. Shah, S.P., and McGarry, F.J., Griffith Fracture Criterion and Concrete, Journal of the Engineering Mechanics Division, ASCE, Vol. 97, No. EM6, Proc. Paper 8597, pp. 1663–1676 (1971).
54. Sok, C., Baron, J., and François, D., Mécanique de la Rupture Appliquée au Béton Hydraulique, Cement and Concrete Research, Vol. 9, pp. 641–648 (1979).
55. Swartz, S.E., Hu, K.K., Fartash, M., and Huang, C.M.J., Stress Intensity Factors for Plain Concrete in Bending – Prenotched Versus Precracked Beams, Report, Department of Civil Engineering, Kansas State University, Kansas (1981).
56. Walsh, P.F., Fracture of Plain Concrete,: The Indian Concrete Journal, Vol. 46, No. 11, pp. 469, 470, and 476 (1979).
57. Wecharatana, M., and Shah, S.P., Resistance to Crack Growth in Portland Cement Composites, Report, Department of Material Engineering, University of Illinois at Chicago Circle, Chicago, Illinois (1980).
58. Bažant, Z.P., and Oh, B.H., Rock Fracture via Stress-Strain Relations, Concrete and Geomaterials, Report No. 82-11/665r, Northwestern University, Evanston, Illinois (1982); *also to appear in ASCE Journal of Engineering Mechanics, Vol. 110 (1984).*
59. Bažant, Z.P., and Cedolin, L., Fracture Mechanics of Reinforced Concrete, Journal of the Engineering Mechanics Division, ASCE, Vol. 106, No. EM6, Proc. Paper 15917, December 1980, pp. 1287–1306; with Discussion and Closure in Vol. 108, EM., pp. 464–471 (1982).
60. Bažant, Z.P., and Cedolin, L., *Finite Element Modeling of Crack Band Propagation,* Journal of Structural Engineering, ASCE, Vol. 109, No. ST2, pp. 69–92 (1983).

61. Flanagan, D.P., and Belytschko, T., A Uniform Strain Hexahedron and Quaderlateral with Orthogonal Hourglass Control, Int. J. for Numerical Methods in Engineering, Vol. 17, pp. 679–706 (1981).
62. Marchertas, A., Bažant, Z.P., Belytschko, T., and Fistedis, S.H., Extension of HCDA Safety Analysis of Large PCRV Containment Structures, Preprints 4th Intern. Conf. on Struct. Mech. in Reactor Technology, San Francisco, Paper E4/1 (1977).
63. Marchertas, A.H., Beltyschko, T.B., Bažant, Z.P., Transient Analysis of LMFBR Reinforced/Prestressed Concrete Containment, Trans, 5th Intern, Conf. on Struct. Mech. in Reactor Tech., Vol. H, Paper H4/1, West Berlin, ed. by T.A. Jaeger and B.A. Boley, publ. by North Holland (1979).
64. Marchertas, A.H., Fistedis, S.H., Bažant, Z.P., and Belytschko, T., Analysis and Application of Prestressed Concrete Reactor Vessels for LMFBR Containment, Nuclear Engng. and Design, Vol. 49 pp. 155–173 (1978).
65. Building Code Requirements for Reinforced Concrete (ACI Standard 318–377), Am. Concrete Institute, Detroit (1977).
66. Marchertas, A.H., Kulak, R.F., and Pan. Y.C., *Performance of Blunt Crack Approach* Within a General Purpose Code, in Nonlinear Numerical Analysis of Reinforced Concrete, ed. by L.E. Schwer, Am. Soc. of Mech. Engrs., New York 1982, (presented at ASME Winter Annual Meeting, Phoenix, pp. 107–123 (1982).
67. Bažant, Z.P., Pfeiffer, P., Finite Element Crack Band Analysis, in preparation.
68. Bažant, Z.P., Pfeiffer, P., Marchertas, A.H., *Blunt Crack Band Propagation in Finite* Element Analysis for Concrete Structures, Preprints 7th Int. Conf. on Structural Mechanics in Reactor Technology, Chicago (1983).
69. Rice, J.R., Mathematical Analysis in the Mechanics of Fracture, in Fracture, an Advance Treatise, H. Liebowitz, ed. Vol. 2, Academic Press, New York, N.Y., pp. 191–250 (1968).
70. Haugeneder, E., A Note of Finite Element Analysis of Blunt Crack Band Propagation, Proc., Intern. Conf. on Constitutive Equations for Engineering Materials, ed. by C. Desai, University of Arizona, Tucson, pp. 561–564 (1983).
71. Pan, Y.C., Marchertas, A.H., Kennedy, J.M., Finite Element of Blunt Crack Band Propagation, A Modified J-Integral Approach, Preprints, 7th Intern. Conf. on Structural Mechanics in Reactor Technology, Paper H, Chicago (1983).
72. Rice, J.R., *The Localization of Plastic Deformation,* Preprints of the 14th IUTAM Congress (Int. Union of Theor. and Appl. Mech.), held in Delft, Netherlands, Edited by W.T. Koiter, North Holland Publishing Co, Amsterdam, pp. 207–220 (1976).
73. Bažant, Z.P., Tsubaki, T., and Belytschko, T.B., Concrete Reinforcing Net: Safe Design, Journal of the Structural Division, Proc. ASCE Vol. 106, No. ST9, pp. 1899–1906, Paper 15705 (1980).
74. Bažant, Z.P., and Wahab, A.B., Instability and Spacing of Cooling or Shrinkage Cracks, Journal of the Engineering Mechanics Division, ASCE, Vol. 105, No. EM5, Proc. Paper 14933, pp. 873–889 (1979),
75. Bažant, Z.P., and Wahab, A.B., Stability of Parallel Cracks in Solids Reinforced by Bars, *International Journal of Solids and Structures, Vol. 16, pp. 97–105 (1980).*
76. Branson, D.E., Design Procedures for Computing Deflection, ACI Journal, Vol. 65, No. 9, pp. 730–742 (1968).
77. Kani, G.N.J., Basic Facts Concerning Shear Failure, Part I and Part II, J. of ACI, Vol. 63, No. 6, pp. 675–692 (1966).
78. Leonhardt, F., and Walther, R., Beiträge zur Behandlung der Schubprobleme im Stahlbetonbau, Beton-u Stahlbetonbau, Vol. 56, No. 12 (1961), Vol. 57, No. 2, 3, 6, 7, 8, (1962), Vol. 58, No. 8, 9 (1963).
79. Bhal, N.S. Über den Einfluss der Balkenhöhe auf Schubtragfähihkeit von einfeldrigen Stahlbetonbalken mit und ohne Schubbewehrung, Dissertation, Unversität Stuttgärt (1968).

80. Walraven, J.C., The Influence of Depth on the Shear Strength of Lightweight Concrete Beams without Shear Reinforcement, Stevin Laboratory Report No. 5-78-4, Delft University of Technology (1978).
81. Taylor, H.P.J., The Shear Strength of Large Beams, J. of the Structural Division ASCE, Vol. 98, pp. 2473–2490 (1972).
82. Rüsch, M., Haugli, F.R., and Mayer, M., Schubversuche an Stahlbeton Rechteckbalken mit Gleichmässig Verteilter Belastung, Deutscher Ausschuss für Stahlbeton, Heft 145, W. Ernst u. Sohn, West Berlin (1962).
83. Swamy, R.N., and Qureshi, S.A., Strength, Cracking and Deformation Similitude in Reinforced T-Beams under Bending and Shear, Part I and II, J. of Am. Concrete Inst., Vol. 68, No. 3, pp. 187–195 (1971).
84. Bažant, Z.P., Kim. J.K., Size Effect in Shear Failure of Longitudinally Reinforced Beams, Am. Concrete Institute Journal Vol. 81 (1984), in press.
85. Reinhardt, H.W., Masstabeinfluss bei Schubversuchen im Light der Bruchmechanik (Size Effect in Shear Tests in the Light of Fracture Mechanics), Beton-und Stahlbetonbau, Vol. 7, No. 1, pp. 19–21 (1981).
86. Reinhardt, H.W., Similitude of Brittle Fracture of Structural Concrete, Proc. IABSE Colloquium Advanced Mechanics of Reinforced Concrete, Delft, pp. 201–210 (1981).
87. Bažant, Z.P., Oh, B.H., Deflections of Cracked Reinforced Concrete Beams, Am. Concrete Institute Journal, Vol. 81 (1984), in press.
88. Bažant, Z.P., Oh, B.H., Spacing of Cracks in Reinforced Concrete, J. of Engng. Mech. ASCE, in press.
89. Agrawal, G.L., Tulin, L.G., and Gerstle, K.H., Response of Doubly Reinforced Concrete Beams to Cyclic Loading, ACI Journal, Proc. Vol. 63, No. 7, pp. 823–835 (1965).
90. Bruns, N.H., and Siess, C.P., Plastic Hinging in Reinforced Concrete, J. of the Structural Division ASCE, Vol. 92, No. ST5, pp. 45–64 (1966).
91. Burns, N.H., and Siess, C.P., Repeated and Reversed Loading in Reinforced Concrete, J. of the Structural Division ASCE, Vol. 92, No. ST5, pp. 65–78 (1966).
92. Sinha, B.P., Gerstle, K.H., and Tulin, L.G. Response of Singly Reinforced Beams of Cyclic Loading, ACI Journal, Proc. Vol. 61, No. 8, pp. 1021–1038 (1964).
93. Bažant, Z.P., and Panula, L., Practical Prediction of Time-Dependent Deformations of Concrete, Materials and Structures (RILEM, Paris), Vol. 11, pp. 307–328, 415–434 (1978), Vol. 12, pp. 169–183 (1979).
94. Hollington, M.R., A Series of Long-Term Tests to Investigate the Deflection of Representative Precast Concrete Floor Components, Technical Report TRA 442, Cement and Concrete Association (London) (1970).
95. Krafft, J.M., Sullivan, A.M. Boyle. R.W., Effect of Dimensions on Fast Fracture Instability of Notched Sheets, Cranfield Symposium, Vol. I, pp. 8–28 (1961).
96. Bažant, Z.P., Cedolin, L., Approximate Linear Analysis of Concrete Fracture by R-Curves, Journal of Structural Engineering ASCE, Vol. 110, No. 5T6, June (1984).
97. Tada, H., Paris, P.C., and Irwin, G.R., The Stress Analysis of Cracks Handbook, Del Research Corp., Hellertown, Pa. (1973).
98. Wnuk, M., Bažant, Z.P., and Law, E., Stable growth of Fracture in Brittle Aggregate Materials, Theoretical and Applied fracture Mechanics, Vol. 2 (1984) in press.
99. Bažant, Z.P., Ohtsubo, H., and Aoh, K., Stability and Post-Critical Growth of a System of Cooling or Shrinkage Cracks, International Journal of Fracture, Vol. 15, No. 5., pp. 443–456 (1979).
100. Chi, M., and Kirstein, A.F., Flexural Cracks in Reinforced Concrete Beams, Journal, American Concrete Institute, Proc., Vol. 54, No. 10, pp. 865–878 (1958).
101. Clark, A.P., Cracking in Reinforced Concrete Flexural Member, Journal, American Concrete Institute, Proc., Vol. 52, No. 8, pp. 851–862 (1956).

102. Kaar, P.H., and Mattock, A.H., High Strength Bars as Concrete Reinforcement, Part 4. Control of Cracking, Journal, Portland Cement Association Research and Development Laboratories, Vol. 5, No. 1, pp. 15–38 (1963).
103. Hognestad, E., High Strength Bars as Concrete Reinforcement, Part 2. Control of Flexural Cracking, Journal, Portland Cement Association Research and Development Laboratories, Vol. 4, No. 1, pp. 46–63 (1962).
104. Mathey, R.G., And Watstein, D., Effect of Tensile Properties of Reinforcement on the Flexural Characteristics of Beams, Journal, American Concrete Institute, Proc. Vol. 56, No. 12, pp. 1253–1273 (1960).
105. Bažant, Z.P., and Raftshol, W.J., Effect of Cracking in Drying and Shrinkage Specimens, Cement and Concrete Research, Vol. 12, pp. 209–226 (1982).
106. Bažant, Z.P., Mathematical Models for Creep and Shrinkage of Concrete, in Creep and Shrinkage in Concrete Structures, ed. by Z.P. Bažant and F.H. Wittmann, J. Wiley & Sons, London, pp. 163–285 (1982).
107. Bažant, Z.P., and Ohtsubo, H., Stability Conditions for Propagation of a System of Cracks in a Brittle Solid, Mechanics Research Communications, Vol. 4, No. 5, pp. 353–366 (1977).
108. Lachenbruch, A.H., Journal of Geophysical Research, Vol. 66, p. 4273 (1961).
109. Lister, C.R.B., Geophysical Journal of the Royal Astronomical Society, Vol. 39, pp. 465–509 (1974).
110. Bažant, Z.P., and Oh, B.H., Model of Weak Planes for Progressive Fracture of Concrete and Rock, Report No. 83-2/448m, Center for Concrete and Geomaterials, Northwestern University, Evanston, Il. (1983).
111. Bažant, Z.P., and Oh, B.H., Microplane Model for Fracture Analysis of Concrete Structures, Proc., Symp. on the Interaction of Nonnuclear Munitions with Structures, U.S. Air Force Academy, Colorado Springs, May 1983, ed. by C.A. Ross, publ. by McGregor & Werner, Inc., Wash. D.C.
112. Taylor, G.I., Plastic Strain in Metals, J. Inst. Metals, Vol. 63, pp. 307–324 (1983).
113. Batdorf, S.B., and Budiansky, B., A Mathematical Theory of Plasticity Based on the Concept of Slip, NACA TN1871 (1949).
114. Zienkiewics, O.C., and Pande, G.N., Time-Dependent Multi-laminate Model of Rocks – A Numerical Study of Deformation and Failure of Rock Masses, Int. Journal of Numerical and Analytical Methods in Geomechanics, Vol. 1, pp. 219–247 (1977).
115. Pande, G.N., and Sharma, K.G., Multi-Laminate Model of Clays – A Numerical Evaluation of the Influence of Rotation of the Principal Stress Axes, Report, Department of Civil Engineering, University College of Swansea, U.K., 1982; see also Proceedings, Symposium on Implementation of Computer Procedures and Stress-Strain Laws in Geotechnical Engineering, ed. by C.S. Desai and S.K. Saxena, held in Chicago, Aug. 1081, Acorn Press, Durham, N.C., pp. 575–590 (1981).
116. Pande, G.N., and Xiong, W., An Improved Multi-laminate Model of Jointed Rock Masses, Proceedings, International Symposium on Numerical Models in Geomechanics, ed. by R. Dungar, G.N. Pande, and G.A. Studer, held in Zurich, Sept. 1982, Balkema, Rotterdam, 1982, 218–226.
117. Bažant, Z.P., and Tsubaki, T., Concrete Reinforcing Net: Optimum Slip-Free Limit Design, Journal of the Structural Division, ASCE Vol. 105, No. ST2, Proc. Paper 14344, Feb. 1979, pp. 327–346; Discussion and Closure, pp. 1375–1383 (1981).
118. Albrecht, J., and Collatz, L., Zur numerischen Auswertung mehrdimensionaler Integrale, Zeitschrift für Angewandte Mathematik und Mechanik, Band 38, Heft 1/2, Jan./Feb., pp. 1–15.
119. Bažant, Z.P., and Oh, B.H., Efficient Numerical Integration on the Surface of a Sphere, Report, Center for Concrete and Geomaterials, Northwestern University, Evanston, Ill. (1982).

120. Bažant, Z.P., and Gambarova, P., Crack Shear in Concrete: Crack Band Microplane Model, Journal of Engineering Mechanics ASCE, Vol. 110 (1984), in press.
121. Paulay, T., and Loeber, P.J., Shear Transfer by Aggregate Interlock, Am. Concr. Inst. Special Publ. SP42, Detroit, pp. 1–15 (1974).
122. Reinhardt, H.W., and Walraven, J.E., Crack in Concrete Subject to Shear, Journal of the Structural Division ASCE, Vol. 108, pp. 207–224 (1982).
123. Walraven, J.C., and Reinhardt, H.W., Theory and Experiments on the Mechanical Behavior of Cracks in Plain and Reinforced Concrete Subjected to Shear Loading, HERON Journal Vol. 26, No. 1A, Dept of Civil Eng. Delft University of Technology, Delft (1981).
124. Laible, J.P., White, R.N., and Gergely, P., Experimental Investigation of Shear Transfer across Cracks in Concrete Nuclear Containment Vessels, Am. Concrete Inst., Special Publ. SP53, pp. 203–226 (1977).
125. Mattock, A.H., The Shear Transfer Behavior of Cracked Monolithic Concrete Subject to Cyclical Reversing Shear, REport SM7404, Dept. of Civil Engng., Univ. of Washington, Seattle (1974).
126. Paulay, T., Park, R., and Phillips, M.H., Horizontal Construction Joints in Cast-in-Place Reinforced Concrete, in Shear in Reinf. Concrete, Vol. 2, Am. Concrete Inst. Special Publ. SP42, Detroit (1974).
127. Laible, J.P., White, R.N., and Gergely, P., Experimental Information on Shear Transfer Across Cracks in Concrete Nuclear Containment Vessels, Special Publ. SP53, Am. Concr. Inst., pp. 203–226, Detroit 1977.

Additional bibliography

128. Baumann, T., Zur Frage der Netzbewehrung von Flächentragwerken, Der Bauingenieur, Vol. 47, No. 10, pp. 367–377 (1971).
129. Bažant, Z.P., Mathematical Models for Creep and Shrinkage of Concrete, Chapter 7 in Creep and Shrinkage in Concrete Structures, ed. by Z.P. Bažant and F.H. Wittmann, J. Wiley & Sons, London, pp. 163–256.
130. Bažant, Z.P., and Oh, B.H., Strain Rate Effect in Rapid Triaxial Loading of Concrete, Vol. 108, pp. 764–782 (1982).
131. Bažant, Z.P., and Oh, B.H., Concrete Fracture via Stress-Strain Relations, Report No. 81-10/665c, Center for Concrete and Geomaterials, Technological Institute, Northwestern University, Evanston, Ill. (1981).
132. Bažant, Z.P. and Oh, B.H., Deformation of Cracked Net-Reinforced Concrete Walls, Journal of the Structural Engineering ASCE, Vol. 109, No. ST2, pp. 93–108 (1983).
133. Bhal, N.S., Über den Einfluss der Balkenhöhe auf Schubtragfähigkeit von einfeldrigen Stahlbetonbalken mit und ohne Schubbewehrung, Dissertation, Universität Stuttgart (1968).
134. Building Code Requirements for Reinforced Concrete ACI-318-77, ACI Committee 318, American Concrete Institute, Detroit, Mich. (1977).
135. CEB-FIP Model Code for Concrete Structures, Commité Eurointernational du Béton, CEB Bulletin No. 124/125-E, Paris (1978).
136. Cedolin, L., and Bažant, Z.P., Fracture Mechanics of Crack Bands in Concrete, Fracture Mechanic Methods for Ceramics, Rocks and Concrete, ed., S.W. Freiman and E.P. Fuller, Am. Soc. for Testing Materials STP745, pp. 221–236 (1981).
137. Cedolin, L., and Dei Poli, S., Finite Element Studies of Shear Critical R/C Beams, J. of the Engng. Mech. Div., ASCE, Vol. 103, No. EM3, pp. 395–410 (1979).
138. Cervenka, V., and Gerstle, K.H., Inelastic Analysis of Reinforced Concrete Panels, Publications, Intern. Assoc. for Bridge and Structural Engng., Zurich, Switzerland, Vol. 31, 1971, pp. 31–45 and Vol. 32, pp. 25–79 (1972).

139. Christensen, R.M., A Rate-Dependent Criterion for Crack Growth, Intern. J. of Fracture, Vol. 15, No. 1, Feb. 1979, pp. 3–21,; disc. Vol. 16, pp. R229–R232, R233–R237 (1980).
140. Chudnovsky, A., On the Law of Fatigue Crack Layer Propagation in Polymers, Polymer Engineering and Science, Vol. 22, No. 15, pp. 922–927 (1982).
141. Chudnovsky, A., Proceedings of NSF Workshop on Damage, held in General Butler State Park in May 1980, University of Cincinnati.
142. Crisfield, M.A., Local Instabilities in the Non-linear Analysis of Reinforced Concrete Beams and Slabs, Proc., Institution of Civil Engrs. Part 2, Vol. 73, pp. 135–145 (1982).
143. Crisfield, M.A., Accelerated Solution Techniques and Concrete Cracking, Comp. Methods in Appl. Mech. and Engng. Vol. 30 (1982).
144. Carpinteri, A., Notch-Sensitivity and Fracture Testing of Aggregate Materials, Engng, Fracture Mechanics, Vol. 16, No. 14, pp. 467–481 (1982).
145. Ingraffea, A.R., Numerical Modeling of Fracture Propagation, in Rock Fracture Mechanics, ed. by H.P. Rossmanith, publ. by The International Center for Mechanical Sciences, Udine, Italy (1983).
146. Isida, J., Elastic Analysis of Cracks and Stress Intensity Factors, Baifukan Publishing Col, Japan (1976).
147. Kachanov, M., Continuum Model of Medium with Cracks, J. of the Engng. Mech. Div. ASCE, Vol. 106, pp. 1039–1051 (1980).
148. Kachanov, M.L., A Microcrack Model of Rock Inelasticity, Mechanics of Materials, North Holland, Vol. 1, pp. 19–41 (1982).
149. Kani, G.N.J., Basic Facts Concerning Shear Failure, Part I and Part II, J. of ACI, Vol. 63, No. 6, pp, 675–692 (1966).
150. Leonhardt, F., and Walther, R., Beitrage nur Behandlung der Schubprobleme im Stahlbeton bau, Beton-u Stahlbetonban, Vol. 56, No. 12 (1961), Vol. 57, No. 2, 3, 6, 7, 8, (1962), Vol. 58, No. 8, 9 (1963).
151. Marchertas, A.H., Belytschko, T.B., Comparison of Transient PCRV Model Test Results with Analysis, Trans. 5th Int. Conf. on SMiRT, Paper H8/2, Berlin (1979).
152. Marchertas, A.H., and Belytschko, T.B., Transient Analysis of a PCRV for LMFBR Primary Containments, Special Issue on Mechanics of Applications to Test Breeder Reactor Safety, Nuclear Technology, Vol. 51, No. 3., pp. 433–442 (1980).
153. Margolin, L.G., Numerical Simulation of Fracture, Proceedings, INtern. Conf. on Constitutive Relations for Engineering Mechanics, ed. by C. Desai, University of Arizona, Tucson, pp. 567–572 (1983).
154. Mihashi, H., and Zaitzev, J.W., Statistical Nature of Crack Propagation, Chapter 4 in Report of RILEM Techn. Comm. 50-FMC, to appear
155. Morley, C.T., Yield Criteria for Elements of Reinforced Concrete Slabs, Introductory Report, Colloquium, Plasticity in Reinforced Concrete, Report of the Working Commission, Inter. Assoc. for Bridge and Struct. Engng., Vol. 8, pp. 35–47 (1979).
156. Nilson, A., Nonlinear Analysis of Reinforced Concrete by Finite Element Method, Am. Concrete Institute Journal, Vol. 65 (1968).
157. Paris, P.C., Fracture Mechanics in the Elastic Plastic Regime, Flaw Growth and Fatigue, ASTM Special Techn. Publ. 631, Am. Soc. for Testing Materials, Philadelphia, pp. 3–27 (1977).
158. Park, R., and Paulay, T., Reinforced Concrete Structures, J. Wiley & Sons, New York, (1975).
159. Paulay, T., and Loeber, P.J., Shear Transfer by Aggregate Interlock Shear in Reinforced Concrete, Special Publications SP-42, American Concrete Institute, Detroit, Mich., pp. 1–15 (1974).
160. Pietruszczak, S., and Mroz, Z., Finite Element Analysis of Deformation of Strain-Softening Materials, Intern. J. for Numerical Methods in Engineering, Vol. 17, pp. 327–334 (1981).

161. Rice, J.R., An Examination of the Fracture Mechanics Energy Balance from the Point of View of Continuum Mechanics, Proc. First International Conference on Fracture (held in Sandia) T. Yokobori, et al., eds. Japanese Soc. for Strength and Fracture of Materials, Tokyo, Japan, Vol. 1, pp. 309–340 (1965).
162. Rice, J.R., Mathematical Analysis in the Mechanics of Fracture, in Fracture an Advance Treatise, H. Liebowitz, ed., Vol. 2, Academic Press, New York, pp. 191–250 (1968).
163. Rüsch, E.H., Haugh, F.R., and Mayer, M., Schubversuche an Stahlbeton Rechteckbalken mit Gleichmassig verteilter Belastung, Deutscher Ausschuss für Stahlbeton, Heft 145, W. Ernst & Sohn, West Berlin (1962).
164. Saouma, V.E., Ingraffea, A.R., and Catalano, D.M., Fracture Thoughness of Concrete-K_{IC} Revisited, J. of the Energy Mech. Div. ASCE, Vol. 108, pp. 1152–1166 (1982).
165. Seaman, L., Curran, D.R. Shockey, D.A., Computational Models for Ductile and Brittle Fracture, J. of Applied Physica, Vol. 47, No. 11, 1976, pp. 4814–4826 (also L. Seaman, Proceedings, NSF Workshop on Damage and Fracture, Stone Mountain, Nov. 1982, ed. by A. Alturi, Georgia Institute of Technology, Atlanta.
166. Stout, R.B., Deformation and Thermodynamic Response for a Dislocation Model of Brittle Fracture, Engineering Fracture Mechanics, to appear (also Report UCRL-87472, Lawrence Livermore Laboratory, 1982).
167. Stout, R.B., Thigpen, L., and Peterson, L., Modeling the Deformation of Materials Involving Microcracks Kinetics, Report UCRL-85477, Lawrence Livermore National Laboratory, Livermore, Cal., 1981 (to appear in Int. J. of Num. Methods in Geomechanics, 1983).
168. Stroud, A.H., Approximate Calculation of Multiple Integrals, Prentice Hall, Englewood Cliffs, New Jersey, pp. 296–302 (1971).
169. Swamy, R.N., and Qureshi, S.A., Strength, Cracking and Deformation Similitude in Reinforced T-Beams under Bending and Shear, Part I and Part II, J. of Am. Concrete Inst., Vol. 68, No. 3, pp. 187–195 (1971).
170. Taylor, H.P.J., The Shear Strength of Large Beams, J. of the Structural Division ASCE, Vol. 98, pp. 2473–2490 (1972).
171. Walraven, J.C., The Influence of Depth on the Shear Strength of Lightweight Concrete Beams without Shear Reinforcement,: Stevin Laboratory Report No. 5-78-4, Delft University of Technology (1978).
172. Watstein, D., and Mathey, R.G., Width of Cracks in Concrete at the Surface of Reinforcing Steel Evaluated by Means of Tensile Bond Specimens, Journal. American Concrete Institute, Proc. Vol. 56, No. 1, pp. 47–56.
173. Wecharatana, M., and Shah, S.P., Double Torsion Tests for Studying Slow Crack Growth of Portland Cement Mortar, Cement and Concrete Research, Vol, 10, pp. 833–844 (1980).
174. Wecharatana, M., and Shah, S.P. Slow Crack Growth in Cement Composites, J. of the Structural Division ASCE, Vol. 108, pp. 1400–1413 (1982).
175. Wittmann, F.H., Mechanics and Mechanisms of Fracture of Concrete, Advances in Fracture Research (Preprints, 5th Intern. Conf. on Fracture, in Cannes, March 1981), Vol. 4, Pergamon Press, Paris, pp. 1467–1487 (1981).
176. Zaitsev, Y.W., and Wittmann, F.H., Crack Propagation in a Two-Phase Material Such as Concrete, Fracture, 1977 (Proc. 4th Intern. Conf. on Fracture), University of Waterloo, Vol. 3, pp. 1197–1203 (1977).
177. Zech, B., and Wittmann, F.H., Variability and Mean Value of Strength of Concrete as a Function of Load, Am. Concrete Institute Journal, Vol. 77, No. 5, pp. 358–362 (1980).
178. Zech, B. and Wittmann, F.H., Influence of Rate of Loading on Strength of Concrete, Manuscript (1981).